



**THE INVESTIGATION OF
HYPERVELOCITY GOUGING**

DISSERTATION

David J. Laird, Captain, USAF

AFIT/DS/ENY/02-01

**DEPARTMENT OF THE AIR FORCE
AIR UNIVERSITY**

AIR FORCE INSTITUTE OF TECHNOLOGY

Wright-Patterson Air Force Base, Ohio

APPROVED FOR PUBLIC RELEASE; DISTRIBUTION UNLIMITED

Report Documentation Page		
Report Date 01 Mar 2002	Report Type Final	Dates Covered (from... to) Jul 2000 - Dec 2001
Title and Subtitle The Investigation of Hypervelocity Gouging	Contract Number	
	Grant Number	
	Program Element Number	
Author(s) Captain, David J. Laird, USAF	Project Number	
	Task Number	
	Work Unit Number	
Performing Organization Name(s) and Address(es) Air Force Institute of Technology Graduate School of Engineering and Management (AFIT/EN) 2950 P Street, Bldg 640 WPAFB, OH 45433-7765	Performing Organization Report Number AFIT/DS/ENY/02-01	
Sponsoring/Monitoring Agency Name(s) and Address(es) AFOSR/NM ATTN: Dr. Len Sakell 801 N. Randolph Street, Rm 732 Arlington VA 22203-1977	Sponsor/Monitor's Acronym(s)	
	Sponsor/Monitor's Report Number(s)	
Distribution/Availability Statement Approved for public release, distribution unlimited		
Supplementary Notes		
<p>Abstract</p> <p>The slipper/rail interface of a hypervelocity rocket sled is subject to immense forces due to dynamic loads and impact of the slipper with the rail, and tremendous heating due to aerodynamic and frictional effects is produced at the interface. Under these severe loading conditions, the material in the rail will sometimes experience large non-linear deformations known as gouging. Hydrocodes are computational solvers designed to handle such non-linear, large deformation, high shock, hydrodynamic applications. The ability of the hydrocode CTH to handle gouge modeling is considered, as well as the manner in which temperature environments affect deformation and plastic strain. The solution techniques and material modeling are described. Using this numerical analysis tool, a study of how gouging occurs and tracing of its development at various impact velocities was undertaken, with emphasis on the effect of shock wave distribution. Modeling the intense aerodynamic and frictional heating near the contact region, the effects of temperature on gouge initiation were evaluated through the application of several thermal environment scenarios that have been developed. The effects of friction, slipper geometry, slipper velocity, and impact method have been considered. Finally, the differences between three-dimensional and two-dimensional analysis considering gouging have been evaluated.</p>		

Subject Terms Rocket Sleds, Hypervelocity Impact, CTH, Gouging	
Report Classification unclassified	Classification of this page unclassified
Classification of Abstract unclassified	Limitation of Abstract UU
Number of Pages 197	

The views expressed in this dissertation are those of the author and do not reflect the official policy or position of the United States Air Force, Department of Defense, or the U.S. Government.

THE INVESTIGATION OF HYPERVELOCITY GOUGING

DISSERTATION

Presented to the Faculty

Graduate School of Engineering and Management

Air Force Institute of Technology

Air University

Air Education and Training Command

In Partial Fulfillment of the Requirements for the

Degree of Doctor of Philosophy

David J. Laird, BS, MS

Captain, USAF

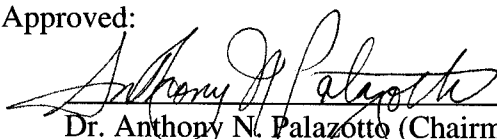
March 2002

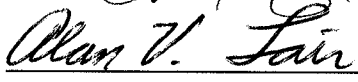
APPROVED FOR PUBLIC RELEASE; DISTRIBUTION UNLIMITED

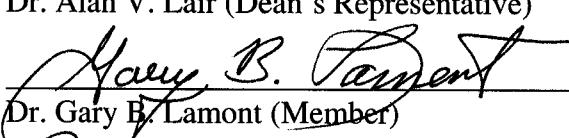
THE INVESTIGATION OF HYPERVELOCITY GOUGING

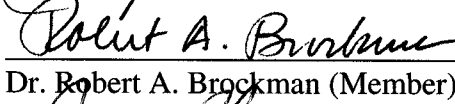
David J. Laird, BS, MS
Captain, USAF

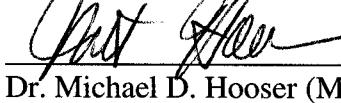
Approved:


Dr. Anthony N. Palazotto (Chairman)

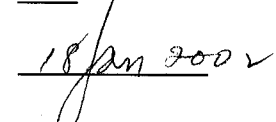

Dr. Alan V. Lair (Dean's Representative)


Dr. Gary B. Lamont (Member)

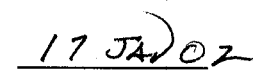

Dr. Robert A. Brockman (Member)


Dr. Michael D. Hooser (Member)

Date


18 Jan 02


12/18/01


17 Jan 02


18 Dec 01


18 Dec 01

Accepted:


Dr. Robert A. Calico

Dean, Graduate School of Engineering and Management


24 Jan 02

Date

Acknowledgements

I thank my advisor Dr. Anthony Palazotto for his guidance, counseling, and instruction during this effort. I am grateful for all of the help I have received from the other members of my doctoral committee: Dr. Gary Lamont, Dr. Robert Brockman from the University of Dayton, and Dr. Michael Hooser from the Holloman High Speed Test Track. I also acknowledge the inputs and special assistance of Craig Schmitz of MidSouth Engineering, Dr. Gerald Kerley of Kerley Technical Services, Dr. Paul Taylor at Sandia National Laboratories, Dr. Ala Tabiei from the University of Cincinnati, Dr. Ron Hinrichsen at the ASC MSRC, and Dr. David Belk at Eglin AFB. I would also like to recognize all of the support I have received from my family and friends. This research has been sponsored by the Air Force Office for Scientific Research with Dr. Len Sakell as program manager.

David J. Laird

Table of Contents

	Page
Acknowledgements.....	iv
List of Figures.....	vii
List of Tables	xi
Nomenclature.....	xii
Abstract.....	xvi
I. Introduction.....	1
Background	1
Gouging Phenomenon.....	4
Problem Statement and Objectives	7
Methodology Preview	9
II. Previous Gouging Research.....	10
Methods for Gouging Mitigation	36
Summary of Previous Research.....	37
III. Methodology	39
Using Hydrocodes to Simulate Gouging	39
Introduction to Impact Dynamics	42
Overview of CTH	43
Conservation Laws.....	45
Equation of State (EOS).....	46
Constitutive Equations	51
Failure Models	56
Solution Methods for the Governing Equations	57
Spatial Discretization	59
Consistency, Accuracy, Stability, and Efficiency.....	64
Treatment of Shocks	65
Example of Finite Volume Solution Methodology.....	66
CTH Solution Sequence.....	71
Boundary Conditions	76
Material Interfaces	77
Mechanical Loading and Aerodynamic Analysis	79
Thermal Effects.....	80

IV. Results and Discussion of Numerical Simulations	92
Simulation Plan Overview	92
Modeling Technique and Baseline Oblique Impact.....	93
Formation of Material Jets in Slipper Impacts.....	114
Temperature Effects.....	118
Slipper Temperature Profiles and Elevated Rail Temperature	127
Asperity Impacts	130
Horizontal Velocity.....	137
Vertical Velocity.....	139
Geometry.....	140
Increased Rail Yield Stress	143
Rate Dependent Slipper	144
Parallel Plate Models	146
Three Dimensional Model	148
Mixed Eulerian Cell Treatment	152
Material Interface Models.....	153
Friction.....	155
Fluid Behavior and Instability	157
Explosive Welding.....	158
V. Summary and Conclusions	160
Hypervelocity Impact.....	160
Shock Wave Propagation.....	161
Effect of High Temperatures	161
Slipper Geometry	164
Effect of Material Yield Stress	164
Preventing Gouging	165
Subjects for Future Studies	166
Appendix: Sample Input Deck.....	167
References.....	171

List of Figures

Figure	Page
1. Monorail Rocket Sled	2
2. Slipper and Rail Configuration	3
3. Gouge Schematic	5
4. Gouge in Slipper [4].....	5
5. Sled Velocity and Number of Gouges for MMI Tests [11]	15
6. Comparison of Slider Yield Strength and Density to	22
7. Barker's Model [19].....	26
8. Tachau's Model [20].....	29
9. Validation of CTH to Experimental Data [22]	31
10. Example of a p - v - T Surface [57].....	47
11. Slider and Guider Represented in Lagrangian Coordinates.....	60
12. Slider and Guider Represented in Eulerian Coordinates	61
13. ALE Method	63
14. Sample Computational Grid	67
15. CTH Eulerian Cell [54].....	72
16. Sled Test Velocity Profile [77]	82
17. Shock wave and Aerodynamic Heating of Sled [4].....	83
18. Heat Inputs to System	87
19. Time Dependent Slipper Temperature Profile at 5 Seconds.....	89
20. Steady State Rail Temperature Solution	91

21. Oblique Impact Scenario.....	94
22. Computational Grid	98
23. Slipper Penetration in Baseline Impact at 0.5 μ s	99
24. Shear Forces at 0.5 μ s.....	100
25. Hump Development at 0.5 μ s	100
26. Hump Overridden at 1.0 μ s.....	101
27. Growth of Asymmetric Interaction Region at 4.5 μ s.....	101
28. Initiation of Slipper Jet at 5.0 μ s.....	102
29. Growth of Gouge at 6.5 μ s.....	102
30. Initiation of Rail Jet at 9.0 μ s.....	104
31. Growth of Gouge at 20.0 μ s.....	104
32. Growth of Gouge at 30.0 μ s.....	105
33. Resulting Gouge at 50.0 μ s.....	105
34. Maximum Gouge Depth Versus Time.....	106
35. Divisions Between Compressed and Jetted Materials	107
36. Velocity Vectors at 4.5 μ s.....	108
37. Velocity Vectors at 9.0 μ s.....	108
38. Development of High-Pressure Core at 3.0 μ s	110
39. Growth of High-Pressure Region at 4.5 μ s.....	111
40. Growth of High-Pressure Region at 9.0 μ s.....	111
41. Stress Wave Propagation at 1.0 μ s.....	112
42. Stress Wave Propagation at 4.5 μ s.....	113

43. Temperature at 4.5 μ s	114
44. Fluid Jets In Typical Hypervelocity Impact.....	115
45. Fluid Jets From Near-Edge Impact of Two Bodies	115
46. Fluid Jets from Slipper/Rail Asperity Impact	116
47. Fluid Jets from Slipper/Rail Penetration Induced Impact.....	116
48. Formation of Fluid Jets Due to Critical Impact Angle	117
49. Maximum Gouge Depth Versus Time For Various Uniform Slipper Temperatures.....	119
50. Gouge Initiation with 2500 K Slipper at 2.0 μ s.....	120
51. Gouge Initiation with 2500 K Slipper at 2.5 μ s.....	121
52. Double Gouge Formation in 1500 K Slipper at 6.0 μ s	122
53. Double Gouges in 2500 K Slipper at 23.0 μ s	123
54. Material Mixing for 1500 K Slipper at 10 μ s	124
55. Pressure Profile at 4.5 μ s for Slider Initially at 298 K and 1000 K	125
56. Material Plots for 298 K Slider at 5.0 μ s and 1000 K Slider at 4.5 μ s	125
57. Temperature Profile at 4.5 μ s for Slider Initially at 298 K and 1000 K	126
58. Yield Stress at 4.5 μ s for Slider Initially at 298 K and 1000 K	127
59. Maximum Gouge Depth Vs. Time for 500 K Source Temperature	129
60. Maximum Gouge Depth Vs. Time for Different Thermal Environments with a 2500 K Source Strength	130
61. Asperity Impact Model	131
62. Correlation of CTH Results to Experimental Data [22]	132
63. Material Deformation from 0.1 cm Asperity Impact at 1.0 μ s	133

64. Material Deformation from 0.1 Asperity Impact at 5.0 μ s	134
65. Resulting Gouge After Asperity Impact and Oblique Impact	135
66. Gouge Initiation Due to 0.5 cm Diameter Asperity	136
67. Maximum Gouge Depth Vs. Time for Asperity Impacts	137
68. Rail Damage at 24 μ s Due to 1 km/s Oblique Impact	138
69. Maximum Gouge Depth Vs. Time for Various Horizontal Velocities.....	139
70. Maximum Gouge Depth Vs. Time For Various Vertical Impact Velocities	140
71. Small Geometry Oblique Impact Model.....	141
72. Maximum Gouge Depth Vs. Time for Small Geometry Slipper	141
73. Maximum Gouge Depth Vs. Time for High Yield Stress Slipper	144
74. Maximum Gouge Depth Vs. Time for Rate Dependent Slipper Model	146
75. Parallel Plate Model with Pre-Described Deformation	147
76. Resultant Gouge Due to Pre-Described Deformation.....	147
77. Slipper Corner Contact	149
78. Three-Dimensional Oblique Impact Model	150
79. Development of Three-Dimensional Gouge at 11 μ s	151
80. Maximum Gouge Depth Vs. Time for Three Different Mixed Cell Treatments..	153
81. Maximum Gouge Depth Versus Time for Material Interface Models	155
82. Maximum Gouge Depth Vs. Time for Various Frictional Coefficients	156
83. Fluid-Like Mixing of Rail and Slipper	158
84. Kelvin-Helmholtz Instability in Fluid Flow [85].....	158
85. Interface of Two Explosively Welded Metals [42].....	159

List of Tables

Table	Page
1. Parameters for the Steinberg-Guinan-Lund Constitutive Model [47,48]	55
2. Specific heat of VascoMax 300 Steel [81]	85
3. Gouging Characteristics of Various Leading Edge Geometries	142

Nomenclature

(\cdot) Time rate of change

$(\cdot)_0$ Initial conditions

$(\cdot)_\infty$ Free stream conditions

$(\cdot)_H$ Hugoniot conditions

$(\cdot)_R$ Reference conditions

a, b, c, d Cell corner points in finite volume example

A Cell area

A, B, C, n, m Johnson-Cook model constants

B Body force per mass

c Sound speed

c_v Specific heat

C_f Coefficient of sliding friction

C_1 Exponential prefactor constant

C_2 Coefficient of drag

d Distance

E Energy, specific internal energy

E_C Energy on zero-Kelvin isotherm

F Force, $\frac{\partial u}{\partial x}$

G Shear modulus, $\frac{\partial u}{\partial y}$

i, j, k Spatial indices

i, j, m, n Cell boundary midpoints in finite volume example

K_1	Second kind of modified Bessel's function of order one
l	Source length
m	Mass
M	Mach number, mass
M_∞	Free stream Mach number
n	Unit normal vector, time step index
N	Normal force
p, P	Pressure
Q	Artificial viscosity
R	Universal gas constant
S	Internal energy per volume per time
t	Time
T	Temperature
T^*	Homologous temperature
u_P	Particle velocity
u	Temperature
U	Flow velocity
U_K	Activation energy
U_S	Shockwave velocity
v	Velocity, specific volume
V	Cell volume
w	Work
x, y	Spatial coordinates

Y	Yield stress
Y_A	Yield stress at Hugoniot elastic limit
$Y_A f(\varepsilon^p)$	Athermal yield stress component
Y_{max}	Maximum yield stress for rate independent SGL model
\dot{Y}_{max}	Maximum yield stress of athermal yield component
Y_P	Peierls stress
Y_T	Thermally activated yield stress component
Δt	Time step size
$\Delta x, \Delta y$	Cell size
α	Thermal diffusivity
β	Work hardening parameter
β_t	Position of Lagrangian body (cell)
γ	Ratio of specific heats
Γ	Grüneisen function
Γ_0	Grüneisen parameter
δt_n	Time step size
Δ	Difference operator
ε	Strain
ε_i	Initial plastic strain
ε^p	Equivalent plastic strain
$\dot{\varepsilon}^*$	Dimensionless plastic strain rate
ζ	Non-dimensionalized time

κ	Thermal conductivity
λ	Ratio of time scales
μ	Average operator, $1 - \frac{\rho_0}{\rho} = \frac{u_p}{U_s}$
ξ, η	Non-dimensionalized coordinates
ρ	Density
σ	Stress
σ_{eff}	Effective stress
σ_m	Spherical stress
$\sigma_x, \sigma_y, \sigma_z$	Direct stresses
$\sigma_1, \sigma_2, \sigma_3$	Principal stresses
Σ	Stress tensor
1,2,3,4	Control points in finite volume example
∇	Gradient operator
$\partial\beta_t$	Boundary of cell

Abstract

The slipper/rail interface of a hypervelocity rocket sled is subject to immense forces due to dynamic loads and impact of the slipper with the rail. In addition, tremendous heating due to aerodynamic and frictional effects is produced at the interface. Under these severe loading conditions, the material in the rail will sometimes experience large non-linear deformations known as gouging.

To successfully model the gouging phenomenon, the high strain, high strain-rate, high temperature conditions and shock wave behavior present in high velocity impact dynamics must be effectively dealt with. Constitutive laws modeling inelastic material response and an appropriate equation of state also need to be considered to model these effects.

Hydrocodes are computational solvers designed specifically to handle such non-linear, large deformation, high shock, hydrodynamic applications. Part of this dissertation evaluates the ability of the hydrocode CTH to handle the problem of determining the onset of gouging. This evaluation is based on considering the hydrocode theory and its implications on the development of the gouging phenomenon. Also considered is the manner in which temperature environments affect deformation and plastic strain. The solution techniques and material modeling are described.

Using this numerical analysis tool, a study of how gouging occurs and tracing of its development at various velocities of impact was undertaken. Due to intense aerodynamic and frictional heating near the contact region, the effects of temperature on gouge

initiation were evaluated through the application of several thermal environment scenarios that have been developed. The effects of friction, slipper geometry, slipper velocity, and impact method have been considered. Finally, the differences between three-dimensional and two-dimensional analysis considering gouging have been evaluated.

THE INVESTIGATION OF HYPERVELOCITY GOUGING

I. Introduction

Background

The Holloman High Speed Test Track (HHSTT) facility at Holloman Air Force Base, New Mexico, is a ground based test facility designed to test items under simulated free flight conditions. The facility can be used for a wide variety of high speed testing applications such as materials, aircraft parts, and weapons systems. Testing is conducted using rocket propelled sled vehicles guided by steel slippers that ride on continuous steel rails. The rails are standard 171 lb/yd crane rails, butt-welded in 39-foot sections for a length of ten miles [1].

For velocities over 5,000 feet per second, test articles with a relatively small cross sectional area are usually mounted to a monorail or narrow gauge sled to minimize drag. A photo of a final stage monorail sled is shown in Figure 1. A booster stage is also partially visible.

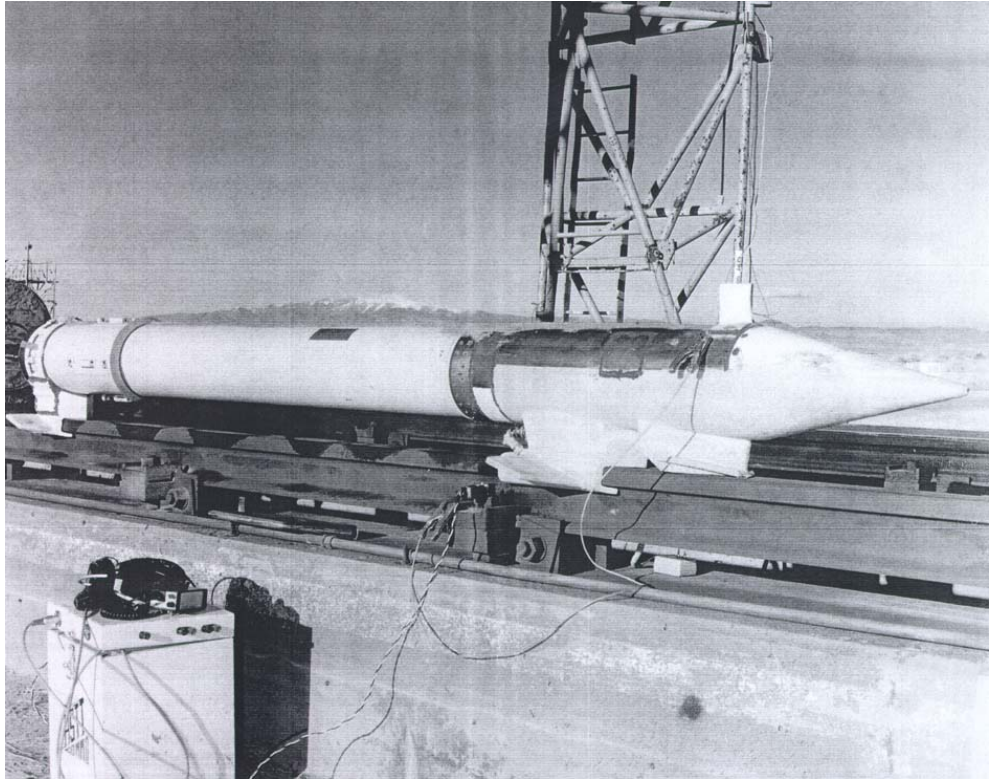


Figure 1. Monorail Rocket Sled

The sled assembly is mounted to the rail (also called the guider) by a type of shoe called a slipper or a slider, also seen in Figure 1. Slippers are normally constructed of a high strength steel alloy such as VascoMax 300. Slippers are used in the front and back of each stage. Thus, the number of slippers is dependent on the arrangement of booster rockets and the number of rails used (dual or monorail). The slipper wraps around the rail as shown in the schematic in Figure 2, allowing the sled to traverse the rail, but prohibits lateral and vertical movement in excess of a small gap between the slipper and rail. An initial gap size near 0.125" is present to allow the slipper to ride over imperfections or discontinuities in the rail, but the gap can increase as the slipper wears down. Typical dimensions for a slipper may be 8" long and 1" thick, but vary per

application. The slipper configuration pictured is just one of several slipper configurations that are in use. Other configurations include one sided (for dual rail only) or topless designs.

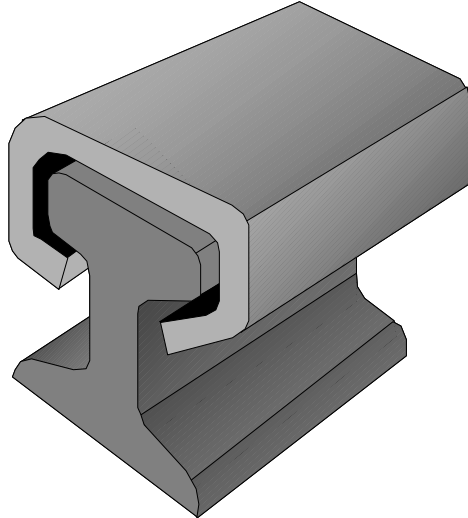


Figure 2. Slipper and Rail Configuration

In order to reduce drag and achieve higher velocities or accelerations, the sled is sometimes run in a helium environment. This is done by erecting a tent around selected portions of the track and filling it with helium. The sled may enter and/or exit the helium environment at any desired part of the test run. The helium environment drastically reduces the aerodynamic loading and heating at the slipper, as well as aerodynamically induced external loads.

Gouging Phenomenon

Currently, users of the facility have requirements to conduct tests at up to 10,000 feet per second. In order to achieve such velocities, investigation and engineering must be performed to overcome a variety of challenges. These include the proper sled layout, aerodynamic drag, sled loading, external aerodynamic lift, internal aerodynamic loading, dynamic loads, roll stability, aerodynamic heating, proper use of heat protective coatings, slipper wear, component oxidation, and gouging [2,3]. Gouging is a particular kind of surface damage to both the rail and the slider caused by the passage of the slider, and many of the other problems listed play either a direct or indirect role in the gouging process.

Extreme straightness of the rail is required to reduce the dynamic loading induced into the sled vehicle traveling along the track, particularly at high speeds approaching 10,000 fps. Straightness of the rails is maintained through precision survey and rail alignment. In spite of this, small irregularities of the rail do exist. These irregularities, along with aerodynamic forces, cause a dynamic bounce of the sled traveling down the rail at high speeds. At hypervelocity speeds, the impact of the sled on the rail can cause a tear-drop shape of material to be eroded away from the surface of the rail, sometimes resulting in a mirrored effect, occurring concurrently (lasting micro seconds) on the inside of the slipper [1].

Gouging is recognized by a tear drop shaped depression carved into the surface, with the blunt, leading edge of the feature being raised above the original surface, as shown in Figure 3. Figure 4 shows a slipper assembly after a test run, and indicates typical heat and friction related damage. A gouge can be seen on the inside of the slipper.

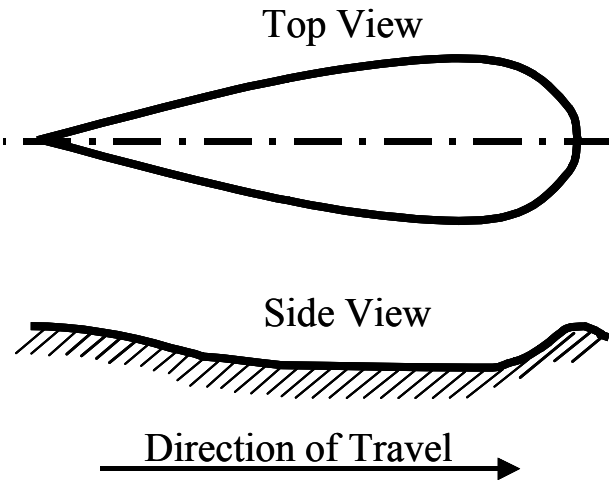


Figure 3. Gouge Schematic



Figure 4. Gouge in Slipper [4]

Gouging is observed when rocket sleds exceed 1.5 km/s (3355 mph), and is caused by the intermittent contact between the slider and rail under a combination of high relative velocity, extremely high local bearing pressure, and high temperature. The path of the

sled assembly is characterized by free flight, with this intermittent contact occurring as the slipper moves within the space afforded by the slipper/rail gap.

Gouging has been observed in metals undergoing hypervelocity sliding contact. It is initiated by an impact event, complicated by uneven wear and stress concentrations. This impact results in shock wave propagation and interaction, high pressure, plasticity, and material interaction and mixing. At sufficiently high velocity, inertial forces are so great that the materials exhibit fluid-like behavior. Shock induced pressure from the impact creates a region of plasticity under the location of impact. The tangential motion of one body with respect to the other deforms or shears material at these points resulting in the deformation of the parallel surfaces that impinge on each other in a continuous interaction. Once this interaction region grows large enough to shear the surface of one of the materials from the bulk material, a gouge is formed. Continuous interaction of the materials in the region of the gouge creates an instability that causes the gouge to grow further until the materials are no longer in contact.

Slipper wear and gouging are affected by a combination of conditions, including: velocity, slipper and rail material properties, normal loading and slipper bearing pressure, temperature, friction, and geometry. Many of these effects also change as a function of velocity.

Some of the material displaced by gouging results in ejecta that is expelled into the air behind the slider. Also, some of the slider material has been found in rail gouges, and rail material has been found in slider gouges, supporting the theory that rail and slipper gouges are somehow coupled.

It is important to keep in mind that not all contact between the slider and rail results in gouging. This leads one to recognize that investigation into the specific mechanical and thermal conditions required to initiate gouging may yield the necessary and sufficient conditions to mitigate gouging. As the mechanism for these factors in the rocket sled test are better understood and predicted, one can successfully use them in simulating the gouging mechanism.

Problem Statement and Objectives

Research toward developing a 10,000 fps ground vehicle is progressing in several areas, i.e. propulsion, thermal protection, vibration isolation, and dynamic simulation. Gouge mitigation continues to be problematic, as limited data is available to support the development of accurate models.

Gouging forces extensive maintenance to be performed on the rail, including grinding of burrs and filling of the craters along the ten-mile test section. Hypervelocity impact of subsequent test vehicles with surface anomalies on any damaged rail would cause additional damage to the sled and rail. Rail and slipper failure due to gouging and molten ejecta produced by the gouging process can cause catastrophic failure of the sled. Mitigation of gouging is absolutely critical to the successful execution of a ground vehicle design [5].

Ultimately, test track engineers would like to totally eliminate gouging from high-speed tests. Gouging may be mitigated through the use of various materials in the rail or sled sliders, or coatings on them. But any effort to mitigate gouging must be accompanied by an understanding of the gouging process and what affects it.

For the first time a study has evolved that analytically characterizes the impact of a slider with a guider at 10,000 fps considering the scientific features present in the response, i.e. temperature, shock wave action, and material response. This has required characterization of impact scenarios, aerodynamic and frictional heating, and material properties. In this study, the physics involved in gouge formation have been carefully studied. Particular attention has been given to shock wave propagation and its influence on gouge development. A shortcoming of previous gouging research is that the effect of material temperature was not considered. In this study, the effects of elevated temperature states due to aerodynamic or frictional heating have been evaluated. This study also investigates the effects of friction, slipper geometry, and velocity. The scientific issues being considered as related to the gouging phenomenon are:

- How does gouging occur?
- What is the effect of shock wave distribution?
- How does the thermal environment affect the onset of gouging?
- What is the difference between 3D and 2D analysis considering gouging making use of hydrodynamic relationships?

In summary, the goals of this dissertation are to understand the problems of gouging, understand the physics related to the gouging problem, conduct a literature search of gouging research already performed, identify and explain hydrocode methodologies, and indicate the effect of temperature on gouge initiation and development.

Methodology Preview

Much of the previous work that has been done involving gouging is outlined in Chapter II. This gives a thorough background on the factors that are known to influence gouging, and includes both experimental and numerical results.

In order to efficiently test new and/or improved system designs, new gouging models or analytical tools must be developed. Because of the extreme aerodynamic forces and the effects of these forces, any tool developed to model the rocket sled and the gouging phenomena must have the capability to handle aerodynamics, aeroelasticity, thermodynamics, frictional response, nonlinear mechanics, viscoplasticity, and material failure phenomena. Hydroram codes (or hydrocodes) are numerical programs specifically designed for problems involving high energy, explosives, material incompressibility, shock propagation, nonlinear response, and large deformations. Hydrocodes have been used successfully to model high velocity impacts, a phenomena thought to be similar to high speed gouging. Chapter III describes the methods that are used to investigate gouging in the current research, including the solution methodology incorporated in the hydrocode CTH, and an evaluation of its capability to accurately model the physics involved in gouging. The effects of several numerical issues and solution techniques within CTH are also explored.

The numerical models used, an outline of the simulations conducted, and the results of these simulations are described in Chapter IV. Finally, the summary and conclusions of the research are given in Chapter V.

II. Previous Gouging Research

Although there is currently a need to examine gouging, it is not a new phenomenon.

In fact, it has been observed in rocket sled testing for more than thirty-five years [6].

Research regarding gouging can generally be categorized into six main topic areas:

- Test track observations and gouge tests
- Laboratory gouging tests
- Numerical modeling of gouging
- Rail gun gouging
- Load analysis

This chapter examines the history research in each of these topic areas and the relevant facts found by previous researchers.

Test track observations and gouge tests. Using a monorail test sled at Sandia National Laboratory, Gerstle [7,8] conducted experiments where he specifically tried to initiate gouging in the rail. He found that gouges frequently occurred downstream from upward kinks in the rail but that very short radius irregularities, such as weld beads across the rail intended to initiate gouging, in fact did not cause gouging. Microanalysis of damaged portions of the rail (AISI 1080 steel) revealed that gouges had a surface layer of martensite with a layer of 304 stainless steel (sled shoe material) deposited on top of the martensite. Examination below the surface of gouges showed that high enough temperatures had been reached to austenitize the steel, and that the rail material was severely strained and microcracked. This was all believed to be evidence of catastrophic thermoplastic shear (adiabatic slip). Cracks into the surface of gouges characteristically

had stainless steel in their center surrounded by layers of martensite and then deformed pearlite. Rail surfaces that had not been contacted by sled shoes had no damage other than surface layer decarburization, a loss of carbon due to high temperatures, typically over 800 K.

In 1982, Krupovage and Rassmussen [9] documented the development of sled designs. They discussed that although not conclusively proven at the time, impacts between the slipper and rail are likely to be one of the causes for rail gouging. Track tests have demonstrated that controlling aerodynamic downloading can significantly reduce the oscillations leading to impact.

To give some indication of the thermal environment in the area of the slipper contact surface, the authors describe *slipper fire* (wear products leaving the aft slipper gap) as a homogenous stream of luminous material resembling the spark pattern of a grinding stone, with light emission from white to yellow. Further, intense light densities surrounding the 5000 to 7000 fps sleds are attributed to aerodynamic heating and to erosive oxidation of sled and slipper material. Considering frictional heating, the authors suggest the following relationship for the work developed by friction per unit time:

$$\dot{w} = C_f N v \quad (1)$$

where C_f is an empirical friction coefficient, N is the normal force, and v is the sled velocity. If these values can be determined, the heat generated due to friction may be calculated if one assumes that this change of energy is entirely converted to heat.

Previously, some thought was given to the idea that a thin melted layer at the contact surface may act as a lubricant. However, the authors question the idea of melt lubrication

because observations suggest that the formation of liquid metal may act as an abrasive rather than a lubricant.

In 1984, Krupovage [10] again addressed rail gouging. The author describes gouging experienced in a number of rocket sled runs with different sled types and test conditions. He observed that the largest gouge measured 4" long, 3" wide, and 0.40" deep. Gouges were found at rail breaks, and gouges were also created on the inside of slippers. In addition to those containing slipper material, some gouges were found to contain copper from an aerodynamic wedge in front of the slipper.

In addition to gouging, Krupovage points out that another rocket sled phenomenon observed to begin at velocities exceeding 5000 fps was the loss of sled material in the forward area of the sleds due to aerodynamic heating. Based on this occurrence and the results of the observed tests, he generally concludes that gouging is a result of the aerodynamic heating and oxidation of forward portions of the rocket sled and the internal slipper materials, slipper wear products, debris caused by impact of the aerodynamic wedge, or other debris from external sources. Gouging occurs when this debris becomes trapped in the sled slider and rail interface and does not result solely from the load imparted to the rail through the slider. Gouging also results from rail breaks and possibly rail surface irregularities.

It was also concluded that greater aerodynamic heating and more gouges occurred during the sled coast phase, and external material loss due to aerodynamic heating was nonexistent in the helium environment. Furthermore, a dynamic model composed of a sled bouncing through the slipper gap and impacting on the slipper support structure with some effective mass is suggested.

Mixon [11] set out to give a thorough review of previous research and experimental gouging data for many runs, including where gouges occurred and what conditions were based on a gouging database compiled by Bob L. Kirkpatrick and Will D. Wilson. Based upon other works, it is summarized that factors that appear to affect gouging include high stresses from dynamic loading, high velocity, asperities on the rail surface, frictional heating, deterioration of slippers and subsequent entrapment of deteriorated material, and external ejected sled material when in an air environment.

Sled tests considered for analysis included tests for the Low Mass Interceptor (LMI), Medium Mass Interceptor (MMI), and Patriot PAC3. Each of these test series used an independent forebody sled that carried the payload pushed by the final stage. Hence at the highest velocities, gouges could be initiated by either the forebodies front or rear slippers, or the final stage pusher rocket (Roadrunner) front or rear slippers. The forebody slippers were all web bearing slippers (monorail) for additional roll stability.

The two LMI tests investigated included the use of a helium environment. Gouging started to occur at about 5800 fps, and the tests reached a peak velocity of 6863 fps. Seventy-five to eighty-three percent of major gouges occurred after peak velocity. All of the gouges found occurred within the helium environment, where aerodynamic heating is low with minimal external burning and oxidation but friction is probably high and slipper surfaces are probably deteriorated. It is hypothesized that gouging probably contributed to excessive sled roll, which resulted in system failure during both tests.

The MMI testing consisted of seven runs with a peak velocity of 6660 fps. In four of these tests, the documentation included the location of the gouge on the railhead. Gouging started at 5400 fps, and in total 408 gouges were found, including 24 major ones

that required welding. A comparison of the velocity profile and the number and location of gouges is shown in Figure 5. In this figure, the line represents the sled velocity vs. track station, and the bars indicate the number of gouges present per 500 feet of track. This clearly shows the velocity regime in which gouging occurs for this test to be above 5400 ft/s, and that the highest concentration of gouges occurred in the region of peak velocity. Most gouges were found at the corners of the railhead, and relatively few occurred on the flat surfaces. Diagrams of the rail and location of the gouges are given in the report. There were instances of simultaneous gouging, where multiple gouges were found at the same track station. One run in particular accounted for 114 (27.9%) gouges, and 9 (37.5%) major gouges, and a large 6-inch gouge that broke the rail and led to catastrophic failure. The number of gouges per 100 ft was found to be significantly higher after peak velocity than before, which is attributed to slipper deterioration. However with respect to just the major gouges, ten occurred before the peak velocity and eight formed after. During the course of the MMI testing, the rail was repainted and this seemed to improve gouge resistance. Again, all of the gouges found were in the helium environment.

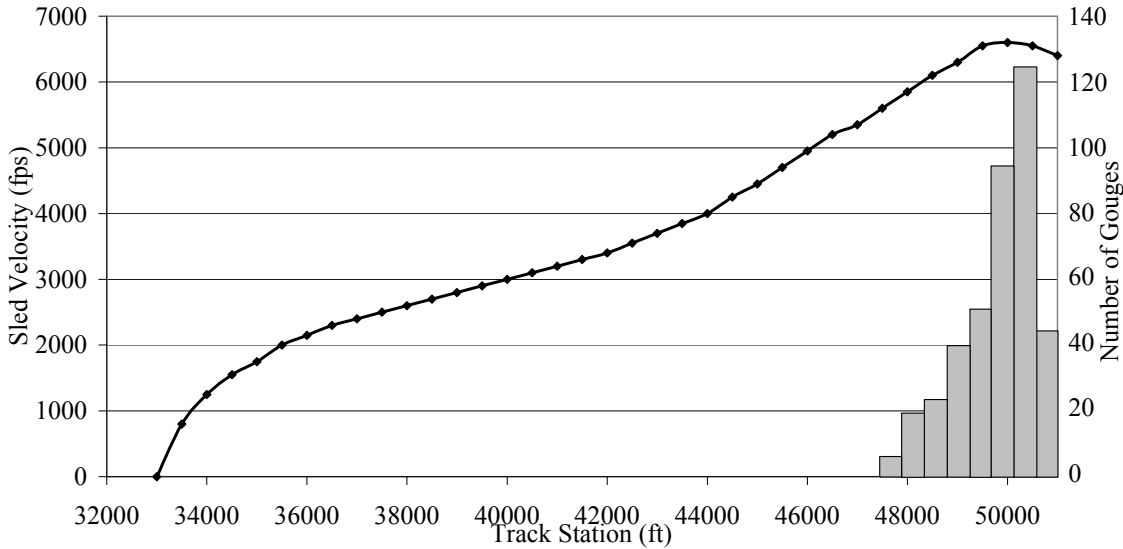


Figure 5. Sled Velocity and Number of Gouges for MMI Tests [11]

The PAC3 tests consisted of 14 runs reaching a peak velocity of 6000-6100 fps. It included a rigorous repainting program. The entire rail was sandblasted and repainted with a controlled thickness of paint (6 mils, \pm 1 mil) every 4 runs, with spot repainting where needed between every run. Gouging started at 5750 fps. In this case, it was found whether the sled was before or after peak velocity did not affect the tendency to gouge. Again, all gouges occurred in helium. Only 2 major gouges occurred in these tests, both of which were on the same run. This run had more gouging than any other PAC3 run, ending in a major structural failure of the final stage pusher.

Mixon concludes that there is a relationship between gouging and the tendency for roll forces. Sleds are described as having a tendency to roll or lift based on the gouge location, and it is probable that gouging leads to excessive roll, which often leads to failure. And conversely, roll and lift significantly influence gouge position on the

railhead. In high wear/gouge conditions, a tendency exists for gouging to occur at a higher rate after burnout, likely due to the successive deterioration of the slipper surfaces. High gouging rates occur in small velocity increments (less than 50 fps) just before and immediately following peak velocity. Structural failures also result in a considerable number of gouges. High stress, high velocity, rail imperfections, deteriorated slipper surfaces, and frictional heating are prime contributors to the onset of gouging.

Since well-maintained rail coatings significantly reduce the number of gouges, gouging may be mitigated by the establishment of the best coating and thickness, and improved coating application methods. In addition, improved track alignment and machining methods, and new slipper materials and design concepts are likely to be valuable.

Regarding the modeling of gouging, Mixon suggests an accurate model could prove beneficial in studying rail coatings if the properties that distinguish the materials from one another can be identified and measured. Thus simulations can be used to find an optimal coating material and thickness.

In 1982, Barber and Bauer [12] contrasted sliding contact behavior at low and high velocity with that of hypervelocity, which they described as the regime of velocity in which the predominant forces of interaction are inertial. They identified the existence of a hypervelocity “sliding threshold velocity” and also developed a model for the process of hypervelocity asperity impact and gouge formation. They described the gouging event as follows:

When two solids are brought together, actual physical contact occurs only at a small number of discrete contact points. The normal load between the two solids is supported by these discrete areas. The number and size of the contact points

increases with increasing applied load. Adhesion between two bodies in contact occurs at the contact spot and “cold welds” are formed. Tangential motion of one body with respect to the other deforms or shears material in the contact spots and results in further asperity contact. Frictional forces develop because of the ability of the contact spots to resist this deformation (wear results from material fracture due to excessive straining in the contact spot region.) During contact spot shearing, energy is dissipated into the deformation zone and then removed from the deformation zone by thermal conduction into the material substrate.

As sliding velocity increases, the rate of energy dissipation in the deformation zone exceeds the conduction rate out of the deformation zone, causing the deformation zone temperature to rise. As sliding velocity increases still further, the temperature of the entire surface of a slider may reach the melting point, at which point a liquid interface is formed between the sliding surfaces, greatly reducing the frictional forces observed and the coefficient of friction. The liquid interface behaves as a hydrodynamic bearing. Viscoshearing of the liquid film dissipates energy, which causes intense heating of the slider surface and results in surface melting. Surface recession occurs, providing an influx of melted material from the slider surface equal to the efflux from the interface due to slider motion, and a steady-state hydrodynamic interface is established. The development of this hydrodynamic fluid layer depends upon the material properties of the slider and guider, the sliding velocity, the normal load, and possibly the geometry of the slider.

At hypervelocity, if a fluid interface forms, velocity gradients in the interface will increase, as will the frictional force, energy deposition, surface recession, slider wear, and interface temperature. At some velocity, it is likely that the temperature of the interface region becomes so high that the interface material is vaporized, with a resultant drop in viscosity and frictional force. If a fluid interface does not form, asperity contact continues to occur at very high velocities. The asperities, however, can no longer come into contact in a steady or quasi-steady mechanical mode. Instead, the impact generally in an oblique manner, generating shock stresses. [12]

Barber and Bauer termed the point at which the impact-induced stress is equal to the ultimate strength of the material the “hypervelocity sliding threshold velocity.” They felt that the hypervelocity sliding threshold velocity, as was impact stress, was related to the asperity impact velocity, the angle of impact, and the density and shock speed of the materials involved. They also felt that hypervelocity asperity impact would be a discrete, localized, violent event resembling a microscopic explosion that would be expected to produce a small crater in the surface of the material. The center of mass of this explosion

would travel at approximately one-half of the slider velocity. Due to the relative motion of the slider, a tear-shaped crater would result rather than a simple, hemispherical shape. Barber and Bauer found little quantitative data to support their theory. However, they felt that the conclusion drawn by Graff and Dettloff, generally that a minima of both sliding velocity and normal load were required to initiate gouging, confirmed the existence of a sliding threshold velocity. Additionally, they felt that instances of rail gun gouging further confirmed the existence of a threshold sliding velocity. It was felt that the onset of gouging corresponded to the point at which asperity impact would produce stresses exceeding the ultimate strength of copper.

Laboratory Gouging Tests. Experimental investigations began in the late 1960's when Trott [13] attempted to evaluate materials for use in sliders. His method involved using a gun to fire the materials at a curved rail, although this was not successful.

In 1968, an effort to use Trott's gun method to duplicate gouging damage in a laboratory on a smaller scale and to evaluate several rocket sled shoe materials and rail coatings was undertaken by Graff et al. [14,15]. They designed experiments to create the conditions of high velocity sliding contact using a special gun facility that enabled them to shoot projectiles on a grazing angle of impact at a flat or curved target at up to 9000 fps.

Graff et al. felt that the basic nature of gouging was one of high velocity sliding contact or grazing impact between metallic surfaces. Beginning with a review of sled tests, the researchers catalogued data from gouge damage at the Holloman AFB rocket sled test track and noticed that gouging seems dependent on many parameters including rail and slipper materials, slipper geometry, rail straightness, airflow in the slipper gap,

velocity, and contact stresses. They studied previous sled runs showing that gouging began between 5200 and 5500 fps. Gouges are described by a tear drop shape with a typical gouge being 2 to 4 inches long, 1 inch wide, and 1/16 inch deep. The authors discuss coloring and metal deposits in the gouge. The maximum observed gouge frequency occurred after peak velocity, and this is attributed to increased gap size and wear effects. The review showed that the sled velocity was the primary factor affecting the frequency of gouge occurrence. They also learned that about 80% of the gouges were on the side or top edges of the rail, 15% were on the undersides, and only 5% were on the top surface of the rail. It is noted that downward biasing by canards and high strength maraging steel slippers appeared to produce less gouging.

In the laboratory, the study focused on impact velocity, slipper and rail materials, and interfacial stresses. Using projectiles of brass, copper, steel, and aluminum, Graff et al. successfully created gouges on steel target surfaces that had all the essential features of rocket sled gouges. While initial attempts by firing at a 20-foot radius curved steel target did not produce gouging, reducing to a 3 ft radius to increase stress resulted in gouges similar to those seen at Holloman AFB.

After impact, projectiles left marks on the target plate indicating the width or wear of the projectile. A layered structure of target base materials, oxide coating, molten projectile material, and projectile base material was created, suggesting the existence of a molten interface during gouging. It is suggested that aerodynamic flow conditions in the gap are probably capable of creating melting of the slipper without metal-to-metal contact. Evidence indicates that the coating material acts in the sense of a lubricant under hydrodynamic loading and transmits the supporting normal stresses but does not transmit

the gouge initiating shear stress. Melt lubrication eases high-speed friction by forming a liquid layer between the sliding surfaces. Calculations were made to support the conclusion that due to the velocity and size of projectiles, transient stresses are small in comparison with the steady pressure and may be effectively ignored. Sample calculations of the normal stresses encountered in the experiments were 78,000 psi for a steel projectile weighing 0.27 oz.

It was found that sudden jumps in stress caused by discontinuities in the curved target resulted in gouge initiation. Gouges were more likely to occur at slight kinks in the curved projectile track, where normal forces were maximum, and that gouges were predictably initiated at transverse scratches and gains of sand deliberately placed on the track surface. Furthermore, orienting the ground surface-finish of the target plate transverse to projectile motion resulted in more gouging than when the surface-finish was parallel to the motion, and sanded finishing produced fewer gouges than other finishes. It was concluded that for the same velocity and stress, the fewer surface imperfections, the fewer gouges.

Based on their observations, the authors describe the mechanism for gouge initiation as the point when, at critical conditions of normal stress and velocity, the oxide film on the target and the molten film at the projectile/target interface is penetrated and direct metal to metal contact occurs, resulting in a welded junction. This penetration of the surface layer can occur from a sudden stress jump resulting from a high spot, or from a local surface imperfection. Projectile material deforms and slightly penetrates into the target, while simultaneously, target material penetrates into the projectile. Initially, the amount of deformation is small, but continuing interaction at the metal-to-metal interface

causes pressure and shearing action that causes the size of the interaction to increase.

The growth and propagation of the gouge requires the continued shear of material at the base of the junction. Gouge termination is determined to be caused by the passage of the projectile trailing edge beyond the effective region.

Further studies by Graff and Dettloff [16] examined various projectile materials and target coatings subjected to normal stresses up to 200,000 psi. It was found that all metallic projectiles caused gouging while Teflon did not, soft metals gouged more, while harder metals had higher threshold gouging velocities. Harder maraging steels gouged less, but excessively hard steels resulted in a machining action. It is suggested that a slipper with hardness just slightly greater than the hardness of the rail would give the best results. General results for coating materials was that the successful coatings were low density, low strength, and non-metallic. Use of low strength coatings caused all of the material shear behavior to occur in the coating and not on the projectile. Plastics and ceramics were found to have insufficient strength to withstand imposed stresses, except cemented tungsten carbide that was tough enough to withstand contact shock without fracturing, welding, or gouging. Tests suggested that high normal stresses were not sufficient to cause gouging if direct metal-to-metal contact is prevented.

Also using a special purpose gun assembly, Tarcza [17] conducted gouging studies at a relatively low velocity. The primary purpose of Tarcza's work is to demonstrate that gouging is possible at velocities lower than those at which it has been previously reported, and to show that there exists a correlation between gouging and material properties, which may be used to accurately predict the gouging onset velocity. The experiment was designed to confirm an apparent correlation in reported instances of

gouging between velocity and slider strength and hardness, and the corresponding extrapolation to lower relative velocities. It was further intended to pinpoint the gouging onset velocity for a chosen material and a given set of conditions. Lastly, it was intended to create gouges inexpensively and in a manner that could be readily duplicated.

Beginning with a literature review of selected papers on gouging on both rocket sleds and rail guns, Tarcza concluded that all the proposed theories had in common the slipper velocity, stress at the contact surfaces, and sensitivity to material properties. Examining past data, a linear relationship was recognized between gouge onset velocity and yield strength divided by density (Figure 6). Using this relationship, Tarcza postulated that a lead slider impacting against a lead guider would start gouging at 715 fps.

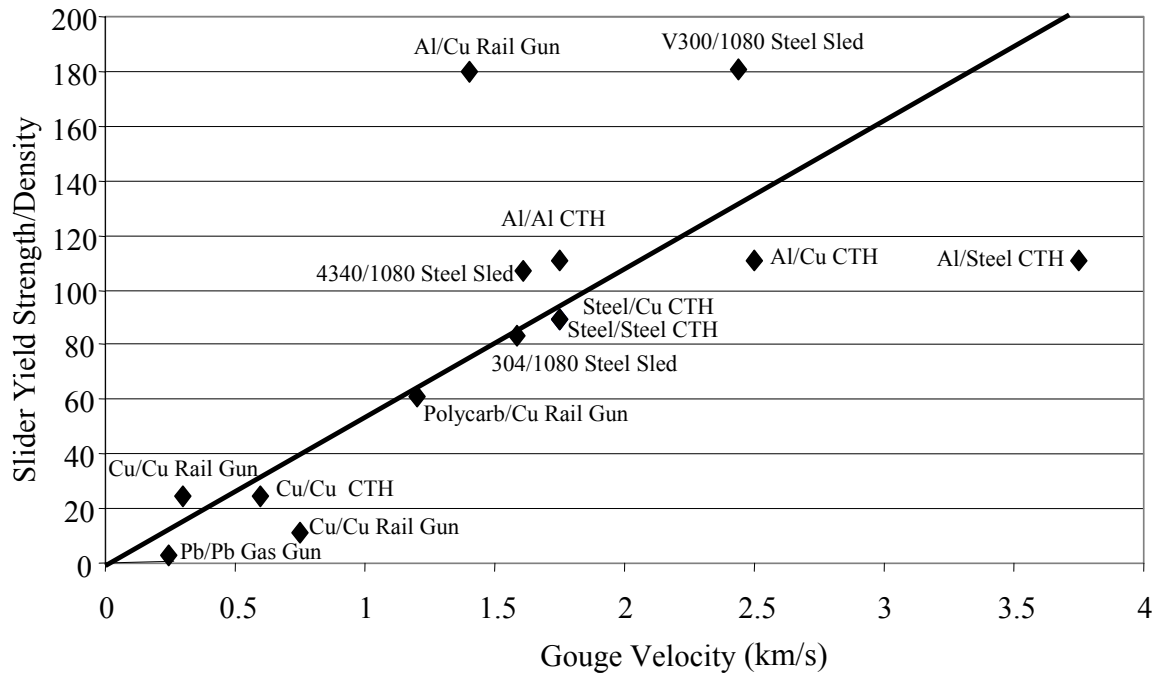


Figure 6. Comparison of Slider Yield Strength and Density to Gouge Initiation Velocity [17]

Tarcza believed that given the proper conditions and materials with appropriate properties, gouging would be possible at velocities other than those at which it has previously been observed. Considering one definition of hypervelocity as the regime in which inertial forces dominate over those deriving from strength of materials, Tarcza searched for a material combination that would exhibit hypervelocity gouging phenomena at relatively low speeds.

Experiments were conducted using a .22-caliber light gas gun, curved surface target in a catch fixture, and instrumentation similar to Graff et al. Using a lead pellet projectile against a lead target, Tarcza found that gouging occurred consistently at sliding velocities above 272 m/s. He examined the resulting wear and impact damage, and found that gouges occurred in the shape of teardrops, ovals, or peanuts. The highest velocities produced the largest gouges. All of the gouges had dull finish, rough or scraped appearance, and raised lip normally associated with gouging. Though most gouges produced seemed to develop solely from a point of incidental slider-guider contact, a few of the gouges instead appeared to result directly from scratches or other pre-existing nonuniformities in the surface of the lead sheet guider. Further, a raised manufacturing seam across the entire width of the sheet used had the opposite effect. Not only did the seam prevent gouging, in every case it seemed to cause an extended period where the slider and guider were not in contact that grew longer with increase velocity. These observations agreed with experimental findings of Gerstle at the Sandia Test Track. Numerous instances of overlapping gouges were observed. In addition, a number of instances were observed where gouges were initiated within the width of a wear track but continued outside of the track. It was found that there is a regime between gouging and

no gouging. Tarcza sometimes observed what he termed to be “incipient” gouging, in which case gouges did not seem fully developed. Tarcza felt that in testing, the instance of gouging must have occurred after a period of somewhat sustained contact between the slider and guider as opposed to a sudden, unexpected material interaction. Neither plate thickness nor the presence of an oxide layer seemed to affect the wear, impact fan, or gouging. Because the gouging impact speed was significantly below material wave speed, Tarcza concludes that gouging is not limited to being a hypervelocity phenomenon.

After use, the pellets were elongated to the rear and their leading edges displayed a protruding, curled lip, which grew more pronounced with increasing velocity. While rearward elongation is the logical result of relative motion forcing slider material to the rear, the surprising lip on the leading edge indicates that material was also being pushed forward ahead of the slider. Tarcza also found that the higher the velocity, the more mass that was lost from the slider. This could be from impact, wear (including against the catch tank after the lead sheet), and/or gouging. No evidence was found of gouging on the slider surface, but significant wear after the last gouge (especially in the catch tank) would have removed any gouging evidence. Because of slider surface marring, it can only be speculated that if slider gouging does occur, it must be less sever than that which occurs on the guider. Otherwise, the cumulative effects of all guider gouges from any given wear track, particularly those with large gouges, should have resulted in far more slider damage than was observed in any recoverable pellet.

The magnitude of normal force generated during slider-guider contact is critical in onset of gouging. The normal force has been attributed to surface asperity impact, gouge

initiating particles, and normal slider velocity components. The fact that an appropriate curvature was needed in lab tests further confirms the requirement for a sufficient amount of normal force for gouges to occur. In reality then, gouging onset velocity is a function of normal force as well as slider material properties. It seems appropriate as well as more accurate to describe gouging and its onset velocity for a given slider material in terms of the normal force required for gouging. If it is presumed that the normal forces which cause gouging are functions of slider characteristics and are transmitted to the guider surface through asperity impact, it follows that the magnitude of transmitted force can be altered by varying the slider mass, the slider normal acceleration, the slider tangential velocity, or any combination of the three. At present there is no data that either quantifies sufficient normal force or specifically relates slider normal force to gouging or the gouging onset velocity.

Numerical Modeling of Gouging. Boehman et al. [18] attempted the development of a computer model to study hypervelocity friction, wear, and gouging at the slider/rail interface. They were able to identify the velocity regimes for stability, but were unsuccessful in implementing gouging criteria.

Numerical work was continued by Barker et al [19] at Sandia National Laboratory in 1987. Using the hydrocodes CSQ and its successor CTH, a model termed the Parallel Impact Thermodynamics (PIT) model was developed to model slider impact. The PIT model involves a slider with a small gap and forty-five degree angled front impacting a gouge initiating asperity, as seen in Figure 7.

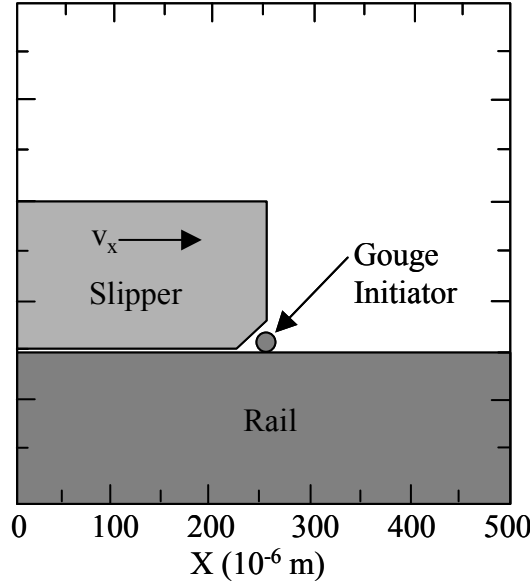


Figure 7. Barker's Model [19]

First, to get an idea of temperatures involved due to friction, it was found that the frictional surface heating of a 30mm diameter steel projectile sliding at 3 km/s in a barrel with a nominal curvature of 1 mil per 10 inches would be expected to result in surface melting of the projectile after 0.002 seconds (0.6 m) of travel and to a depth of 0.67 mm.

Like those before, the researchers felt that gouging was an impact phenomenon and developed a theory and computer model accordingly. The CTH program uses high shock physics characteristics similar to a ballistic impact problem, for which CTH has been successfully used in the past.

They were able to show that a numerical model of high velocity tangential impact, where the slider impacts something in front of it horizontally, could produce simulated gouging under certain conditions. To function properly, two-dimensional models required a gap between the slider and guider, an asperity, and a normal load generated by

giving the leading edge of the slider a forty-five degree angle to impart downward motion to the asperity during impact. Three-dimensional models were used to verify results, and it was found that gouging would not occur with a slipper gap. But gouging did occur if no gap was present. Barker et al. determined that both models confirmed the validity of the PIT model.

Their study found that under the conditions under which gouging may exist due to microasperity impact interaction between a slider and guider, extreme local deformation, heating, melting, and possibly vaporization may occur. Results from the model show the progressive development of a gouge, and also indicate the similarities between gouging modeling and hypervelocity impact problems. The impact of a steel asperity traveling at 2 km/s against a stationary steel asperity will generate a shock pressure of about 5800 ksi, which is about 40 times higher than the 150 ksi yield strength of typical heat treated steel. Their feeling was that conditions permitting, a microasperity impact would result in the development of a growing high-pressure interaction region. Their theory of gouge initiation states generally that the high pressure acts to deform the parallel surfaces that impinge on each other in a continuous interaction that can produce gouges. Barker et al. suggested that this type of interaction would be self-sustaining, and will continue until the slider passes beyond the point of interaction. The researchers also suggest that simultaneous symmetric gouging must occur on the slipper surfaces. They also noted that stress wave propagation, reflection, and relief waves might play a role in gouge development.

Barker et al. conducted a parameter study to try to quantify the physical conditions that must exist when gouging takes place and to verify the validity of assumptions made

for the computer model. By varying the simulation parameters, Barker et al. conclude that decreasing the tendency to gouge can be accomplished by increasing the size of the gap between the slider and rail, increasing the slider yield strength with respect to the guider, make the slider out of plastic, give the slider a small angle of attack with respect to the guider, or decrease the normal load between the slider and guider. Another experiment was run without friction to test Graff et al.'s weld junction theory. Gouging occurred with and without friction. Apparently inertial forces are so dominant that the question of welding is unimportant.

Based on these findings, Barker et al. designed a laminated slider whose features allowed release waves to arrive earlier to decrease pressure in the gouge nucleus, provide some shock absorption through flexibility to decrease peak normal pressure, and provide melt lubrication at high velocity. A slider using this design was tested on a small monorail sled that reached 1.9 km/s and produced no gouges.

In 1991, the use of CTH to perform numerical analysis of gouge development was continued by Tachau [20,21]. Beginning with a literature review, Tachau points out that Barker's theory required a gap, an asperity, and an angled leading edge to impart downward motion of the asperity during impact, and that Barker's models did not include the effects of sliding friction. Tachau's hypothesis was that an oblique impact could generate the environment necessary to form a gouge. Tachau improved upon the PIT theory presented by Barker et al. by eliminating the gap between the slider and guider as well as the gouge initiating asperity from the CTH computer model. Instead, an initial slider velocity component normal to the sliding surface was applied to the model as in Figure 8. This produces impact at highly oblique angles (nearly tangent). Tachau felt

that this would result in the development of antisymmetric humps as described by Abrahamson and Goodier in 1961.

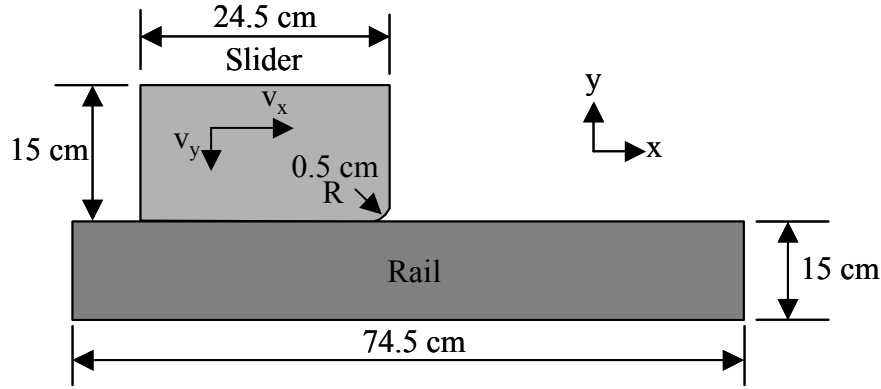


Figure 8. Tachau's Model [20]

The nominal velocities were 2.0 km/s horizontally and 100 m/s vertically. Tachau observed that the crater is somewhat deeper than observed in rocket sled gouges, but this may be attributed to the selected vertical velocity component, which is slightly larger than what might be expected in rocket sled testing. Temperature contours showed high temperatures up to 1800 K resulted from impact and were sustained only at the contact surface. The impacts readily heated the surfaces to near melt conditions. The core pressures were high, on the order of 5000 MPa. Tachau also performed a matrix study of steel and aluminum sliders at different velocities.

He found that a strong pressure core developed by the impact affected whether or not gouging occurred, and that tangential (horizontal) and normal (vertical) velocities were contributing factors. In simulations for a slider and guider both made of steel, he found

that a slider at 2.0 km/s with a 0.1 km/s downward velocity component caused gouging, but one at 1.0 km/s and 0.1 km/s downward did not.

These results lead Tachau to conclude that the temperature at the contact surface must be sufficiently high to cause the materials at and near the contact surface to become viscoplastic, and that the impact condition must be severe enough to ensure the creation of a growing, high-pressure core at the contact surface. He also concluded the heat necessary to produce this high temperature is generated primarily by contact friction and impact, conditions that occur at high speed and large normal loads. Then, when obliquely impacted, the shallow heated zone of softened material allows the formation of antisymmetric deformations described above. Since both the slider and the guider become very hot, antisymmetric deformations would be expected to form on both contact surfaces. If conditions permit a continuous interaction of the heated, viscous layers, a gouge would be initiated in a manner similar to the PIT model. With some reflection on the asperity model, Tachau saw that impact of the slider, with a sloped impact surface, on the asperity provides the vertical momentum or impulse component necessary for gouge formation. This study suggests that the magnitude of the vertical momentum does not need to be large--if the temperature produced by the oblique impact is sufficient to cause melting, and the contact and loading conditions are sustained, eventually a gouge will be formed. Recommendations to mitigate gouging included carefully aligning the entire slider-guider system, designing sliders for aerodynamic stability, and eliminating slider-guider contact while minimizing slider-guider clearance. He also proposes a design for a non-gouging slipper.

Schmitz [22] developed a new software tool based on CTH results to investigate gouging and wear in 1998. The tool predicts slipper wear and gouging phenomena based on empirical data and initial conditions. Experimental testing will be performed to validate the output of the tool. To develop this tool, Schmitz has used CTH running an asperity impact simulation based on Barker's model as shown in [19]. Schmitz has also observed through CTH modeling that growth of the high pressure core in the first four microseconds of impact predicts the formation of a gouge, while if the pressure core does not grow, no gouge will form. Most importantly, Schmitz was able to correlate the gouge velocities for different slider and rail materials in CTH with experimental and test track data as presented in Figure 9.

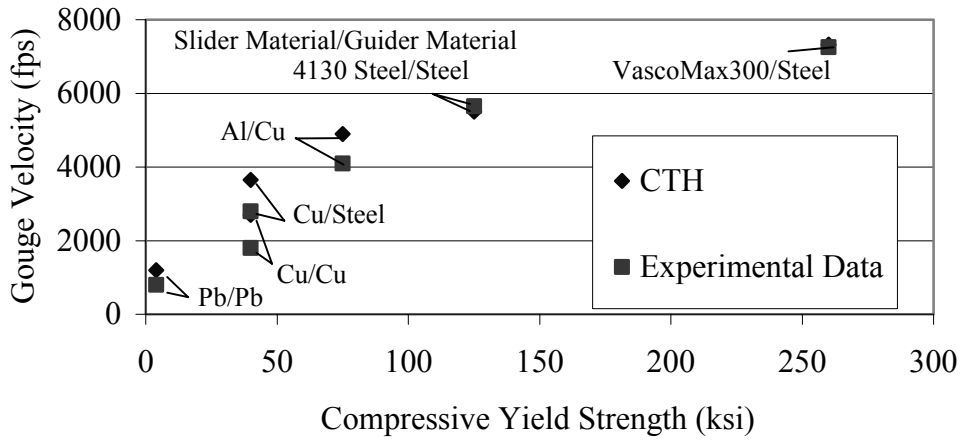


Figure 9. Validation of CTH to Experimental Data [22]

The most obvious limitation of previous computational works is that an elevated thermal environment (due to aerodynamics or friction) was not included in the simulations. Furthermore, size and shape of the sliders simulated were not

representative of real sliders, making it difficult to conclusively compare numerical results to test track data.

Rail Gun Gouging. In high velocity guns such as rail guns and two stage gas guns, hypervelocity gouging is also found at the gun barrel/projectile interface. In 1989, Barker et al. [23] reviewed the data collected in Susoeff and Hawke's 1988 report [24] on rail gun gouging and then acknowledged that the source of gouging damage was still uncertain; the experiments that had produced gouging were designed to improve rail gun performance rather than to study gouging. Barker et al. suggested that molten droplets of the aluminum commutator "impinging" at low angles into the rails and "digging in" might have caused the gouging damage. They reasoned that the higher energy levels used on the last five shots likely resulted in complete vaporization of the aluminum commutator and thus no gouging, whereas earlier shots that produced gouging did so because of incomplete vaporization of the foil.

Barker et al. used the PIT theory to conduct a CTH hydrodynamic code parameter study to predict the conditions under which gouging can occur. In the study, they evaluated all possible slider-guider combinations of copper, steel, aluminum, and plastic at velocities from 0.5 to 12 km/s. The results were examined to determine whether the initial microasperity impact at a slider-guider interface would result in a growing, stable, or decaying interaction region; a growing interaction region would indicate the formation of a gouge. Barker et al. determined that materials that gouge each other do so only within a certain range of velocities. They also determined that there are both upper and lower gouging threshold velocities, although the upper threshold has never been experimentally observed. When sliding exceeds twice the wave velocities of the

interacting materials, gouging does not occur. This is apparently because there is insufficient time for material to be continually pushed up in front of the interaction zone and the reaction dies out. They saw that higher yield strengths raise the lower gouging threshold (and may lower the higher threshold as well). Computer calculations infer that a nearly steady “stream of gas” emanates from the leading shoulder of plastic sabot projectiles because of shock vaporization due to micro impacts (what is normally described as blow-by). Finally, they found that a ten-degree angle of attack on the slider reduces the stream of gas and the tendency for gouging to occur.

Other occurrences of rail gun related gouging are reviewed in the previously discussed works by Tachau and Tarcza [25-28].

Sled Analysis. Because of the difficulty involved in recreating gouging, much work has been performed analytically. In 1968, Korkegi and Briggs [29,30] developed a model to perform a two-dimensional analytical study of the steady state flow through the slipper/rail gap. They calculated the flow conditions and heat flux by dividing the gap flow into four regions: a laminar flow near the stagnation point at the front of the slipper, a turbulent boundary layer region before the upper and lower boundary layers merge, a merged region, and a Couette flow asymptote (flow between a moving plate and parallel stationary plate).

They found that air flowing through the gap is shock compressed to high pressure and temperatures resulting in high lift loads and high heat rates on the inner surface of the slippers. At speeds between Mach 5 and 10, the aerodynamic heating caused by compression and confinement of the shock waves to the inner slipper surface are as high as those at the leading edge stagnation points (similar to re-entry vehicles), and that at

higher velocities these heat rates are comparable to those of sliding friction. At 10,000 fps, heating rates were about 10^4 Btu/ft²-sec. This indicates that aerodynamic heating to the slipper when a gap is present is equally as important as the frictional heating produced when no gap is present.

They developed an expression of gap pressure p as a function of the distance from the slipper leading edge x from one-dimensional isentropic (constant entropy) flow relations relating effective area to local Mach number and pressure as follows:

$$\frac{p(x)}{p_\infty} = \left(\frac{(\gamma + 1)M_\infty^2}{2 + (\gamma - 1)M(x)^2} \right)^{\frac{\gamma}{\gamma-1}} \left(\frac{\gamma + 1}{2\gamma M_\infty^2 - (\gamma - 1)} \right)^{\frac{\gamma}{\gamma-1}} \quad (2)$$

where p_∞ is the pressure at the free stream, $M(x)$ is the Mach number as a function of the downstream distance from the slipper leading edge x , M_∞ is the Mach number at the free stream, and γ is the ratio of the specific heats. The model is valid from the leading edge of the slipper to the emergence location of the upper and lower boundary layers. The model was developed for $M_\infty \gg 1$, and should therefore be valid in the velocity regime being studied. This equation should also be valid for the helium environment using the proper Mach number and value of γ .

Among Korkegi and Briggs' conclusions were that the flow conditions in the gap are almost independent of M_∞ for $M_\infty \geq 4$, and that while the slipper wall is cold, the pressure in the gap decreases from the leading edge to the trailing edge, but as the slipper heats up the gradient diminishes until a condition of constant pressure would result in the limit of adiabatic wall temperature. Additionally, since the gap pressure varies in the same direction as the gap size, a decrease in gap height results in a drop in the gap pressure and

vice versa, hence the configuration is statically unstable. This results in the intermittent bouncing of the slipper metal to metal and a major contributing factor for the tendency of the monorail sled to “jump”.

Load Analysis. Abrahamson and Goodier [31] observed that humps precede moving loads on layers of soft or viscous material, similar to a hump deformation being driven in front of a rolling pin when a slab of bread dough is being rolled out. They concluded that this behavior is the result of inelastic behavior of the layer. If the material were elastic, the deformation would be symmetrical with equal bumps upstream and downstream of the load. For a stationary viscous material, the surface profile changes due to penetration of the load. If the penetration is stopped and the material is given a horizontal velocity, the leading hump is drawn under the penetrating load. The actual profile then, is determined by the combination of penetration and plastic flow. For a symmetric loading of an incompressible material, the surface displacement, which is significant only near the load, creates the characteristic hump.

Cole and Huth [32] developed a mathematical model for the stress field produced by a moving load on an elastic half space and showed that the stress field is symmetric, a finding backed by the analysis of Gerstle and Pearsall [33]. Singularities in the stress and strain were found as the load velocity approached the Rayleigh wave speed. Chao [34] showed the existence of a pressure wave, a shear wave, and a Rayleigh surface wave. Adler and Reismann [35] modeled the rail as an elastic plate strip and eliminated the singularity in the displacement solution by adding small linear damping terms to the equations of motion. Additional moving load analyses have been performed by Criner and McCann [36], Kenny [37], Florence [38], and Choros and Adams [39].

Methods for Gouging Mitigation

Since gouging results from the antisymmetric deformation of the heated zone of softened material, the process may be mitigated by the use of special coatings to protect the surface from the high heating environment. Coatings have been used in the past, and have resulted in fewer occurrences of gouging.

Two types of coatings are available, refractory and ablative. While these coatings are typically intended to protect various parts of the sled from thermal effects, they may also be useful to protect the rail surface. Refractory coatings such as tantalum, nickel-aluminum, zirconium oxide, tungsten, and cobaltech have been used on rocket sleds in the past [9]. Tantalum sheets have been used to protect slipper leading edges but the mounting hardware had failed in the severe thermal environment. The other refractory coatings are applied in layers using a plasma sprayer. These plasma sprayed coatings offer very good protection, however, great care needs to be taken in their application. A reliable interlock between layers must be established to avoid the formation of cracks, which may be initiated by the difference in the thermal expansion coefficients of the metal surface and the coating.

Ablative coatings include Teflon, carbon-carbon, and carbon-phenolic coatings. These have been used to protect sled components at velocities greater than Mach 6. Teflon has been used, but its effectiveness is surpassed by the carbon-carbon. Both of these, however, are of limited usefulness under high shock loading conditions. Carbon-phenolic layers are applied in sheets, using epoxy to bond and stack the layers. The use of ablative materials can result in minor configuration changes, which are undesirable and could be detrimental to operation [9].

A proposed slipper design by Barker et al uses a laminated slider design composed of alternating layers of plastic and high strength, high toughness steel at a 10-degree angle of attack [1912]. This design combines several gouge mitigating factors, and was first tested in 1987 at 1.9 km/s without gouging the rail. Tachau [20] also proposed a slipper design that uses a corrugated contact surface, intended to disrupt the growth of the high-pressure core.

Summary of Previous Research

In the work on gouging done to date, the cause to which gouging has been directly attributed is impact initiated by debris on the guider due to environment, sled deterioration, or alignment defects, and bouncing motion or vibration of the slider against the guider. After impact, proposed mechanisms that cause the gouge to develop have included thermoplastic shear, hypervelocity microasperity impact between the slider and guider contact surfaces, shock induced pressure accumulation at the slider-guider interface, and the existence of viscoplastic materials at the contact surfaces.

Sled impacts involving large slippers are subject to high normal loads due to aerodynamics and structural dynamics coupled with a large mass. Rail gun projectiles are much smaller, lighter, and more precisely balanced, resulting in relatively small normal loads. Laboratory gas guns have high impact angles but small mass compared to sleds. Despite the differences and variety of causes and mechanisms suggested and the three different systems (sled runs, rail guns, and laboratory tests) involved, there are common threads in these findings. Slider velocity, stresses at the contact surface as a function of slider normal force, and material properties of the slider and guider are

repeatedly identified as important factors that determine if gouging will occur. Whether imposed by asperity impacts or the contact between deformed slider and guider surface layers, it is generally agreed that some minimum amount of normal force at a slider-guider interface, relative to the properties of the materials involved, is likely required for gouging to occur. It seems that if the normal forces at a slider-guider interface lead to an accumulation of shock induced pressure at the point of contact, phase transformations, softening, melting, and possibly vaporization and gouging of both slider and guider surfaces may occur.

III. Methodology

This chapter presents the methods that are used to simulate gouging. This includes discussion of the use of hydrocodes and hydrocode theory, governing equations, and physical aspects of the gouge environment that need to be considered.

Using Hydrocodes to Simulate Gouging

Numerical modeling is a critical technique to explore a physical phenomenon. It is a powerful tool that can provide insight and help explain phenomena observed in experiments. Models can be used to test hypotheses concerning fundamental mechanisms and can be used in a systematic application to obtain the influence of variables. They can be used to extend experimental data by performing parametric variation of variables. They can be used as an alternative to experiments and may be the only method to examine extreme high velocity regimes beyond the capability of current launch techniques. Also, by simulating experiments numerically, strains, strain rates, velocities, displacements, stresses, etc., can be determined for any location and for any time [40]. This chapter describes methods to model and study gouging including the governing equations, a description of hydrocodes and hydrocode theory, and physical aspects that need to be considered when modeling gouging.

Slipper impact and subsequent gouging are characterized by colliding, sliding, and eroding surfaces. The colliding materials are in the plastic regime immediately after impact initiation, are subjected to high strain rates, and behave like fluids [41]. Barker et al [19] at Sandia National Laboratory were the first to realize that the onset of gouging is similar to hypervelocity ballistic impact problems, which have been more

extensively studied. Both high velocity impact and gouging consist of material under high bearing pressure, high temperature, and contact of two surfaces. Even though the problems are different, the modeling of the physics is similar and the analysis of gouging may be performed following established methods used in ballistic impact problems.

Classical continuum mechanics describes the dynamics of continuous media with a set of differential equations established through the application of the principles of conservation of mass, momentum, and energy from a macroscopic point of view. The conservation laws relate material density, velocity, specific total energy, the stress tensor, and external body forces per unit mass. Because the three conservation equations have too many unknown parameters, an additional equation called the equation of state (EOS) is needed. The equation of state accounts for compressibility effects and irreversible thermodynamic processes. This equation relates the density (or volume) and internal energy (or temperature) of the material with pressure. In addition, a constitutive equation is needed to describe the particular nature of the material by relating the stress in the material with the amount of strain required to produce this stress. The constitutive model permits the stress to be a function of strain, strain-rate effects, internal energy, and damage. The constitutive equations in conjunction with the equation of state can be used to give an accurate estimate of stresses. The result is a set of coupled, nonlinear equations that in general must be solved simultaneously, considering boundary and initial conditions [42].

Hydrocodes are computer programs that are primarily suited for solving this set of equations. An overview of hydrocode solution methods will be discussed in subsequent paragraphs, and thorough descriptions can be found in works by [40-43]. In general,

many different equations of state and constitutive models are available. Of these, several are developed specifically for large deformation and high strain-rate impact environments such as the gouging problem. Hydrocodes allow the user to specify or even create models to be used.

The extreme pressure and thermal conditions involved in the sled environment coupled with the phenomena of gouging result in large material deformations. In order to model the gouging process, a nonlinear material response is necessary. An inelastic constitutive relation is needed as well as suitable equations of state. Since the surface temperature of the slider and rail increases during sliding contact, the extreme heating conditions produce viscoplastic materials where a shallow heated layer of soft material allows antisymmetric deformation as found by Abrahamson and Goodier [31]. Thus, a viscoplastic constitutive relationship is required to predict the onset of gouging.

As sliding velocity increases, the temperature of the slider and/or rail surfaces may reach the melting point creating a liquid interface with greatly reduced frictional forces and coefficient of friction. Viscoshearing of the thin melted layer dissipates energy, which causes additional internal heating of the contact surfaces, resulting in further surface melting. Under these thermal circumstances, a viscoplastic constitutive relation is necessary. The viscoplastic Bodner and Pardom constitutive model [44] is often used to model high strain rate material response and hypersonic ballistic impact problems. Other viscoplastic constitutive relations include Johnson-Cook [45], Zerilli-Armstrong [46], and Steinberg-Guinan-Lund [47-49].

Using these relations, a model can be constructed and solved numerically to investigate the gouging phenomena. With such models, researchers may explore the

effect of slipper geometry, velocity (forward and vertical), different material hardness, strain rate, and the effect of the material yield strength on the onset of gouging.

Introduction to Impact Dynamics

Impact dynamics has two features that distinguish it from classical mechanics involving rigid or deformable bodies under quasi-static conditions. The first is the importance of inertia effects, which must be considered in all of the governing equations based on the fundamental conservation laws of mechanics and physics. In the hypervelocity regime, hydrodynamic pressure dominates the behavior of solids undergoing high velocity impact. At these very high pressures, metals behave like inviscid fluids [50]. Consideration of the material behavior under these conditions and under high rates of loading must be undertaken.

Secondly, the role of stress wave propagation in the analysis of problems becomes important. This includes recognizing that most impact events are transient phenomena where steady-state conditions do not exist. For high velocity impacts, stresses will exceed the yield strength and inelastic as well as elastic waves will be generated. In order to bear stress, solid materials must deform. Compression pushes particles closer together, which takes time and requires relative motion. When subject to an instantaneous pressure, the pressure is initially entirely supported by inertia. As the particles near the pressure begin to move, they generate a stress and begin to accelerate the particles they are moving toward, and this becomes the front of the stress wave. These waves propagate through materials, changing particle velocities and the state of stress and strain. Once the stress between adjacent particles becomes equal to the applied

pressure, relative motion ceases and the pressure is supported entirely by compression. In most solids, the wave fronts are only a few molecules thick and can be treated as discontinuities. The initial stress wave generated by the impact propagates into unstressed material at the elastic wave velocity, which is $c = \sqrt{\frac{d\sigma/d\varepsilon}{\rho}}$, where $d\sigma/d\varepsilon$ is the local slope of the material's stress-strain curve in the elastic regime and ρ is the density [41]. Plastic stress waves travel at the plastic wave velocity, which is given by the same equation above but where $d\sigma/d\varepsilon$ is the local slope of the stress-strain curve in the plastic regime. In traditional applications, the wave propagation occurs so much faster than material deformation that it may be considered to be instantaneous, such that when a load is applied, the entire domain is immediately affected. In hypervelocity cases, as the material response nears or exceeds the wave velocity, this is not necessarily the case. In the rail/slipper gouging problem, the material sound speed is roughly twice the speed as the 10,000 fps sled velocity. At low velocity, one may consider that loads applied to an 8 inch long slipper effect the whole slipper. But as the sled approaches 10,000 fps, the slipper is displaced 4 inches before the load is applied across the whole slipper. In this case, the application of stress is dynamic and can no longer be considered to occur instantaneously.

Thorough descriptions of these phenomena involved can be found in impact and high velocity metal working textbooks [42, 50-52].

Overview of CTH

The present gouging research has been performed using the hydrocode CTH (CHARTD to the Three Halves), a family of codes developed at Sandia National

Laboratories for modeling complex multi-dimensional, multi-material problems that involve large deformations and strong shocks. A brief description of CTH is included here, and details will be presented in following discussions.

CTH uses a two-step, second-order accurate Eulerian solution algorithm to solve the governing equations of mass, momentum, and energy conservation [53]. CTH contains constitutive models that include strain and strain-rate effects, and is well suited for problems pertaining to large distortions such as those considering impact. Models are included for strength, fracture, porous materials, high explosives, and a variety of boundary conditions. Viscoplastic or rate-dependent models of material strength formulations of Johnson-Cook, Zerilli-Armstrong, and Steinberg-Guinan-Lund are standard options [54].

CTH contains two major equation of state packages that can be used to investigate problems pertaining to shock propagation, melting, and/or vaporization, such as those that occur in hypervelocity impact. These are the Analytic Equation of State (ANEOS), and SNL-SESAME, a tabular EOS. The analytic package ANEOS includes Mie-Grüneisen, Jones-Wilkins-Lee, and ideal gas equations of state. The SNL-SESAME tabular data is based on experimental data and may include multiple liquid-vapor, liquid-solid, and solid-solid transitions [55].

Other useful features of CTH include a high-resolution interface tracker, and pre- and post-processors. CTH has also been adapted for use on parallel computing systems, reducing solution time for large projects.

Conservation Laws

The conservation of mass, momentum, and energy are the fundamental principles that are assumed to govern the motion of any continuum [43]. The integral form of the conservation of mass equation in Lagrangian coordinates can be expressed as:

$$\frac{d}{dt} \int_{\beta_t} \rho dV = 0 \quad (3)$$

where t is the time, ρ is the mass density, β_t is the position the Lagrangian body occupies at time t , and V is the cell volume. This form of the equation states that the mass of the body does not change with time.

Conservation of momentum states that the rate of change of momentum of a body is equal to the resultant of the applied forces:

$$\frac{d}{dt} \int_{\beta_t} \rho U dV = \int_{\partial\beta_t} n \bullet \Sigma dA + \int_{\beta_t} \rho B dV \quad (4)$$

where U is the velocity, Σ is the stress tensor, $\partial\beta_t$ is the boundary of β_t , B is the body force per mass, n is the unit normal vector on the surface, and \bullet is the dot product. This means that the change of momentum with time (or force) is equal to the force resulting from the stress plus the change in momentum due to any body forces.

The energy conservation principle states that the rate of increase of energy of a body is equal to the rate at which the applied forces do work on the body:

$$\frac{d}{dt} \int_{\beta_t} \rho E dV = \int_{\beta_t} \Sigma \bullet \nabla U dV + \int_{\beta_t} S dV \quad (5)$$

where E is the specific internal energy and S is an internal energy source per volume per time [56]. This equation states that the change in energy per time results from the energy

changes due to the stress field plus any energy sources. In other words, the change in energy is the amount of energy entering β_t minus the energy leaving plus internal sources.

Equation of State (EOS)

In the gouging problem, it is important to model the materials involved and solve for the thermodynamics and material response. Material modeling may be categorized into three areas: the equation of state, the constitutive relations, and failure [40].

The reliability of computer shock simulations depends on accurate thermodynamic models for the associated materials. Strong shock simulations require sophisticated and accurate models of the thermodynamic behavior of materials. Phase changes, nonlinear behavior, and fracture can be important for accurate predictions.

Materials in thermodynamic equilibrium maintain a relationship between thermodynamic variables, such as pressure, as functions of mass density (or specific volume v) and temperature. Pressure is a component of total stress, which can be broken into two components: spherical stress and deviatoric stress. Pressure is simply the spherical stress component, and is represented by:

$$\sigma_m = \frac{\sigma_x + \sigma_y + \sigma_z}{3} = \frac{\sigma_{ii}}{3} \quad (6)$$

The relationship between the pressure, specific volume, and temperature is known, in short, as the p - v - T relationship. An example of a p - v - T surface including phase transitions is shown in Figure 10.

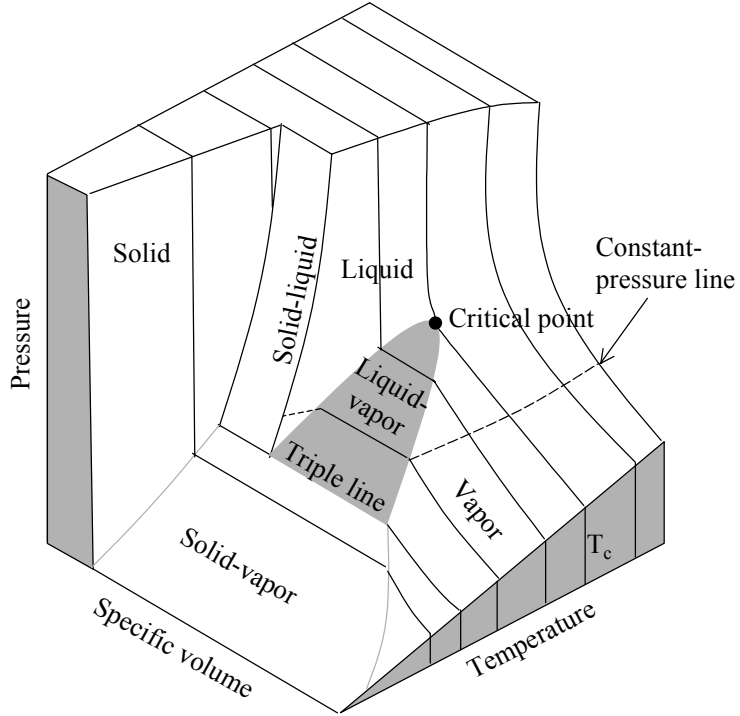


Figure 10. Example of a p - v - T Surface [57]

The p - v - T relationship can be expressed in three basic ways: graphically, such as phase diagrams and surfaces like Figure 10, as an analytical equation called an equation of state (EOS), or tabularly (such as steam tables). Hydrocodes use either an analytic equation of state or a table.

In high strain, high strain-rate problems, the behavior of materials are normally modeled by decomposing the stress into spherical stress (pressure) and deviatoric stress (plasticity). The two formulations can be treated independently because plastic flow has been found to be independent of pressure at low pressures in solids. The hydrostatic behavior is also assumed to be strain-rate independent. The mathematical relationship of the hydrostatic components of stress (pressure) and strain (density) is handled by the equation of state. It must also consider temperature (or energy) [50].

Because the three conservation equations have more unknown parameters than equations, the pressure, density, and temperature relations provided by the equation of state (EOS) are coupled with the solution of the conservation equations. Furthermore, when considering the presence of shock waves, the EOS may include the pressure, density, and temperature relationships across a shock wave. In this case, the EOS also deals with shock velocity, U_s , and particle velocity, u_p .

The EOS is usually not considered in a solid mechanics solution because pressure, volume, and temperature changes are usually not significant and can be considered as constants, reducing the number of variables that need to be solved. But in fluid flow and impact dynamics, the materials are compressible and pressure, which is spherical stress, can vary. In the hypervelocity regime, the form of the equation of state is important in predicting the dynamics, and several forms of the equation of state have been specialized for this purpose. Hydrocodes typically allow the user to choose appropriately from several of these EOS models. To better understand what the EOS models do and how they function, two common equation of state packages used in hydrocodes are described below.

Mie-Grüneisen Equation of State. A simple and well-known representation of an equation of state is the ideal gas equation:

$$pv=RT \tag{7}$$

where p is the pressure, v is the volume, T is the temperature, and R is a constant. When considering the response of solids and the propagation of shock waves, an equation of state more detailed than Equation 7 is necessary to determine state conditions. One

method of doing so is the Mie-Grüneisen equation of state, which is specifically intended to deal with relating the pressure, density, and temperature across a shock wave.

Shock waves form when disturbances propagate with a velocity greater than the sound speed. The Rankine-Hugoniot jump conditions express the conservation of mass, momentum, and energy in a steady one-dimensional shock wave. For a material initially at rest, with initial density ρ_0 , pressure P_0 , and energy E_0 , the shock conservation equations (jump conditions) are [55]:

$$\mu = 1 - \frac{\rho_0}{\rho} = \frac{u_P}{U_S} \quad (8)$$

$$P_H = P_0 + \rho_0 U_S u_P = P_0 + \rho_0 U_S^2 \mu \quad (9)$$

$$E_H = E_0 + \frac{u_P^2}{2} = E_0 + \frac{\mu(P_H + P_0)}{2\rho_0} \quad (10)$$

where, ρ , P_H , and E_H are the density, pressure, and energy of the shocked material, U_S is the velocity of the shock wave as it moves through the undisturbed material, and u_P is the particle velocity behind the shock front. In CTH, U_S can be represented by a quadratic function of u_P , or a special modified form to model nonlinear behavior at low pressures. The curve that passes through all points on the p - v - T surface that satisfy these jump conditions (Equations 8, 9, and 10) is called the Hugoniot. While this method is effective in describing the shock wave motion, it gives little information about material states, so it will be combined into an equation of state as described below.

The Grüneisen function Γ is defined as the dependence of pressure on internal energy at constant density, $\Gamma = \rho^{-1}(\partial P/\partial E)_\rho$, where the subscript ρ indicates constant density. The Mie-Grüneisen approximation assumes that Γ is a function only of density, giving

$\Gamma = \Gamma_0 \rho_0 / \rho$. This assumption leads to a linear relationship between pressure and energy at constant density:

$$P(\rho, E) \approx P_R(\rho) + \Gamma(\rho)\rho[E - E_R(\rho)] \quad (11)$$

where P_R and E_R are the pressure and energy along a reference curve.

When the temperature is needed, Mie-Grüneisen models normally assume that the specific heat $c_v = (\partial E / \partial T)_v$ is a constant, which gives:

$$E(\rho, T) = E_R(\rho) + c_v[T - T_R(\rho)] \quad (12)$$

where T_R is the temperature on the reference curve.

Using the Hugoniot as the reference curve and the Mie-Grüneisen approximation, the Mie-Grüneisen equation of state gives pressure P and energy E by [55]:

$$P(\rho, E) = P_H(\rho) + \Gamma_0 \rho_0 [E - E_H(\rho)] \quad (13)$$

$$E(\rho, T) = E_H(\rho) + c_v[T - T_H(\rho)] \quad (14)$$

where P_H , E_H , and T_H are the Hugoniot pressure, energy, and temperature, and ρ_0 is the initial density of the Hugoniot. The Grüneisen parameter Γ_0 and specific heat c_v are taken to be constants. P_H and E_H are computed from Equations 8, 9, and 10 (jump conditions) with $P_0 = E_0 = 0$.

The Hugoniot temperature T_H is obtained by deriving a differential equation from the first law of thermodynamics, Maxwell relationships, and the Grüneisen equation. Detail of this derivation can be found in [42]. The solution of this differential equation is:

$$T_H = \frac{(E_H - E_C)}{c_v} = e^{\Gamma_0 \mu} \left[T_0 + \frac{1}{c_v} \int_0^{\mu} e^{-\Gamma_0 \mu} \mu^2 U_S \left(\frac{dU_S}{d\mu} \right) d\mu \right] \quad (15)$$

where E_C is the energy on the zero-Kelvin isotherm. Using this expression, the Hugoniot temperature is found numerically.

Tabular Equation of State. Although simple forms can be represented analytically as an equation, tabulation allows the use of sophisticated models that are too complicated to be incorporated into analytic formulas. Tabular equation of state models are powerful tools that use experimental material data to predict thermodynamic states. These tables are created using the empirical data and use interpolations and extrapolations. A good tabular EOS can give valid results over a much wider density-temperature range than analytic models by capturing a number of chemical and physical phenomena that affect thermodynamic behavior, such as electronic structure, nuclear thermal motion, phase transitions, chemical reactions, and thermal electronic excitation and ionization [55]. For iron and iron-like alloys that will be examined in this research, CTH contains a tabular model developed by Sandia National Laboratories known as the SESAME tabular EOS for iron. This model includes four solid phases (alpha, gamma, epsilon, delta), melting, and vaporization. It agrees well with most experimental data, including impact and penetration experiments and wave profile measurements, which show multiple shock behavior [55,58,59].

Constitutive Equations

When a code is used to model material response (strain) to an applied stress, constitutive models are used to define the equations for the stress and strain relationships in a material [60]. If stresses above the yield stress will be encountered, then the constitutive model needs to be able to account for the yield point and the onset of

plasticity. Constitutive models are used to define the equations for the stress and strain relationships in a material. These models can include the effects of temperature, large deformations, and high strain rates.

Some well-known examples of constitutive models include elastic-plastic, elastic-perfectly-plastic, perfectly plastic, and linearly-elastic-perfectly-plastic models. While these simple models are available in most hydrocodes, to solve the high speed, high temperature, large deformation, high strain-rate gouging problem, more advanced models need to be considered of the following form:

$$\sigma_{ij} = f(\varepsilon_{ij}, \dot{\varepsilon}_{ij}, T) \quad (16)$$

where σ_{ij} is the stress tensor, ε_{ij} is the strain, $\dot{\varepsilon}_{ij}$ is the strain rate, and T is the temperature. Some common rate dependent deformation and fracture models include:

- Johnson-Cook viscoplastic model for rate dependent plasticity
- Zerilli-Armstrong model for rate dependent plasticity
- Steinberg-Guinan-Lund model for viscoplasticity
- Johnson-Holmquist ceramic model
- Bammann-Chiesa-Johnson viscoplastic model

Asay and Kerley [61] provide additional information on both the EOS and constitutive modeling.

Johnson-Cook Viscoplastic Model. In the Johnson-Cook model, the material is treated as elastic when the principal stresses are small. As the stress increases to a specified value, a function modeling viscoplastic behavior is used. The implementation

of this model establishes a stress function called effective stress. This effective stress is represented as the scalar function [42]:

$$\sigma_{\text{eff}} = \frac{1}{2} \sqrt{2[(\sigma_1 - \sigma_2)^2 + (\sigma_2 - \sigma_3)^2 + (\sigma_1 - \sigma_3)^2]} \quad (17)$$

where σ_1 , σ_2 , and σ_3 are the principal stress components at a point.

The model uses an empirical relationship for the yield stress, Y , in the plastic region [45,62]:

$$Y = [A + B(\varepsilon^p)^n][1 + C \ln \dot{\varepsilon}^*][1 - T^{*m}] \quad (18)$$

where ε^p is the equivalent plastic strain, $\dot{\varepsilon}^* = \dot{\varepsilon}/\dot{\varepsilon}_0$ is the dimensionless plastic strain rate for $\dot{\varepsilon}_0 = 1.0 \text{ s}^{-1}$, and T^* is the homologous temperature $\frac{T - T_r}{T_M - T_r}$, where T is temperature, T_r is room temperature, and T_M is the melt temperature. The material dependent constants A , B , C , n , and m are empirically determined. This model is essentially a mathematical fit to experimental data.

The effective stress, σ_{eff} , is compared to the yield stress, Y . When $\sigma_{\text{eff}} < Y$ the material is totally elastic and no viscoplastic behavior is considered. When $\sigma_{\text{eff}} > Y$ the material has entered the viscoplastic region and the Johnson-Cook model is initiated.

In Equation 18, the first group of terms in brackets gives the stress as a function of strain; A is the yield stress and B and n represent the effects of strain hardening. The second and third expressions represent the effects of strain rate and temperature, respectively. In this formulation, if the strain and strain rate are very small, and the temperature is near room temperature, Equation 18 reduces to $Y = A$, where A is the nominal yield stress. As either strain or strain rate begin to increase, the value for Y also increases. It is important to recognize that as the temperature approaches the melting temperature, the temperature dependent term goes to zero, driving the expression for Y to

zero. Thus at the melting temperature, there is no longer any elastic region, and stress cannot be supported.

Steinberg-Guinan-Lund Model. The Steinberg-Guinan-Lund (SGL) model predicts the viscoplastic response of various materials, principally metals, based on a theoretical consideration of thermally activated dislocation mechanics [47-49,60]. This model again compares the effective stress to a yield stress function. The strain-rate dependent form of the SGL model defines the yield stress as:

$$Y = \left[Y_T(\dot{\varepsilon}, T) + Y_A f(\varepsilon^p) \right] \frac{G(P, T)}{G_0} \quad (19)$$

where the components $Y_A f(\varepsilon^p)$ and Y_T are defined by

$$Y_A f(\varepsilon^p) = Y_A \left\{ 1 + \beta (\varepsilon^p + \varepsilon_i) \right\}^n \quad (20)$$

and

$$\dot{\varepsilon}^p = \left(\frac{1}{C_1} \exp \left[\frac{2U_K}{T} \left(1 - \frac{Y_T}{Y_p} \right)^2 \right] + \frac{C_2}{Y_T} \right)^{-1} \quad (21)$$

In these equations, P and T are the pressure and temperature, ε^p and $\dot{\varepsilon}^p$ are the equivalent plastic strain and its time derivative, Y_A is the yield stress at the Hugoniot elastic limit, $f(\varepsilon_p)$ is the work-hardening function with β , ε , and n used as fitting parameters. G_0 is the initial shear modulus, Y_p is the Peierls stress, which is the minimum amount of stress required for a dislocation to move through a crystal lattice, and $2U_K$ is the energy necessary to form a pair of kinks in a dislocation segment. The quantities C_1 and C_2 are defined in terms of various dislocation mechanics parameters and are specific to the material being modeled [60]. Two limits are imposed in this model:

$$Y_A f(\varepsilon^p) \leq Y_{\max}^{\circ} \quad (22)$$

and

$$Y_T \leq Y_P \quad (23)$$

where Y_{\max}° is the work hardening maximum in the rate dependent version of the model.

The rate independent model is a special case of the rate dependent form with Y_T set to zero and the following limit applied:

$$Y_0 f(\varepsilon^p) \leq Y_{\max} \quad (24)$$

The significance of each of the material constants is described in Table 1.

Table 1. Parameters for the Steinberg-Guinan-Lund Constitutive Model [47,48]

Category	Parameter	Description
Initial Conditions	ρ_0	Initial density
	G_0	Initial Shear Modulus
	Y_0	Initial Yield Stress
Pressure and Temperature Dependence of the Shear Modulus	A	Pressure Dependence of the Shear Modulus
	B	Temperature Dependence of the Shear Modulus
Work Hardening	β	Work Hardening Parameter
	n	Work Hardening Parameter
	ε_i	Initial Plastic Strain
	Y_{\max}	Work Hardening Maximum
Melt	Γ_0	Initial Value of Grüneisen's Gamma
	a	Coefficient of the Volume Dependence of Gamma
	T_{m0}	Melt Temperature at Constant Volume
Rate Dependence	C_1	Exponential Prefactor in Rate-Dependent Model
	C_2	Coefficient of Drag Term in Rate-Dependent Model
	U_K	Activation Energy
	Y_P	Peierls Stress
	Y_A	Athermal Yield Stress
	Y°_{\max}	Work Hardening Maximum in Rate-Dependent Model

Both the Johnson-Cook and Steinberg-Guinan-Lund constitutive models assume isotropic, linear elastic response of the material. At the beginning of the call to these models in CTH, the deviatoric stress is calculated from a stress rate equation assuming the entire strain rate is elastic. A von Mises yield surface is constructed using the yield stress model from the Johnson-Cook or Steinberg-Guinan-Lund model, and a check is conducted to see if the predicted deviatoric stress is outside of the yield surface. If the stress is outside, the model returns the stress state to the yield surface along a radial (referred to as the “radial return method”) and the extent of distance between the predicted state and the final return state is proportional to the plastic strain rate. This approach is outlined in detail in [63] and [64].

Failure Models

In addition to the deformation modeled by the constitutive equations, other damage, failure, and fracture models may be used to predict at what point a specified material should fail and its failure mode.

The failure method implemented in the current research is based on maximum pressure and void insertion. Each material is assigned a minimum pressure and a relaxation pressure. For each cell containing material, the pressure of each material in the cell is compared with its minimum pressure. If the pressure drops below the minimum value of any material present, then the material is assumed to have fractured. Once fracture is determined to occur, pressure of the failed material(s) is reduced to the relaxation pressure by introducing a void into the cell or increasing the volume of void already present. To relax the pressure of a material in a fracturing cell, a call to the

equation of state is made to determine the derivative of pressure with respect to density at constant internal energy. This is used to estimate the new density required to reduce the magnitude of the pressure to the relaxation value [54].

Solution Methods for the Governing Equations

Solution of the governing equations is the core purpose of numerical solvers like hydrocodes. Several different methods to compute the solution to the equations have been developed, including finite difference, finite volume, and finite element methods. Each of these methods utilizes spatial discretization of the problem space and solving the governing equations in each of the new spaces. In general, these techniques approximate the unknown variables by utilizing simple functions. Substituting these approximations into the governing equations and subsequent mathematical manipulations result in a set of algebraic equations that are then solved to obtain the distribution of the properties at nodal points using suitable matrix solution techniques. The main differences between these methods are associated with the way in which flow variables are approximated and with the discretization processes.

Finite Difference Method. The conservation laws of fluid motion may be expressed mathematically in either differential or integral form. When a numerical scheme is applied to the differential equation, the domain of solution is divided into discrete points, upon which the finite difference equations are solved. Finite difference methods describe the unknowns of the problem by means of point samples at the node points of a grid of coordinate lines. The primary numerical approximation utilized in finite difference method is to represent the differential forms of the governing equations by difference

equations. Truncated Taylor series expansions are often used to generate the finite difference approximations of derivatives of the variables in terms of the variables at each grid point and its immediate neighbors. Those derivatives appearing in the governing equations are replaced by finite differences, resulting an algebraic equation for the values of the variables at each grid point. Since finite differencing is a pointwise approximation, the values computed at each point are assumed to be representative of the surrounding cell.

Finite Volume Method. When the integral form of an equation is utilized, the domain of solution is divided into small volumes (or areas for a two-dimensional case) and the conservation laws in integral form are applied to these volumes. The integral methods include finite volume and finite element methods. The finite volume method was originally developed as a special formulation of the finite difference method. In the finite volume method, the problem domain is divided up into control volumes. This method is distinguished by solving the integral forms of the governing equations (Equations 3-5) over each of the control volumes to yield a discretized equation at the center of each volume. The resulting statements express the exact conservation of relevant properties for each finite size cell. The conservation of each variable within a finite control volume is a balance between processes tending to increase or decrease it. Discretization involves the substitution of a variety of finite difference type approximations for the terms in the integrated equation representing flow processes such as convection, diffusion, and sources. This converts the integral equations into a system of algebraic equations [65]. A special benefit of the finite volume method is that it can be used directly on an irregular, non-structured grid without having to map to a computational domain.

Finite Element Method. Finite element techniques treat the computational space as many small, interconnected elements rather than a pointwise discretization of the continuum as in the finite difference methods. In this way, a piecewise approximation of the differential equations is made. Thus finite difference techniques are an approximate solution of the exact problem, whereas finite element methods provide the exact solution to an approximate problem. There is no basic mathematical difference between the two techniques. The only differences are in the implementation. In the past there have been more pros and cons for both finite differencing and finite elements. However, progress in both fields has closed the differences between them, and both tend to be equally suitable.

Spatial Discretization

Since these solution methods require the discretization of the problem domain, it is appropriate to discuss methods to relate the computational grid to the physical space. Numeric solution of the conservation laws, equation of state, and constitutive model first requires that the simulated geometry be described using a computational grid. Data is then computed at each grid point [40].

Lagrangian Method. A common technique attaches the computational grid point to the material, and the grid moves with the material as it deforms, deforming the mesh as well. This is known as the Lagrangian description, and is depicted in Figure 11. As the material deforms, grid points may move further apart or closer together, changing the cell volumes as the grid points follow the particle paths of points in the material.

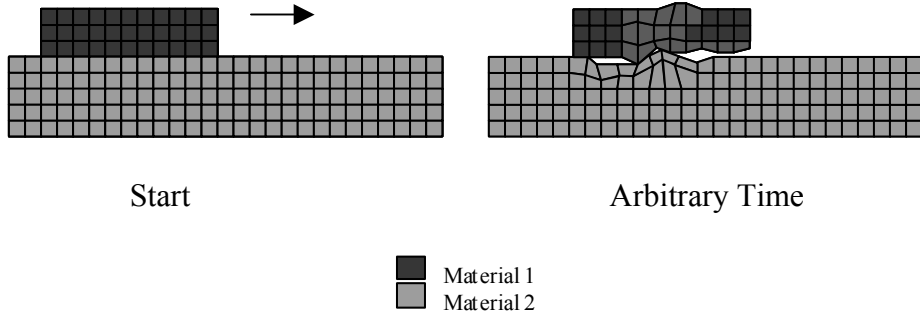


Figure 11. Slider and Guider Represented in Lagrangian Coordinates

The primary advantage of Lagrangian codes is their ability to accurately track material boundaries and interfaces. Since the grid is attached to the material, the material remains within the computational elements as they continuously deform with the distortion of the entire structure. Another advantage of the Lagrangian formulation is that due to its long history of structural applications, sophisticated material modeling is available, including the capability of modeling nonlinear material response (elastic-plastic, viscoplastic) in addition to the equation of state.

However, difficulties arise in the Lagrangian model when cells undergo large physical distortions, as will be the case in a high velocity slider/rail impact. Elements may become so distorted as to compromise the numerical accuracy of the contact simulation. Cells may be inverted, that is, the cell boundaries may cross one another, resulting in a computed negative mass. If cells shrink, the time step must become extremely small to satisfy the CFL stability condition (described later). If cells grow larger, the accuracy of calculations in the distorted areas may degrade as the defined grid becomes incapable of modeling a resulting complex geometry.

Eulerian Method. Problems inherent to the Lagrangian method are overcome through the use of the Eulerian technique, where the grid is fixed in space, and the material flows through the grid as shown in Figure 12. Eulerian codes are ideally suited for treating large distortions because the mesh is fixed. The quantities of flow into and out of a cell are used to compute the new mass, pressure, velocity, and energy. The cell volumes do not change. All hydrodynamic problems could be solved numerically using Eulerian calculation [40]. Use of the Eulerian method also enables the application of calculations for the diffusion and mixing of materials, which are not possible in Lagrangian coordinates.

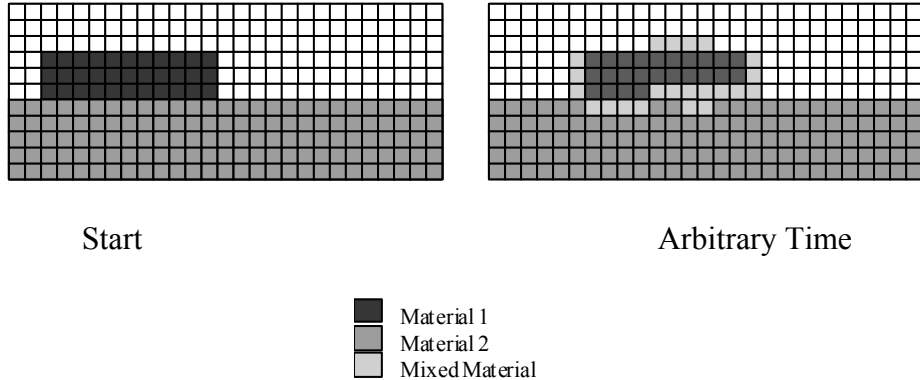


Figure 12. Slider and Guider Represented in Eulerian Coordinates

However the Eulerian method is not without its own difficulties. Material boundaries may move such that more than one material may be contained within the same computational cell, resulting in mixed material cells as seen in Figure 12. Material boundaries within a mixed material cell are not well defined and the exact position of material boundaries becomes difficult to determine. Typically, boundaries are only

known to the resolution of the Eulerian cell size. This may cause the materials to diffuse across cells at an unrealistic rate, and in general Eulerian codes are too diffusive to have sophisticated constitutive models. The numerical approximation of the differential equations in these mixed cell boundaries are not as accurate as the interior single material cells. Using a smaller mesh size may refine boundary accuracy, but this would result in longer computational run times. Additionally, within the mixed cells, the mixed materials are often assumed to be in pressure equilibrium (i.e. there is only one pressure per cell). Determination of the cell pressure requires an iterative procedure between the equations of states of the materials. This also results in increasing computational times for an increasing number of mixed cells.

As can be seen by comparing Figure 11 with Figure 12, more cells are required in the Eulerian computational grid to get the same accuracy as a Lagrangian grid because grid points are required everywhere in the computational space, not just over the materials.

The Eulerian method also does not track the material history such as in the Lagrangian method. Material history must be recorded by introducing additional variables such as Lagrangian tracers designed for this purpose, again increasing the computational burden.

Arbitrary Lagrangian Eulerian (ALE) Method. Since the phenomena of gouging involves large displacements, material mixing, material interface tracking, and non-linear material response it is clear that while both methods would provide benefits, each method also has some drawbacks. In order to gain the benefits of both Lagrangian and Eulerian methods, and to avoid the disadvantages associated with each method, a means of

coupling the two techniques has been developed called the Arbitrary Lagrangian Eulerian (ALE) Method.

In the ALE method, two steps are performed during each time increment. First, a Lagrangian step is performed where the motion of the fluid-structure material is determined by solving the conservation equations. In this step, the grid is deformed with the material, just as in the Lagrangian method. Second, a Eulerian rezoning step occurs where the now distorted mesh is partially restored to its original shape based on a predefined criteria for the element deformation. Mass, momentum, and energy are fluxed across the distorted element boundaries to calculate their new values for the restored element shape. An example of how the mesh could move is shown in Figure 13. In this figure, some of the cells boundaries have been relocated to less distorted states, while the material has remained in place. This allows the ALE method to maintain a balance for the physical relative velocity between motion of the grid and motion of the material.

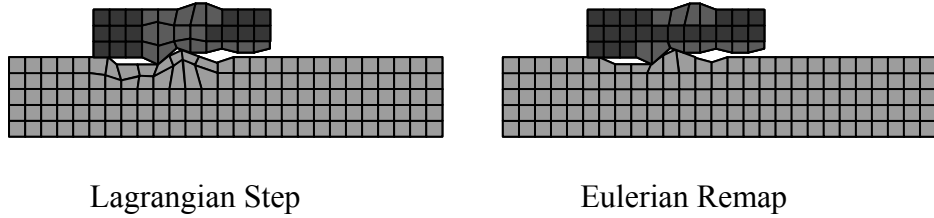


Figure 13. ALE Method

The mesh used in ALE moves with respect to a fixed reference frame, but the mesh is not fixed to the material, so it is called arbitrary. This allows the mesh to move somewhat with the material, and allows the material to move somewhat through the

mesh. The potential advantage from ALE is that it allows one to treat a material in either a Lagrangian mode or one in which the material is allowed to move relative to the mesh. Different materials within the computational mesh can then be treated in the most appropriate manner [66,67].

The method implemented in CTH is very similar to the ALE method. The rezoning step maps the grid to its original geometry, so at the end of the step there is no change to the grid. The end result is that CTH is considered an Eulerian code, although there is a Lagrangian calculation at every time step.

Smooth Particle Hydrodynamics (SPH) Method. Another alternate method designed to overcome the individual drawbacks of the Lagrangian and Eulerian methods as discussed previously is the Smooth Particle Hydrodynamics (SPH) method. SPH is a method of continuum mechanics analysis in which materials are modeled by a discrete set of particles. In SPH the conservation equations are applied at discrete particles in the computational domain. These particles are not associated with a traditional grid system and are not constrained by connectivity requirements like finite elements making SPH ideally suited to simulate large deformation. Application of SPH requires the specification of a weight function that describes a domain of influence that any particle can have with its neighboring particles [68].

Consistency, Accuracy, Stability, and Efficiency

To discretize the differential equations, several properties of the representative differencing approximations need to be analyzed. These include consistency, accuracy, stability, and efficiency [40].

Consistency refers to the idea that the difference equation actually represents its respective differential equation. It is required that the difference scheme reduces to the differential equation in the limit as the time and spatial steps go to zero.

Accuracy of the difference scheme is influenced by round off and truncation errors. Round off errors are due to the limit of significant digits that are carried by the computer. Truncation errors result from the actual discretization, which is only an approximation of the continuum equations [69].

Stability reflects whether the solution will converge or become unbounded. Instability is produced when errors are magnified from one step to the next. The Courant-Friedrichs-Lowy (CFL) stability condition requires that $\Delta t \leq \frac{\Delta x}{c}$ where c is the wave speed [70]. Essentially, the enforcement of this condition would prohibit any disturbances from propagating across more than one cell in a single time step.

The last requirement for a numerical technique is efficiency, which may be defined as the ratio of the total number of calculation and communication (i.e. with memory, between processors) steps required by a computer to obtain a solution to the unit time length of the problem. More complex differencing schemes tend to be more accurate but less efficient. Efficiency is required because of constraints on computational memory and speed. Thus a compromise between accuracy and efficiency is typically required.

Treatment of Shocks

Calculation of problems involving discontinuities, particularly shock waves, presents a special problem because these phenomena occur within a cell boundary rather than being smoothly distributed across cells. Other than implementing the Rankine-Hugoniot jump

conditions, the use of artificial viscosity has been introduced. The addition of an artificial viscosity term to the momentum equation introduces a dissipative mechanism that spreads shocks smoothly over several cells. It is also used to model irreversible effects associated with shocks and to prevent oscillations behind a shock. This method does however affect the stability of a problem, and the CFL condition must be modified accordingly.

Example of Finite Volume Solution Methodology

Now that the basic issues of numerical methodology have been discussed, an example of how the finite volume method can be implemented is described as a prelude to a discussion on the methods within the hydrocode CTH. This example develops the solution for the two-dimensional heat conduction equation based on a textbook by Hoffman and Chiang [71].

Grid generation is the first step in the solution. A domain to be considered is broken up into a uniform square mesh. Figure 14 shows an arbitrary portion of the resulting mesh.

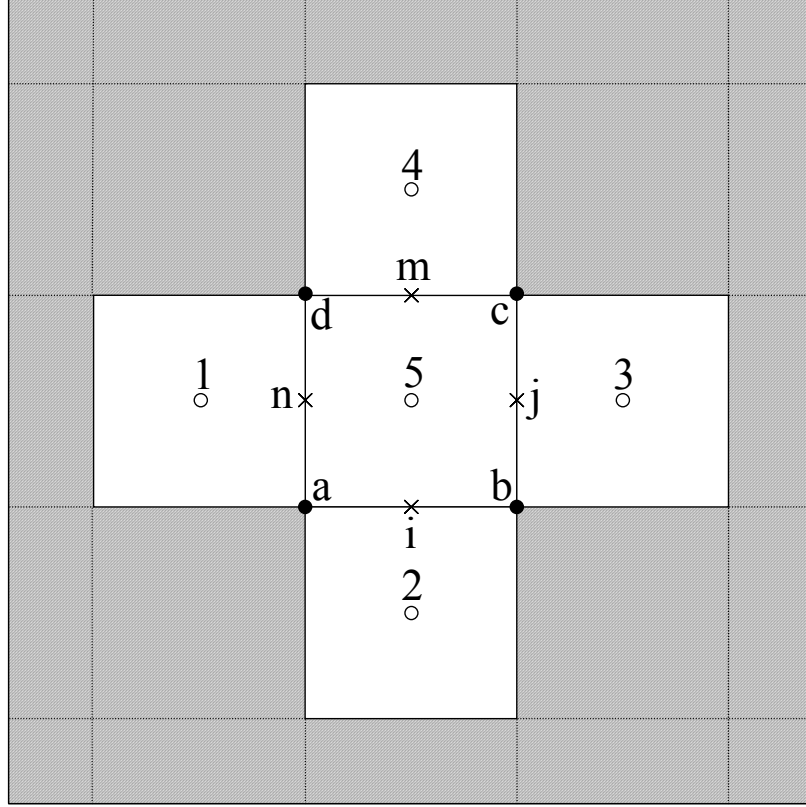


Figure 14. Sample Computational Grid

Of interest here will be the solution of the heat equation for the cell $abcd$ with center point 5. More generally, the center point 5 of the cell being considered could be called point (i,j) , and then the points a, b, c , and d would be $(i-\frac{1}{2},j-\frac{1}{2})$, $(i+\frac{1}{2},j-\frac{1}{2})$, $(i+\frac{1}{2},j+\frac{1}{2})$ and $(i-\frac{1}{2},j+\frac{1}{2})$ respectively. The letters and number are used to simplify notation.

The two-dimensional heat conduction equation is given by:

$$\frac{\partial u}{\partial t} = \alpha \left(\frac{\partial^2 u}{\partial x^2} + \frac{\partial^2 u}{\partial y^2} \right) \quad t > 0 \quad (25)$$

Integration of this equation over the cell $abcd$ results in:

$$\int_{abcd} \left(\frac{\partial u}{\partial t} \right) dx dy = \alpha \int_{abcd} \left(\frac{\partial^2 u}{\partial x^2} + \frac{\partial^2 u}{\partial y^2} \right) dx dy \quad (26)$$

Now considering each side of this equality individually, the left hand side can be approximated by:

$$\int_{abcd} \left(\frac{\partial u}{\partial t} \right) dx dy = \left(\frac{u_5^{n+1} - u_5^n}{\Delta t} \right) A_{abcd} \quad (27)$$

where A_{abcd} is the area of the cell. Points 1, 2, 3, 4, and 5 are called the control points of the five cells, and are the locations that data are solved for in cell-centered schemes.

Again, these points could more generally be considered as $(i-1, j)$, $(i, j-1)$, $(i+1, j)$, $(i, j+1)$, and (i, j) , respectively, but the numbers are used to simplify notation.

Moving on to the right hand side of Equation 26, let $F = \frac{\partial u}{\partial x}$ and $G = \frac{\partial u}{\partial y}$. Then:

$$a \int_{abcd} \left(\frac{\partial^2 u}{\partial x^2} + \frac{\partial^2 u}{\partial y^2} \right) dx dy = a \int_{abcd} \left(\frac{\partial F}{\partial x} + \frac{\partial G}{\partial y} \right) dx dy = a \oint_{abcd} (F dy - G dx) \quad (28)$$

where Green's Theorem, which converts area integrals into line integrals, has been applied in the last step. Using the square $abcd$, one may approximate the integral as:

$$\oint_{abcd} (F dy - G dx) = \left[\begin{aligned} & (F_i \Delta y_{ab} + F_j \Delta y_{bc} + F_m \Delta y_{cd} + F_n \Delta y_{da}) \\ & + (G_i \Delta x_{ab} + G_j \Delta x_{bc} + G_m \Delta x_{cd} + G_n \Delta x_{da}) \end{aligned} \right] \quad (29)$$

where the points i, j, m , and n represent the midpoint locations of the edges ab, bc, cd , and da , respectively. The x and y increments of each edge are determined by:

$$\Delta x_{ab} = x_b - x_a \quad \Delta x_{bc} = x_c - x_b \quad \Delta x_{cd} = x_d - x_c \quad \Delta x_{da} = x_a - x_d$$

$$\Delta y_{ab} = y_b - y_a \quad \Delta y_{bc} = y_c - y_b \quad \Delta y_{cd} = y_d - y_c \quad \Delta y_{da} = y_a - y_d$$

In this example, if the control point values used are from time n , then this will be an explicit problem. If the values used are for $n+1$, then we will have an implicit problem, which will require the simultaneous solution of all cells.

For an explicit formulation, combining the left and right hand sides together we find that the unknown u_5 is determined from:

$$u_5^{n+1} = u_5^n + \alpha \frac{\Delta t}{A_{abcd}} \left[\begin{aligned} & \left(F_i \Delta y_{ab} + F_j \Delta y_{bc} + F_m \Delta y_{cd} + F_n \Delta y_{da} \right) \\ & + \left(G_i \Delta x_{ab} + G_j \Delta x_{bc} + G_m \Delta x_{cd} + G_n \Delta x_{da} \right) \end{aligned} \right] \quad (30)$$

Now the functions F and G at the midpoints i, j, m , and n of the edges are evaluated by:

$$F_i = \left(\frac{\partial u}{\partial x} \right)_i = \frac{1}{A_{a2b5}} \int_{a2b5} \left(\frac{\partial u}{\partial x} \right) dx dy = \frac{1}{2A_{a2b5}} \left[\begin{aligned} & (u_a^n + u_2^n) \Delta y_{a2} + (u_2^n + u_b^n) \Delta y_{2b} \\ & + (u_b^n + u_5^n) \Delta y_{b5} + (u_5^n + u_a^n) \Delta y_{5a} \end{aligned} \right] \quad (31)$$

and similarly:

$$F_j = \frac{1}{2A_{5b3c}} \left[(u_5^n + u_b^n) \Delta y_{5b} + (u_b^n + u_3^n) \Delta y_{b3} + (u_3^n + u_c^n) \Delta y_{3c} + (u_c^n + u_5^n) \Delta y_{c5} \right] \quad (32)$$

$$F_m = \frac{1}{2A_{d5c4}} \left[(u_d^n + u_5^n) \Delta y_{d5} + (u_5^n + u_c^n) \Delta y_{5c} + (u_c^n + u_4^n) \Delta y_{c4} + (u_4^n + u_d^n) \Delta y_{4d} \right] \quad (33)$$

$$F_n = \frac{1}{2A_{1a5d}} \left[(u_1^n + u_a^n) \Delta y_{1a} + (u_a^n + u_5^n) \Delta y_{a5} + (u_5^n + u_d^n) \Delta y_{5d} + (u_d^n + u_1^n) \Delta y_{d1} \right] \quad (34)$$

and also:

$$G_i = \frac{1}{2A_{a2b5}} \left[(u_a^n + u_2^n) \Delta x_{a2} + (u_2^n + u_b^n) \Delta x_{2b} + (u_b^n + u_5^n) \Delta x_{b5} + (u_5^n + u_a^n) \Delta x_{5a} \right] \quad (35)$$

$$G_j = \frac{1}{2A_{5b3c}} \left[(u_5^n + u_b^n) \Delta x_{5b} + (u_b^n + u_3^n) \Delta x_{b3} + (u_3^n + u_c^n) \Delta x_{3c} + (u_c^n + u_5^n) \Delta x_{c5} \right] \quad (36)$$

$$G_m = \frac{1}{2A_{d5c4}} \left[(u_d^n + u_5^n) \Delta x_{d5} + (u_5^n + u_c^n) \Delta x_{5c} + (u_c^n + u_4^n) \Delta x_{c4} + (u_4^n + u_d^n) \Delta x_{4d} \right] \quad (37)$$

$$G_n = \frac{1}{2A_{1a5d}} \left[(u_1^n + u_a^n) \Delta x_{1a} + (u_a^n + u_5^n) \Delta x_{a5} + (u_5^n + u_d^n) \Delta x_{5d} + (u_d^n + u_1^n) \Delta x_{d1} \right] \quad (38)$$

where $\Delta x_{pq} = x_q - x_p$ and $\Delta y_{pq} = y_q - y_p$. Substituting Equations 31-38 into Equation 30, the solution is:

$$u_5^{n+1} = u_5^n + \alpha \frac{\Delta t}{A_{abcd}} \left\{ \begin{aligned} & \left[\frac{1}{2A_{a2b5}} [(u_a^n + u_2^n) \Delta y_{a2} + (u_2^n + u_b^n) \Delta y_{2b} + (u_b^n + u_5^n) \Delta y_{b5} + (u_5^n + u_a^n) \Delta y_{5a}] \Delta y_{ab} \right. \\ & + \frac{1}{2A_{5b3c}} [(u_5^n + u_b^n) \Delta y_{5b} + (u_b^n + u_3^n) \Delta y_{b3} + (u_3^n + u_c^n) \Delta y_{3c} + (u_c^n + u_5^n) \Delta y_{c5}] \Delta y_{bc} \\ & + \frac{1}{2A_{d5c4}} [(u_d^n + u_5^n) \Delta y_{d5} + (u_5^n + u_c^n) \Delta y_{5c} + (u_c^n + u_4^n) \Delta y_{c4} + (u_4^n + u_d^n) \Delta y_{4d}] \Delta y_{cd} \\ & \left. + \frac{1}{2A_{1a5d}} [(u_1^n + u_a^n) \Delta y_{1a} + (u_a^n + u_5^n) \Delta y_{a5} + (u_5^n + u_d^n) \Delta y_{5d} + (u_d^n + u_1^n) \Delta y_{d1}] \Delta y_{da} \right] \\ & + \left[\frac{1}{2A_{a2b5}} [(u_a^n + u_2^n) \Delta x_{a2} + (u_2^n + u_b^n) \Delta x_{2b} + (u_b^n + u_5^n) \Delta x_{b5} + (u_5^n + u_a^n) \Delta x_{5a}] \Delta x_{ab} \right. \\ & + \frac{1}{2A_{5b3c}} [(u_5^n + u_b^n) \Delta x_{5b} + (u_b^n + u_3^n) \Delta x_{b3} + (u_3^n + u_c^n) \Delta x_{3c} + (u_c^n + u_5^n) \Delta x_{c5}] \Delta x_{bc} \\ & + \frac{1}{2A_{d5c4}} [(u_d^n + u_5^n) \Delta x_{d5} + (u_5^n + u_c^n) \Delta x_{5c} + (u_c^n + u_4^n) \Delta x_{c4} + (u_4^n + u_d^n) \Delta x_{4d}] \Delta x_{cd} \\ & \left. + \frac{1}{2A_{1a5d}} [(u_1^n + u_a^n) \Delta x_{1a} + (u_a^n + u_5^n) \Delta x_{a5} + (u_5^n + u_d^n) \Delta x_{5d} + (u_d^n + u_1^n) \Delta x_{d1}] \Delta x_{da} \right] \end{aligned} \right\} \quad (39)$$

Now let $\overline{ab} = l$ and consider that the mesh in Figure 14 is a square mesh. Then we have the following series of simplifying relations:

$$\overline{ab} = \overline{bc} = \overline{cd} = \overline{da} = l$$

$$A_{abcd} = l^2$$

$$\Delta x_{ab} = l$$

$$\Delta x_{cd} = -l$$

$$\Delta x_{bc} = \Delta x_{da} = 0$$

$$\Delta y_{bc} = l$$

$$\Delta y_{da} = -l$$

$$\Delta y_{ab} = \Delta x_{cd} = 0$$

$$A_{a2b5} = A_{5b3c} = A_{d5c4} = A_{1a5d} = \frac{1}{2}l^2$$

$$\Delta x_{a2} = \Delta x_{2b} = \Delta x_{5b} = \Delta x_{b3} = \Delta x_{d5} = \Delta x_{5c} = \Delta x_{1a} = \Delta x_{a5} = \frac{1}{2}l$$

$$\Delta x_{b5} = \Delta x_{5a} = \Delta x_{3c} = \Delta x_{c5} = \Delta x_{c4} = \Delta x_{4d} = \Delta x_{5d} = \Delta x_{d1} = -\frac{1}{2}l$$

$$\Delta y_{a2} = \Delta y_{5a} = \Delta y_{5b} = \Delta y_{c5} = \Delta y_{d5} = \Delta y_{4d} = \Delta y_{1a} = \Delta y_{d1} = -\frac{1}{2}l$$

$$\Delta y_{2b} = \Delta y_{b5} = \Delta y_{b3} = \Delta y_{3c} = \Delta y_{5c} = \Delta y_{c4} = \Delta y_{a5} = \Delta y_{5d} = \frac{1}{2}l$$

Substituting all of this into Equation 39, the solution reduces to:

$$u_5^{n+1} = u_5^n + \alpha \frac{\Delta t}{l^2} \left[(u_1^n - 2u_5^n + u_3^n) + (u_2^n - 2u_5^n + u_4^n) \right] \quad (40)$$

or more generally:

$$u_{i,j}^{n+1} = u_{i,j}^n + \alpha \frac{\Delta t}{l^2} \left[(u_{i-1,j}^n - 2u_{i,j}^n + u_{i+1,j}^n) + (u_{i,j-1}^n - 2u_{i,j}^n + u_{i,j+1}^n) \right] \quad (41)$$

From here, the solution can be integrated through by time steps, considering any necessary stability conditions. If $abcd$ is rectangular, as in this case, then the finite volume solution is equivalent to a finite difference formulation where central difference approximation of the spatial derivatives are used.

CTH Solution Sequence

In CTH, the equations governing the conservation of mass, momentum, and energy (Equations 3, 4, and 5) are integrated explicitly in time using a two-step Eulerian scheme consisting of a Lagrangian step and a remap step.

The Lagrangian step solves the finite volume approximations to the conservation equations by integrating across a time step. Although the explicit equations are solvable, the time step must be controlled to prevent information from crossing more than one cell during a single time step. The time step is chosen to be the minimum of the CFL condition for stability and a cell-volume-change limiting function that prevents excessive compression or expansion of a cell. Some finite difference approximations are used to determine certain quantities such as velocity gradients. These two schemes are equivalent in accuracy (2nd order accurate) if a square mesh is used with a uniform cell size.

With the exception of positions and velocities, all quantities or parameters are centered in each cell and are assumed to be uniform across the cell. The components of the cell velocity vector are centered on, and perpendicular to, a cell face. Variable positioning for a two-dimensional, rectangular cell is shown in Figure 15.

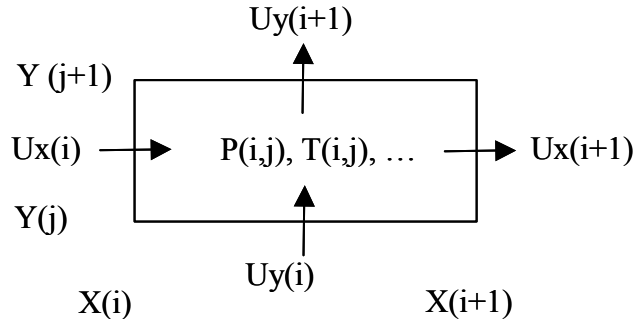


Figure 15. CTH Eulerian Cell [54]

During the Lagrangian step, the computational cells distort to follow the material motion and there is no mass flux across the cell boundaries. Thus, mass is conserved

trivially. The remaining conservation equations are replaced with explicit finite volume representations of the original integral equations.

Given current values of cell masses, volumes, and stresses, the momentum equation is integrated to find updated cell velocities. The finite volume approximation for the x component of the momentum balance equation is

$$Ux_{n+\frac{1}{2},i-\frac{1}{2},j,k} = Ux_{n-\frac{1}{2},i-\frac{1}{2},j,k} - \frac{\delta t_n Ax_{i-\frac{1}{2},j,k}}{\mu_{i-\frac{1}{2}} M_{n,i,j,k}} \Delta_{i-\frac{1}{2}} (P_{n,i,j,k} + Qxx_{n,i,j,k}) + \frac{\delta t_n \mu_{i-\frac{1}{2}} (M_{n,i,j,k} Bx_{n,i,j,k})}{\mu_{i-\frac{1}{2}} M_{n,i,j,k}} \quad (42)$$

where n , i , j , and k are the time and spatial indices, Ux , Ax , and Bx are the velocity, area of the cell face, and the body force in the x direction, respectively, δt_n is the n^{th} time step, M is the cell mass, P is the cell pressure, Qxx is the xx component of the artificial viscosity tensor, and μ and Δ are average and difference operations on the proceeding terms. An analogous equation holds for the conservation of momentum equations in the y and z directions.

The energy equation is integrated over the same time step by means of another staggered mesh finite volume approximation. The conservation of energy equation is written as a balance equation for the internal energy. The total energy in the cell is composed of both internal and kinetic energy. The finite volume approximation to Equation 5 will not conserve total energy unless a special form is used for the total energy in a cell and a special form is used for the mechanical work. In one dimension,

$$M_{n,i} \Delta_{\frac{i-1}{2}} E_{n,i} + \frac{\mu_{\frac{i-1}{2}} M_{n,i}}{2} \Delta_n \left(Ux^2 \right) = \delta t_{\frac{n+1}{2}} M_{n,i} S_{\frac{n+1}{2},i} + \delta t_n \mu_n Ux_{\frac{n-1}{2},i-1} \mu_{\frac{i-1}{2}} (M_{n,i} B_{n,i}) \\ + \delta t_n Ax_{\frac{n-1}{2}} \mu_n Ux_{\frac{n-1}{2},i-1} (P_{n,i-1} + Qxx_{n,i-1}) - \delta t_n Ax_{\frac{n+1}{2}} \mu_n Ux_{\frac{n-1}{2},i+1} (P_n + Qxx_{n,i}) \quad (43)$$

where E is the cell specific internal energy and S is the cell energy source. This methodology can extend directly to multiple dimensions. The solution of this equation requires values of the velocities determined from the momentum equation solution, in addition to mechanical work discretization. Contributions to the mechanical work term come from volumetric (pressure), deviatoric, and artificial viscosity terms [53].

Mechanical work results in an internal energy source associated with the computational cell. The algorithm for partitioning the energy among the materials is part of a cell thermodynamics model. The mechanical work associated with the pressure and artificial viscosity is partitioned between the materials. Mechanical work associated with the stress deviators is partitioned between the materials that can support shear, and is proportional to the volume fractions of the materials. CTH adds the strain energy associated with a material's deviatoric response to that material's internal energy (which also includes the contribution from its isotropic response). The internal energy is used by the equation of state model employed for that material to calculate a temperature.

Stress deviators are updated after these integrations by using the new values of cell velocities, with the second invariant of the deviatoric stress limited by any selected constitutive models. The solution of the energy equation is used to update the cell thermodynamic data: pressure, density, and temperature. Because of the pressure term, completing the description of the full stress tensor in CTH is a matter of thermodynamic updating. This process is not completed until the remap step is completed. When the

thermodynamic updating and remapping are completed, the calculations are advanced to the next cycle and evolution of the problem continues. All of the models discussed previously such as the constitutive and fracture models and artificial viscosity are applied during the Lagrangian step.

After the Lagrangian step, the remap step is performed. During this step, the distorted cells are remapped back to the initial fixed mesh. The velocities, energies, stress deviators, and any internal state variables must be remapped. The remap step advects the appropriate mass, momentum, and energy from the deformed mesh of the Lagrangian step back to the original mesh. Operator splitting techniques are used to perform the multi-dimensional remap operation. The resulting one-dimensional convection equations use a second-order accurate conservative scheme developed by van Leer to calculate the fluxes between cells. The scheme used in CTH replaces a uniform distribution in the old cell with a linear distribution. To reduce the asymmetry resulting from the operator splitting, a permutation scheme in direction of the flow is applied [53].

The volume flux between the old and new cells is calculated first from the geometry of the cell-face motion. Once that is calculated, the volume of materials to be advected must be estimated using an interface tracking algorithm that estimates the location of material interfaces within mixed cells. Next, each material's mass and internal energy are moved using the information from the interface tracker. The three basic variables of mass, momentum, and kinetic energy are calculated from two data base quantities: mass and velocity. As a result, the three basic variables cannot all be conserved across the remap step. To account for the non-conservation of both the momentum and kinetic energy, the user can choose to have the momentum conserved and kinetic energy

discrepancies transformed in an internal energy source or sink, the kinetic energy conserved and the momentum not, or the momentum conserved and the kinetic energy discarded except if momentum fluxed into the new cell has the opposite sign as that cell, in which case the energy is deposited into internal energy. The third option is conceptually similar to an inelastic collision and generally gives the best results [53].

After all remap steps have been completed, the Eulerian energy balance is accomplished. The equation of state package is called for each material yielding new cell pressures, temperatures, and sound speeds. One of the last steps in the remap is to calculate the minimum time step, this is first done for each node and then a global minimum is done to determine the time step for the next computational cycle [54].

Boundary Conditions

The finite volume approximations solve conditions in each cell using the conditions of its surrounding cells. However, cells on the computational boundary do not have cells on at least one of their sides. Because this information is missing, additional information is enforced at these cells in the form of boundary conditions. These are typically in the form of holding flow variables at a known quantity or a known derivative.

In the current research, two types of boundary conditions are used. The first is used at the rail boundaries. In this case, a sound speed based absorbing boundary condition is used to model semi-infinite media. In this case, material velocity is fixed at the boundary. But pressure is allowed to pass through it, controlled in the x direction by:

$$\rho c \frac{d}{dt} Ux = \pm \frac{d}{dt} (P + Q) \quad (44)$$

where U_x is the velocity in the x direction, P is the cell pressure, and Q is the artificial viscosity. This equation allows the pressure and artificial viscosity to move out of the mesh at the speed of sound. An analogous equation is used in the y and z directions.

The second boundary condition, called an “outflow” condition in CTH, is used on the upper boundary. This adds an empty set of cells to the outer edge of the boundary and “fills” them with void, which has zero pressure. This results in zero pressure being enforced along this boundary. However, material is allowed to pass through this boundary, allowing the slipper to exit the computational domain after it passes by the area of interest.

Material Interfaces

The presence of material boundaries in an Eulerian grid requires special consideration to be given to how these boundaries will be treated. At the boundaries, cells may contain parts of multiple materials and/or void, which is space that does not contain material but is enforced to have zero pressure. The treatment of material boundaries is dealt with in two different manners in CTH: the treatment of mixed cells and the use of special sliding boundary algorithms.

CTH has several different options to handle multimaterial cells. In the first, the model defines the yield stress in a mixed material cell as the sum of the volume fraction weighted yield stresses of the individual materials. Single material cells with void have a decreased yield stress because the volume fraction of the material is less than one.

Another model is similar except that the yield stress of all cells is divided by the sum of the volume fractions of the materials that can support shear. Now single material cells with void have the yield stress of the material.

The last model sets the cell yield stress to zero in mixed cells except for the case of a cell containing one material plus void. In this case a volume-weighted average is used, as in the first model. This allows the materials to move as separate, unattached entities, but also results in the impact being frictionless. This model is generally the preferred option when modeling frictionless interfaces when the boundary layer algorithm is not used.

The other method to handle material interfaces is through sliding interface algorithms. Without an interface sliding algorithm specified, CTH assumes that when two materials are in contact, they have the same velocity. This results in the slipper and rail being joined together as one object. In this case, interface behavior is dictated by how multi-material cells are treated. However, in many cases including the simulation of rail gouging, it is known that the two materials involved are separate and will have a large relative displacement between them. For such cases, two specially developed interface models in CTH are the Slide Line and Boundary Layer Interface models. These special models allow for the simulation of sliding interfaces by allowing the materials at an interface to retain their strength properties, yet move independently. The slide line routine, for example, allows materials along designated interfaces to keep their strength in compression and tension, but sets the shear strength to zero to allow the materials to slide. Behavior can be computed at material interfaces using a Lagrangian calculation by providing spatial slidelines, which are used when large transverse deflections of the material interface are expected [40]. The Boundary Layer Interface model couples the

deformation of materials where they share an interface. One surface is deformed using the forces on both materials, and the adjoining surface is transversely constrained to move with it, although the materials may maintain distinct tangential velocities.

Mechanical Loading and Aerodynamic Analysis

The slipper loads can be broken into two categories: quasi-static loads and dynamic loads. Quasi-static loads include inertial forces, rocket thrust, braking, aerodynamic forces, force couples from moments about the center of gravity, and of the reactions of these forces and moments at the slipper rail interfaces [3]. Quasi-steady state loading includes aerodynamic lift and drag, symmetrical thrust, unsymmetrical thrust, braking and inertia forces, weight, rail curvature, and cross track wind. The resulting bearing pressure on the slipper surface is simply the quasi-static force divided by the surface area of the slipper.

Although many factors are influential on the slipper load, the gouging mechanism is most likely dependent on the value of the load, regardless of the cause. In this research, the load is simulated by using an initial vertical impact velocity. The range of loads and vertical velocities to be studied is based on experimental results and analytical predictions from Holloman AFB.

Dynamic loads have not been traditionally used in slipper wear and heating calculations, but are important factors in determining mechanical and thermal conditions on the slipper and rail which lead to gouging. Internal aerodynamic lift is comprised of loads generated by the air pressure in the slipper/rail gap. The lift due to the flow through the gap increases with sled speed and constitutes the dominating load at hypersonic

speeds if not properly controlled with airflow deflection devices or bleed mechanisms. While external aerodynamic loads may be theoretically derived and investigated using a wind tunnel [72-74], the complex geometry of the sled and the discrepancy between the actual hypersonic sled environment and the models result in calculated loads that may be inaccurate [2,3]. However, experimental measurements of pressure in the slipper gap at hypersonic velocities are also difficult to obtain, indicating the need for hypersonic aerodynamic analysis.

The aerodynamic loads and irregularities in the rail, aggravated by the unstable airflow through the slipper/rail gap, impart vertical motion. The dynamic forces due to the oscillatory vertical motion, and the resulting high-speed sled-rail interaction are the dominating forces for the structural design of the sled [75]. These loads are an order of magnitude greater than the quasi-static loads. The frequency of these impacts has been found to be a direct function of the sled velocity. Testing has shown that controlled aerodynamic downloading using fixed canards or a sloped nose can significantly reduce these forces [9].

Thermal Effects

Even though temperatures at the sliding interfaces between the slipper and rail are considerably higher than room temperature, only room temperature has been considered in previous studies concerning material properties and computational simulations. No consideration has been given to the effects of elevated temperatures. Estimated temperatures can be used to determine if gouge initiation and development mechanisms are affected. Elevated temperature solutions may also serve as the basis for further study

of the interactive effect of slider and guider materials and be used to determine if there exists a relationship between slider properties, gouging onset velocity, and guider properties. For example, while Mixon [11] attributed the observation that the number of gouges per 100 ft is significantly higher after peak velocity then before due to slider deterioration, this could also be partly the result of elevated temperature.

In the slider assembly, there are three main sources of heat: the aerodynamic heating from the flow around the slider and through the slider gap, frictional contact between the slider and rail, and chemical reaction of the sled components.

Aerodynamic Heating. The aerodynamic model of the slider/rail gap used by Korkegi and Briggs [29,30] consisted of a laminar stagnation region at the leading edge of the slider followed by a separate turbulent boundary layer on the slider and rail merging into a Couette flow asymptote. The researchers concluded that the airflow through the gap is shock-compressed to high pressures and temperatures resulting in high lift loads and high heat rates to the inner surface of the slider. They estimated the heat rates and pressure distributions along the gap from Mach 4 to Mach 10 and found that heat rates on the inner surface of the slider are of the same order as that encountered at the stagnation point of the leading edge on reentry vehicles, a magnitude of about 10^4 Btu/ft²-sec.

At the leading edge of bodies in aerodynamic flow, a point where the air flow changes velocity to match that of the body is known as a stagnation point. At these points, the air temperature can increase drastically. An example of an 8000 ft/s sled test profile is shown in Figure 16 depicting sled velocity versus track location and time. The figure also plots the corresponding adiabatic stagnation temperature for the corresponding

velocity and atmospheric environment. Aerodynamic heating for speeds above Mach 4.5 is strong enough to require heat protective coatings to protect sled components [9].

Figure 17 shows an example of shock waves produced by the hypersonic sled, and the high temperature stagnation points at component leading edges appear white due to heating.

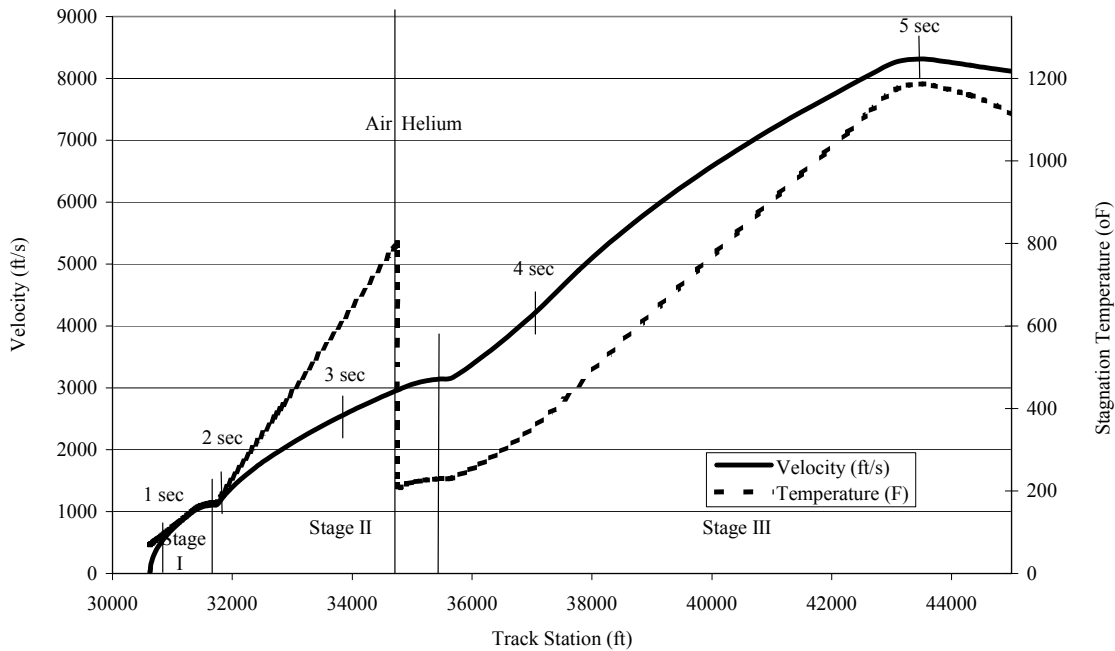


Figure 16. Sled Test Velocity Profile [77]

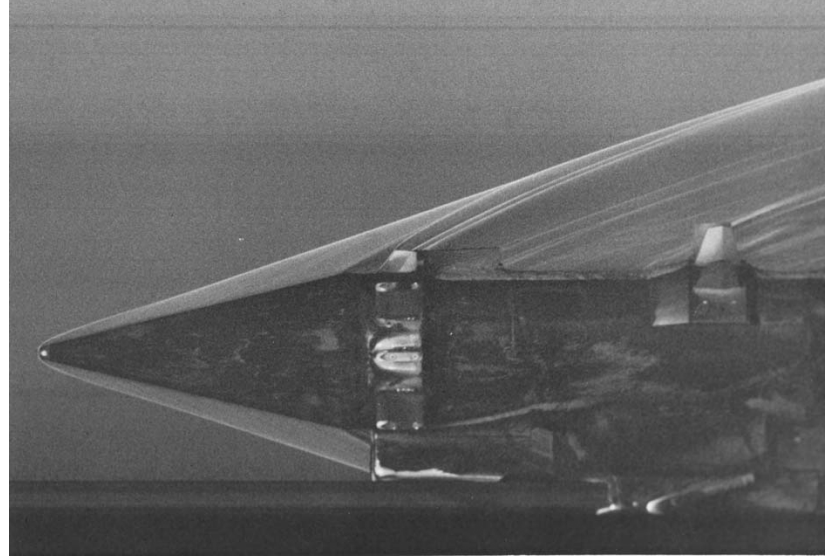


Figure 17. Shock wave and Aerodynamic Heating of Sled [4]

Since the rail is within three feet of the ground, flow around a dual-rail sled may be trapped between the sled and a trough [76]. Also, due to the complex geometry preceding the slipper gap, the slipper is subject to reflected and interacting shock waves that may result in severe thermal and structural loads.

Frictional Heating. An investigation of the frictional heating by Krupovage and Rassmussen [9] related frictional heating to the energy developed by friction between the slipper and rail. They found that the power developed by friction is directly proportional to the material friction coefficient, bearing pressure, and relative velocity. The rate of energy produced by friction is the product of the frictional force and the sled velocity, where the frictional force may be written as the product of the normal force and coefficient of friction. This empirically determined friction has been shown to be a direct function of the sliding velocity [9]. Thus the frictional heating can be expressed as

$$\dot{w} = C_f N v \quad (1)$$

where \dot{w} is the rate of work (or energy) developed by the sliding friction, N is the normal force, v is the relative velocity, and C_f is the coefficient of friction.

Using a similar approach combined with data from an analysis tool known as Dynamic Analysis and Design System (DADS) [77] used at the test track, an estimate of the rise in temperature of the slipper due to friction can be determined. First, one may calculate the change in energy at the interface due to friction. The total change in energy in this case will be determined by the frictional force times the distance the slipper moves. The assumption is made that half of the energy will be converted into heat. So then the amount of energy imparted to the slipper is:

$$\Delta E_{\text{slipper}} = \frac{1}{2} \dot{w} = \frac{1}{2} Fd \quad (45)$$

Examining DADS data, the average frictional force of the final stage over the length of the run is 920 N. Using this force and a total run distance of 13,684 ft, the change in slipper energy would be 1.92 MJ.

To calculate the change in temperature, the energy change, mass, and specific heat of the slipper are related by:

$$\Delta T = \frac{\Delta E}{c_v m} = \frac{Fd}{2c_v m} \quad (46)$$

The largest contact area of the slipper is the upper surface, which is 10.16 cm wide by 20.32 inches long. If we assume that this entire surface area and 1.27 cm of steel above it for all four slippers absorb this energy, the mass used in the equation will be 8.39 kg. The reason 1.27 cm was chosen as the effective depth is because time dependent diffusion problems presented later in this chapter will show that 90% of the thermal

energy is contained well within this distance of the thermal source. The specific heat varies with temperature as in the following table:

Table 2. Specific heat of VascoMax 300 Steel [81]

Temperature (K)	Specific heat c_v (J/g·K)
298	0.360
422	0.481
598	0.599
700	0.858

Using an intermediate value of the specific heat of 0.42 J/g·K, the change in temperature is 546 K, bringing the slipper to 844 K (1060 °F). If it is considered, however, that only portions of the four slippers will be in contact, it is observed that changing the effected slipper mass has a linear effect on the change in temperature. At the test track, the contact surfaces tend to be at only small portions of the rail at any given time. If one assumes a total contact surface over the run is one quarter of the area suggested above, the change in temperature quadruples to 2184 K (3472 °F). This method also assumes that all of the heated mass is affected equally, where a more accurate model would consider energy diffusion through the mass and that the energy source is on one side of the material. Including this feature would certainly result in an even higher temperature near the surface.

Chemical Reactions. The temperatures reached due to thermal inputs are high enough to excite vibrational energy internally within the molecules, and to cause dissociation and

even ionization within the gas. Furthermore, if sled components are protected by an ablative heat shield, the byproducts of the ablation process are also present in the boundary layer. Hence the surface of the sled may be engulfed by a chemically reacting boundary layer and the entire shock layer can be dominated by chemically reacting flow. This gives rise to two additional factors that need to be considered in hypersonic analysis. First, that the vibrational energy of the molecules becomes excited causing the specific heats to become functions of temperature. Second, as the gas temperature increases, a chemical reaction can occur. Thus, the assumption of a perfect non-reacting gas for hypersonic flow will give unrealistically high values of temperature.

Chemical reactions are also caused by severe erosive oxidation of sled components. Once oxidation is initiated, the additional energy produced by the chemical reaction is usually sufficient to cause complete breakdown and erosion of the material within milliseconds [9], and the byproducts of such erosion are then also found in the boundary layer. These problems have been greatly alleviated through the use of the helium environment, but are still problematic in track sections or tests where helium is not used.

Many hydrocodes have some capabilities to handle high-energy burn conditions, and these may have applications to the reactive flow around the slipper. However, this scenario is not considered as part of this work.

Methods for Implementing Thermal Environment. To implement elevated temperature models into CTH calculations, three methods of increasing complexity are determined. For each of these methods, it is assumed that during the gouging event itself, the heating rate from friction or aerodynamics is negligible. This assumption is used because gouging initiates and develops in a matter of microseconds, a much smaller time

scale than the diffusion rate of the materials involved. This being the case, the temperature state before the impact is estimated and imposed as an initial condition immediately prior to impact. During the impact event, changes in temperature state due to deformation and shock propagation are still dealt with via the equation of state and conservation equations.

In developing the initial temperature conditions, the effects of stagnation temperature, airflow through the slider gap, and friction are considered as heat sources. Based on the work of Korkegi and Briggs [29,30], all three sources are assumed to be of the same temperature for modeling purposes. Furthermore, frictional heating and aerodynamic heating in the gap are assumed not to occur at the same place at the same time, and so are dealt with as a single, uniform source as shown in Figure 18.

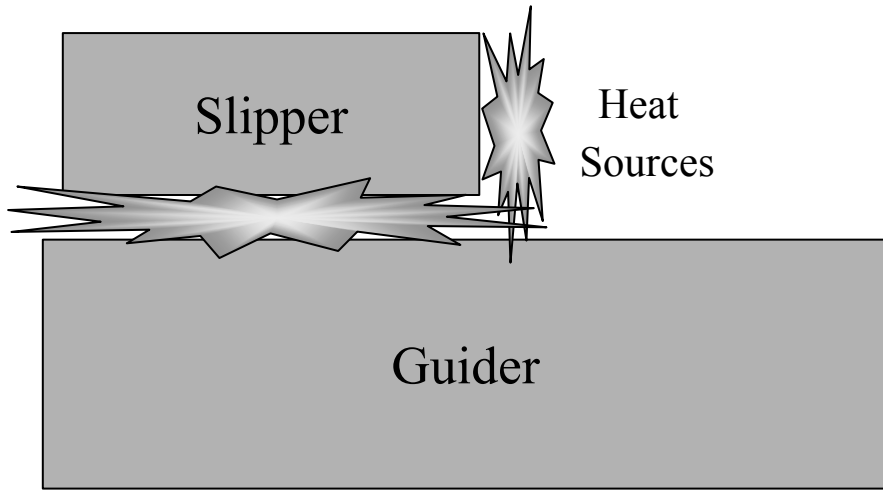


Figure 18. Heat Inputs to System

The simplest method used here assumes that the slider has arrived at a uniform, steady state temperature equal to the heat sources. Furthermore, the rail can be said to be at

room temperature because the heat source (moving with the slipper) is at the impact region for too small of a time for heat to be conducted into the rail. To establish a possible temperature regime, the test profile in Figure 16 has been considered. At 10,000 fps in helium, the stagnation temperature would be 1200 K. A source strength temperature range of 298 K to 2500 K has been examined.

To improve the fidelity of this model, a two-dimensional transient heat transfer solution is employed within the slipper. The variation in temperature of a two-dimensional bar is governed by a partial differential equation called the heat conduction equation [78]:

$$\frac{\partial u}{\partial t} = \alpha \left(\frac{\partial^2 u}{\partial x^2} + \frac{\partial^2 u}{\partial y^2} \right) \quad t > 0 \quad (25)$$

where α is a constant known as the thermal diffusivity, and is defined as

$$\alpha = \frac{\kappa}{\rho c_v} \quad (47)$$

Here, κ is the thermal conductivity, ρ is the density, and c_v is the specific heat of the material.

For VascoMax 300, a maraging steel from which many slippers are made, κ , ρ , and c_v are temperature dependent. To simplify, these values are taken to be constant, and their values at 700 K were used:

$$\kappa_{700K} = 3.0807 \times 10^6 \frac{g \cdot cm}{s^3 \cdot K}$$

$$c_{v700K} = 8.583 \times 10^6 \frac{cm^2}{s^2 \cdot K}$$

$$\rho_{700K} = 7.9173 \frac{\text{g}}{\text{cm}^3}$$

$$\alpha_{700K} = 4.5118 \times 10^{-2} \frac{\text{cm}^2}{\text{s}}$$

The heat equation can now be solved using the simple finite difference algorithm derived earlier:

$$u_{i,j}^{n+1} = u_{i,j}^n + \alpha \frac{\Delta t}{l^2} \left[(u_{i-1,j}^n - 2u_{i,j}^n + u_{i+1,j}^n) + (u_{i,j-1}^n - 2u_{i,j}^n + u_{i,j+1}^n) \right] \quad (41)$$

where u is the temperature and Δt is the time step. Using 735 cells, the resulting temperature profile in the slider after 5 seconds is shown in Figure 19, where white represents the source temperature and each consecutive color contour indicates a drop in temperature.

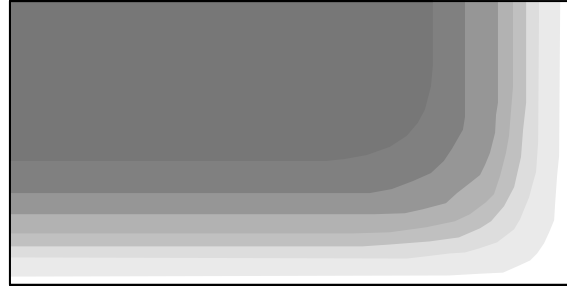


Figure 19. Time Dependent Slider Temperature Profile at 5 Seconds

In this case, the contact surface is at the source strength temperature, while the temperature drops away from the surface.

Although the heat source is present over the impact area of the rail for only a short period of time, analysis of the heat conduction can still be performed. Baker et al [79]

have developed a steady state solution of thermal profiles generated in a rail for high-speed sources. The steady state temperature distribution in the rail is given by:

$$u_{ss}(\xi, \eta) = \frac{\lambda \eta}{\pi} \int_0^1 e^{-\lambda(\xi-\zeta)} f(\zeta) \frac{K_1(\lambda R)}{R} d\zeta \quad (48)$$

where ξ and η are non-dimensionalized coordinates attached to the source, λ is a non-dimensionalized parameter incorporating material density, velocity, specific heat, thermal conductivity, and source length. K_1 is the second kind modified Bessel's function of order one, and R is a function of the coordinates.

Lambda, defined by:

$$\lambda = \frac{\rho v c_v l}{2\kappa} \quad (49)$$

represents the ratio time scales for velocity and diffusion. Since the velocity is very high compared to the rate of thermal diffusion, λ is expected to be very large. Using material properties for 1080 steel, which is what the Holloman High Speed Test Track (HHSTT) rail is made from:

$$\rho = 7.85 \frac{\text{g}}{\text{cm}^3}$$

$$c_v = 5.024 \times 10^6 \frac{\text{cm}^2}{\text{s}^2 \text{K}}$$

$$l = 4.37 \text{ cm}$$

$$\kappa = 4.774 \times 10^6 \frac{\text{g cm}}{\text{s}^3 \text{K}}$$

$$v = 2 \times 10^5 \frac{\text{cm}}{\text{s}}$$

where ρ is density, v is source velocity, c_v is specific heat, l is the source length, and κ is thermal conductivity, we get:

$$\lambda = 3.61 \times 10^6$$

Solving Equation 48, the resulting temperature profile for a unit non-dimensionalized source strength is displayed in Figure 20. In this figure, the length of the y -axis is 2000 times the length of the x -axis to show detail. Each color shade represents a 10% decrease from the source temperature.

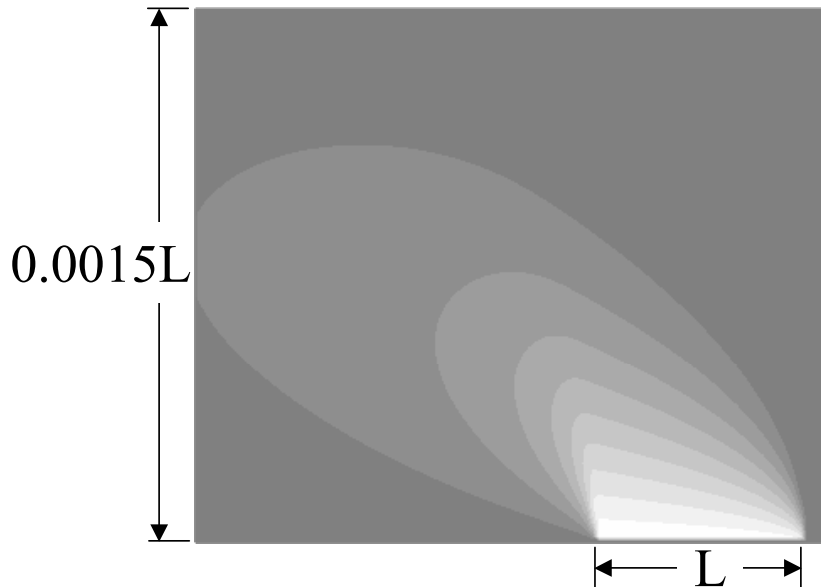


Figure 20. Steady State Rail Temperature Solution

IV. Results and Discussion of Numerical Simulations

This chapter describes the simulations conducted, the models used, and the results of the simulations. The numerical studies performed have been designed to explore the physics leading to gouge development, and the relationship between gouging and temperature. The simulation plan consists of simulations involving the effects of temperature, friction, different CTH numerical options, and model characteristics.

Simulation Plan Overview

An overview of the test plan can be laid out as follows:

- Baseline oblique impact
- Grid convergence studies
- Uniform slider temperature: 500 K, 1000 K, 1500 K, 2000 K, and 2500 K
- Slider temperature contours: 500 K, 1000 K, 1500 K, 2000 K, and 2500 K sources
- Rail temperature with slider contours: 500 K, 1000 K, 1500 K, 2000 K, and 2500 K sources
- Asperity impacts: Asperity with 0.02, 0.1, and 0.5 cm diameters
- Horizontal Velocity: Higher and lower velocities than the baseline test
- Vertical Velocity: Higher and lower velocities than the baseline test
- Geometry: Smaller slipper
- Increased rail yield stress (steel) model
- Strain-rate dependent slider model
- Parallel plate models

- Three-dimensional model
- Eulerian mixed cell treatment: Zero yield stress, average yield stress, and average yield stress not including voids
- Material interface models: Boundary Layer Interface and Slide line
- Friction coefficients: 0.1, 0.2, and 0.3

Modeling Technique and Baseline Oblique Impact

In order to initiate gouging, some impact event must occur. Considering past work and track conditions, several scenarios could be considered. These include but are not limited to:

- Oblique impact (slipper has both horizontal and vertical velocities)
- Asperity impact with slipper gap
- Asperity impact without slipper gap
- Oblique impact with gap, landing on asperity

The primary impact model considered in this research is the oblique impact model, which represents the collision between the slipper and rail due to known sled oscillations. The oblique impact model used here is a two-dimensional plane strain model of a slipper and rail as shown in Figure 21. In this case, the slider is moving at hypervelocity from left to right across the rail, and has relatively small downward vertical velocity component. An impact event is generated when the slider collides with the rail, resulting in a high velocity impact at a very shallow angle.

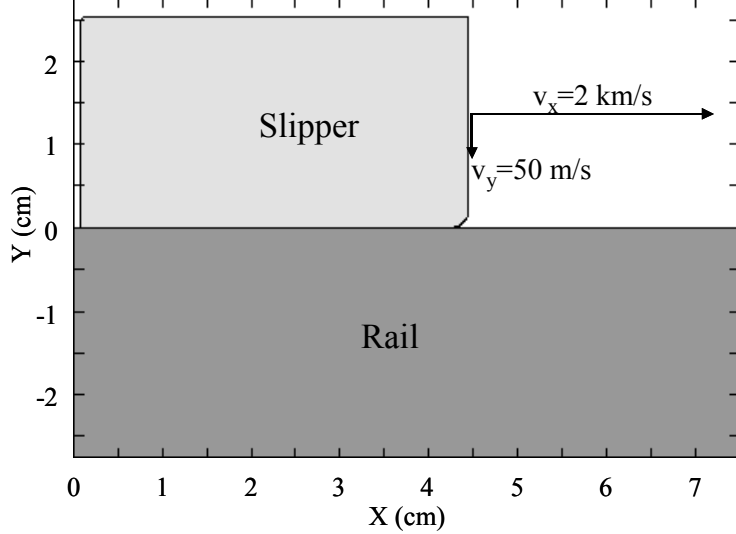


Figure 21. Oblique Impact Scenario

A “baseline” case is constructed to be the norm against which other studies will be compared. For this reason, the baseline case is not too dissimilar to the models of Barker [19], Tachau [20], and Schmitz [22]. The slider is 2.54 cm (1.0 in) thick by 4.37 cm (1.72 in) with a 0.2 cm (.079 in) radius chamfer on the leading edge in contact with a rail. The rail is 2.76 cm (1.09 in) thick by 7.5 cm (2.95 in) long, which takes it into contact with the boundary of the computational domain on the left, right, and bottom. The initial temperature was 298 K throughout the problem domain, and the atmosphere or helium environment was not modeled (i.e. it is in a vacuum).

In the finite volume method, boundary conditions are described as flow conditions at or through outside cell edges. The boundary condition along the bottom and sides of the rail prevents the flow of mass but allows pressure to exit the boundary at the material sound speed. This boundary condition is used to approximate an infinite or semi-infinite medium [54]. The boundary condition implemented on the top of the computational

domain uses an extrapolated pressure method that sets the pressure to zero on the boundary and allows mass to pass out of the domain across the boundary. This boundary condition linearly extrapolates the pressure in the two adjacent cells to the boundary, and is used to allow the slider and any fragments to exit the mesh [54].

To initiate an oblique impact event, the slider is given a horizontal velocity component of 2.0 km/s (6,562 ft/s) and a vertical component of 50 m/s (164 ft/s) as initial conditions.

Models of sled dynamics by Hooser using the Dynamic Analysis and Design System (DADS) [77,80] have shown that more realistic vertical impact velocities are 80 to 100 inches per second. Load and vibration simulations of the sled assembly performed at Holloman AFB indicate that a vertical velocity of 1 to 2 m/s would be a more realistic representation of events. However, the slider mass used in the simulations is much less than the mass of an actual sled. The kinetic energy of a 227 kg (500 lb) sled moving at 1 m/s is equivalent to the model's 89.77 g slider at 50.26 m/s, which is why 50 m/s was chosen. The two materials are already in contact along the slider length, representing the instant that any gap between the two materials is closed and the impact begins.

At the test track, the rail is constructed of 1080 steel crane rail, and typically covered with some kind of coating such as primer. The rail has been modeled here as iron using the Johnson-Cook viscoplastic constitutive model (Equation 18) with the following parameters:

$$A = 1.7526 \times 10^9 \frac{\text{g}}{\text{cm} \cdot \text{s}^2}$$

$$B = 3.8019 \times 10^9 \frac{\text{g}}{\text{cm} \cdot \text{s}^2}$$

$$C = 0.06$$

$$n = 0.32$$

$$m = 0.55$$

$$T_M = 1835.7 \text{ K}$$

and the Sandia National Laboratories SESAME tabular EOS for iron. This EOS tabulates pressure, internal energy, and entropy and includes four solid phases (alpha, gamma, epsilon, delta), melting, and vaporization. It is said to agree well with most experimental data, including impact and penetration experiments and wave profile measurements, which show multiple shock behavior [59]. Slippers are normally constructed from high-strength steels such as VascoMax maraging steel [81]. The slider was modeled as VascoMax 250 steel using the Steinberg-Guinan-Lund model (Equation 19) with the following constants:

$$\rho_0 = 8.129 \frac{\text{g}}{\text{cm}^3}$$

$$G_0 = 7.18 \times 10^{11} \frac{\text{g}}{\text{cm} \cdot \text{s}^2}$$

$$Y_0 = 1.56 \times 10^{10} \frac{\text{g}}{\text{cm} \cdot \text{s}^2}$$

$$A = 2.06 \times 10^{-12} \frac{\text{cm} \cdot \text{s}^2}{\text{g}}$$

$$B = 3.15 \times 10^{-4} \text{ 1/K}$$

$$\beta = 2.0$$

$$n = 0.5$$

$$Y_{max} = 2.5 \times 10^{10} \frac{\text{g}}{\text{cm} \cdot \text{s}^2}$$

$$\gamma_0 = 1.67$$

$$a = 1.2$$

$$T_{m0} = 2310 \text{ K}$$

$$\varepsilon_i = C_1 = C_2 = U_K = Y_P = Y_A = Y_{max} = 0.0$$

and the SESAME EOS model for VascoMax 300 steel, which is the same EOS for iron but with a density-scaling factor. The different constitutive models were used because Johnson-Cook material data for the slipper was not available, and vice versa.

The computational mesh is loosely based on the work of Schmitz [22,82]. Since Schmitz was able to match experimental data from the test track, his grid was used as a starting point. From there, a convergence study resulted in a grid composed of 53,578 rectangular cells, the ones near where gouging will occur being most refined at 0.005 cm on a side. Since the location of the gouge moves with time, but the Eulerian mesh does not, a velocity was imparted to the entire system to maintain the gouge within the region of the most refined cells. The resulting mesh is shown in Figure 22. Information on location, pressure, temperature, and stress at each grid point was stored. Grid size can have a considerable effect on gouge modeling as demonstrated by Tachau's work [20], where he found that it took up to 40 μs for a noticeable gouge to develop. An example of Tachau's work has been repeated, giving identical results. However, by using a more refined grid, gouging developed in just 4 μs .

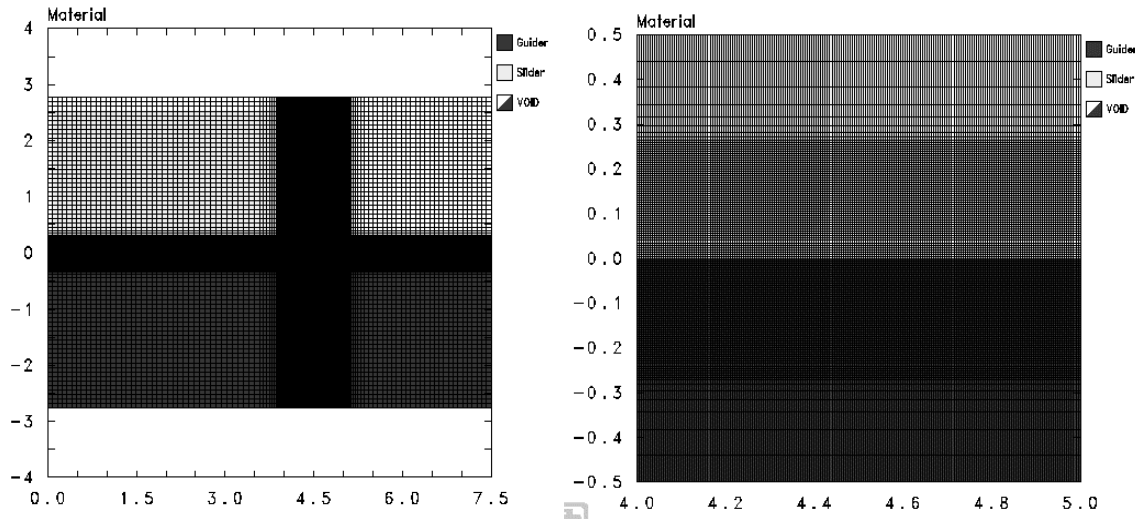


Figure 22. Computational Grid

In most of these runs, no frictional or sliding algorithm has been implemented.

Without an interface sliding algorithm specified, CTH assumes that when two materials are in contact, they have the same velocity. This results in the slider and rail being artificially joined together as one object. In this case, interface behavior is dictated by how multi-material cells are treated. Since CTH uses an Eulerian grid, cells at the material interface tend to contain both slider and rail materials. Here, CTH has been configured to set the yield stress in such mixed cells to the sum of the fraction weighted yield stresses of the individual materials within the cells, including any voids. This results in the materials being joined, and the materials cannot move separately unless the average shear strength is overcome.

Baseline Results. At the problem start time, the slider has initial downward and horizontal velocities, and the two materials are in contact along the slider length. This

represents the instant that the gap between the rail and slider is closed and the impact begins.

The development of gouging begins at the leading edge of contact. Due to the vertical component of the impact, the slider penetrates slightly into the rail. Figure 23, with its y -axis greatly magnified, shows this penetration at 0.5 μ s.

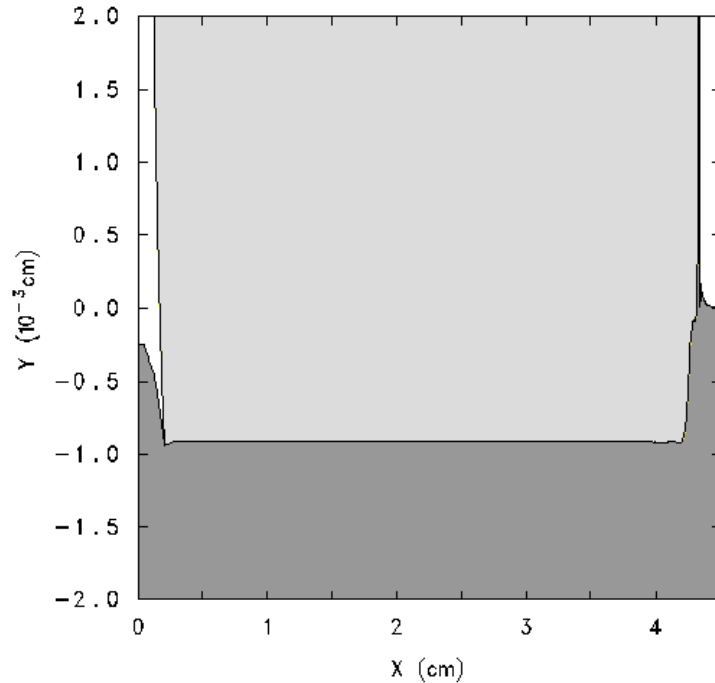


Figure 23. Slider Penetration in Baseline Impact at 0.5 μ s

At the same time, shear forces at the rail surface exceeding 500 MPa (72.5 ksi), as shown in Figure 24, cause material at the rail surface to begin moving in the direction of the slider. Some of the rail material in front of this movement is displaced upward in front of the slider, forming a small hump. By 0.5 μ s, the slider has pushed a small

amount of rail material in front of it, as shown in Figure 25. At this point, this rail hump is less than 0.005 cm tall.

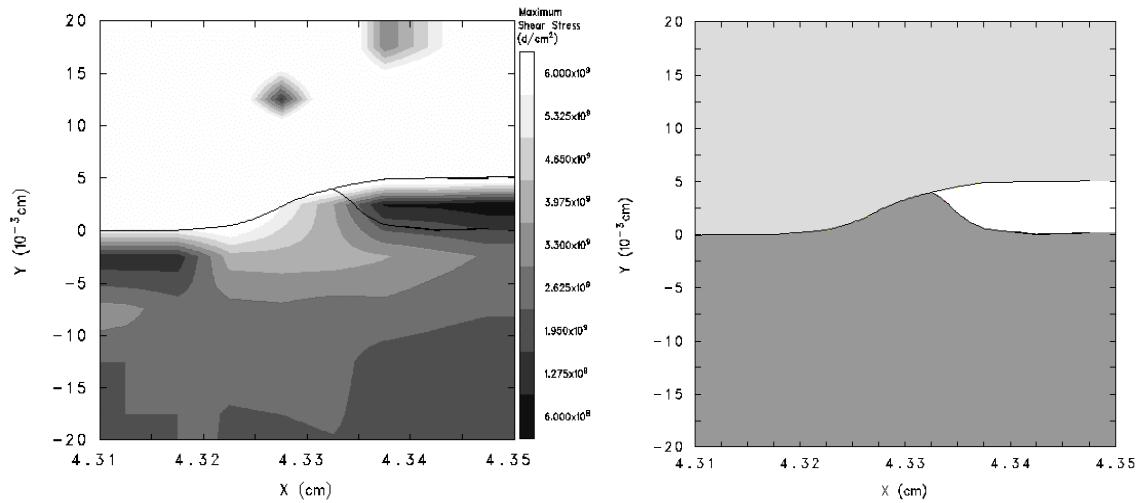


Figure 24. Shear Forces at 0.5 μ s

Figure 25. Hump Development at 0.5 μ s

Growth of the rail hump combined with the slipper penetration due to the vertical component of impact creates a region where there is a vertical component of the material interface. This introduces a small area where impact is occurring horizontally, resulting in hypervelocity impact. This area will be called the interaction region.

The interaction region also moves at about half the velocity of the slipper. This being the case, the rail hump is quickly overrun by the slipper (Figure 26). This results in an antisymmetric hump feature. This means that features in one material are similar to features in the other, but in the reverse direction.

Up until 4.5 μ s, the geometry does not change much, other than that the antisymmetric humps have grown in size, thus increasing the size of the horizontal impact region

(Figure 27). This is due primarily to the fact that the slider has continued to penetrate into the rail due to the vertical component of the initial impact.

Figure 27 includes material tracers to help indicate the nature of material flow. The groups of three tracers initially started as straight columns. It is apparent that the tracer in the rail closest to the interaction region is being pulled in the slider direction due to shear near the interface.

Between 4.0 and 4.5 μ s, the material near the interaction region begins to exhibit fluid like behavior due to the high velocity and the high resulting strain rate. Although the constitutive equations used result in increased yield strengths at higher strain rates, the momentum of the material becomes so high that the slider material begins to form a material jet that impinges downward into the rail. At this point, this plastic flow also accelerates the growth of the interaction region between the slider and rail.

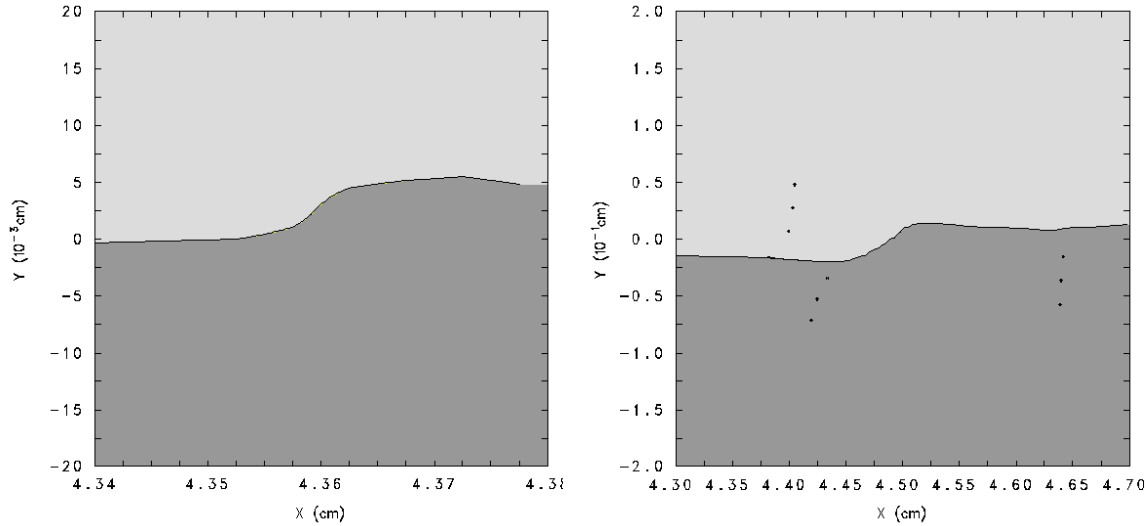


Figure 26. Hump Overridden at 1.0 μ s

Figure 27. Growth of Asymmetric Interaction Region at 4.5 μ s

By 5.0 μ s, a void begins to develop between the rail and slipper behind the interaction region as seen in Figure 28. The void is caused by the fact that the jet is penetrating further into the rail than the bulk of the slipper. Now, the primary mechanism of penetration is changing from the vertical impact to jetting penetration.

By 6.5 μ s, the rail jet has clearly separated from the bulk material, and penetrates significantly deeper than the bottom of the rest of the slipper behind it (Figure 29). Now the pattern of the resulting gouge is becoming apparent: gradually deepening from the trailing edge toward the leading edge, then a steeper rise back to the surface, tipped with a raised leading edge.

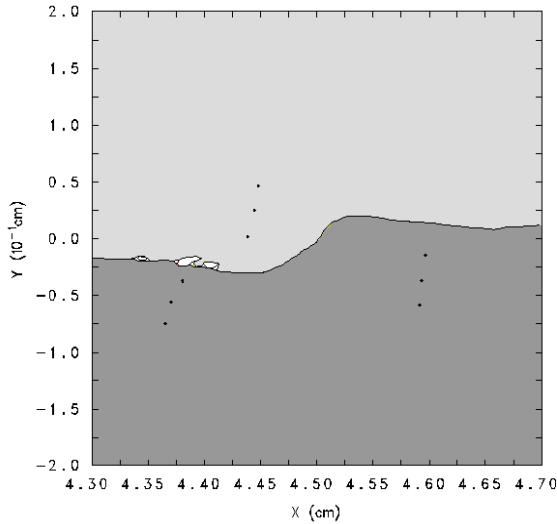


Figure 28. Initiation of Slipper Jet at 5.0 μ s

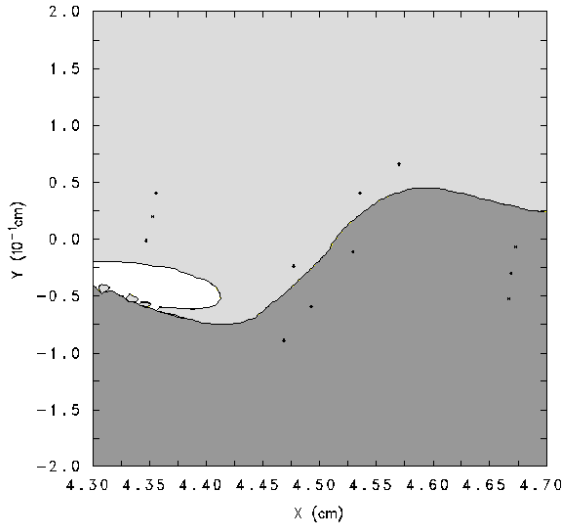


Figure 29. Growth of Gouge at 6.5 μ s

In Figure 30, the newly formed jet of rail material has separated from the bulk of the rail by 9.0 μ s. Throughout the history of the development, and particularly after the formation of the first material jet, the interaction region progressively grows in size. As

this occurs, the jets grow larger and penetrate further, fueling the increase in size of the interaction region and depth of the gouge.

Once the interaction region has developed to this stage, its geometry results in a material instability. That is to say that as long as the region exists with an extension of the rail into the slipper, and the roughly antisymmetric extension of the slipper into the rail, the interaction will continue to cause further penetration. This results in the gouge becoming deeper, which explains why rail gouges are shallow at the initiating end and grow deeper at the leading edge.

As this interaction region grows, two gouges are created: one in the rail behind the interaction region, and one in the slipper in front of it, as seen in Figure 31. If both materials were identical, it is expected that the gouging pattern would be perfectly antisymmetric about the center of the interaction region, with the rail gouge and slipper gouge being identical, but inverted and flipped. Material properties and response are presumed to be the factors that lead to the rail and slipper gouges being different from one another. This leads to the idea that gouge formation can be affected by the choice of materials.

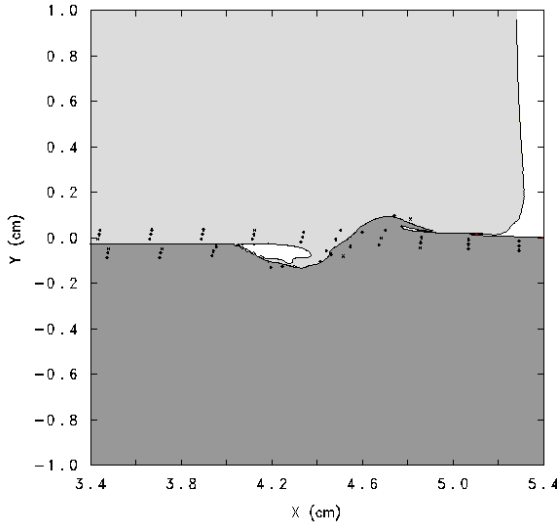


Figure 30. Initiation of Rail Jet at $9.0 \mu\text{s}$

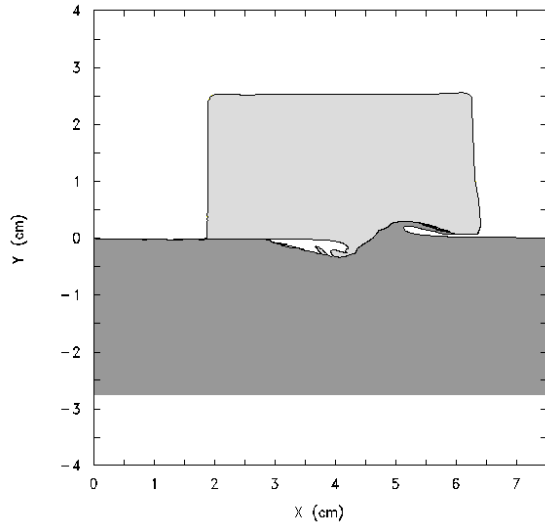


Figure 31. Growth of Gouge at $20.0 \mu\text{s}$

Further growth of the gouging is shown in Figure 32 and Figure 33. In Figure 32, the back of the slipper is passing over the gouge, and will soon overtake the interaction region. Figure 33 shows the gouge in its final stages. The gouge will be terminated as the bulk of the slipper completely passes over the interaction region, ending the interaction. Once this region falls behind the slipper, the base of the rail jet is left behind and forms the raised lip of the gouge seen in experiments. This also explains why the length of rail gouges is limited to the length of the slipper. At $50 \mu\text{s}$, only the base of the slipper jet remains in the interaction region, and the development of the gouge is effectively over. Here we can see the aforementioned gouge description, indications of the raised lip, and material deposits in the gouge.

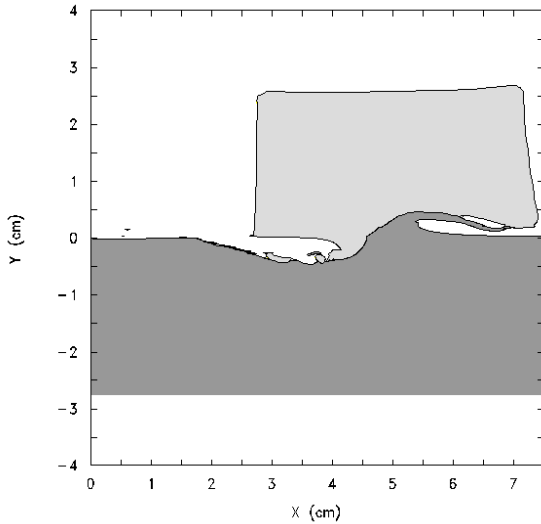


Figure 32. Growth of Gouge at $30.0 \mu\text{s}$

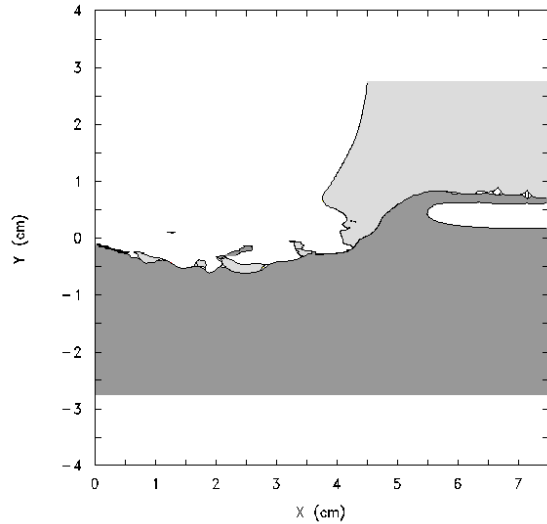


Figure 33. Resulting Gouge at $50.0 \mu\text{s}$

To examine how the gouge grows with respect to time, the chart in Figure 34 compares the height of rail penetration into the slipper, slipper penetration into the rail, and penetration of a slipper with no horizontal velocity but with the same vertical velocity. In the chart, $y = 0 \text{ cm}$ represents the initial rail surface. The lines below $y = 0 \text{ cm}$ chart the maximum penetration of the slipper into the rail, and the line above $y = 0 \text{ cm}$ marks the maximum penetration of rail material into the slipper. It is observed that even without a horizontal velocity, the 50 m/s vertical velocity is significant enough to penetrate into the rail. For the oblique impact, the amount of penetration is initially very similar to vertical impact. At just over $4.0 \mu\text{s}$, however, the gouge begins to develop and the rate of penetration increases significantly. This major departure from the vertical impact penetration signals an important event at this time. Referring to Figure 27 and Figure 28, this point in time corresponds to the initial development of the jets, and the

point transition between when rail penetration is dictated by jet formation rather than vertical impact.

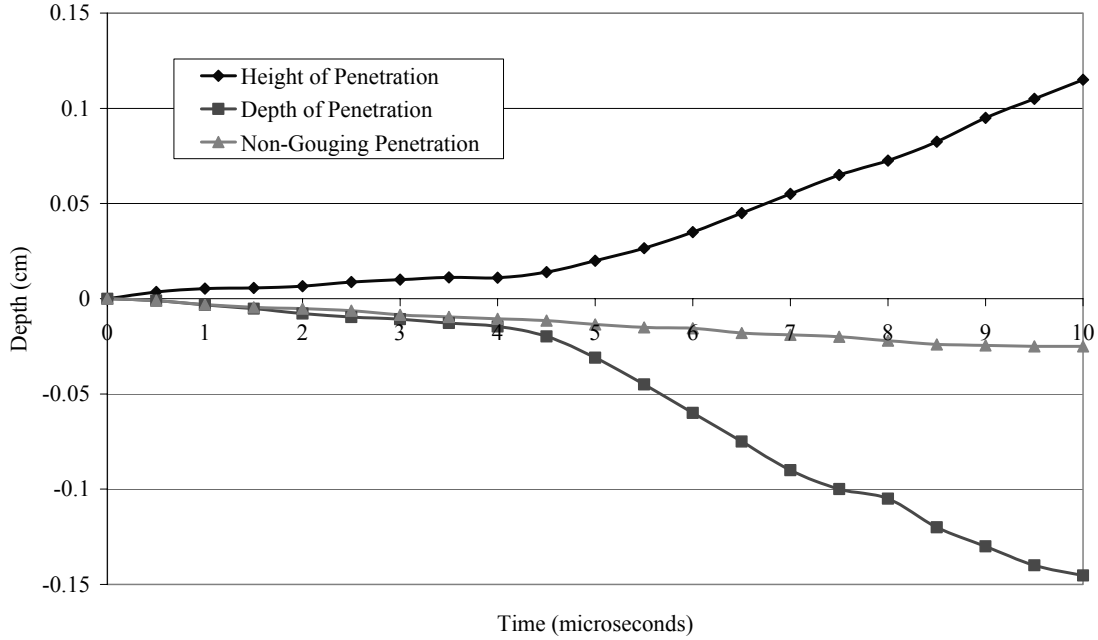


Figure 34. Maximum Gouge Depth Versus Time

By following the motion of the material tracers, it is seen that some material near the surface is directed into the jet, while deeper material is compressed below the developing gouge. Figure 35 shows the rail, slipper, and tracers at $t = 0$. The black lines indicate approximately the dividing line between materials that will eventually be jetted and materials that will be compressed below the gouge for the first 25 μ s. Note that the x and y scales are different to magnify the y direction.

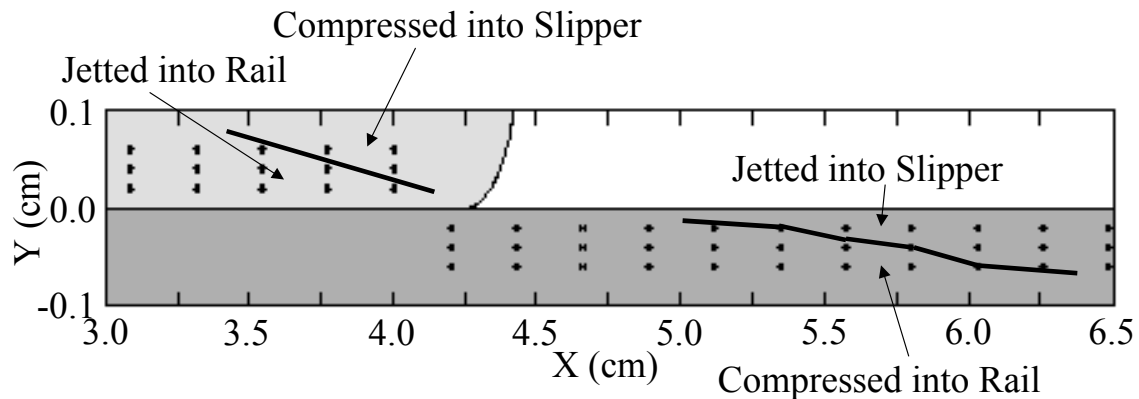


Figure 35. Divisions Between Compressed and Jetted Materials

To further study the flow of material during gouging, velocity vectors are used to visualize the motion. Figure 36 shows velocity vectors at 4.5 μ s. For clarity, only the velocity of the rail is shown. In general, rail material in front of the gouge is being pushed forward, and material below the gouge is being forced downward. Material at the interface in front of the gouge is being propelled near or at the velocity of the slipper, and has a small upward velocity component. Figure 37 shows velocity vectors at 9.0 μ s. By this time, the rail jet is moving with the same velocity of the slipper. Toward the back of the gouge, material moves upward due to recovery of the elastic component of its stress.

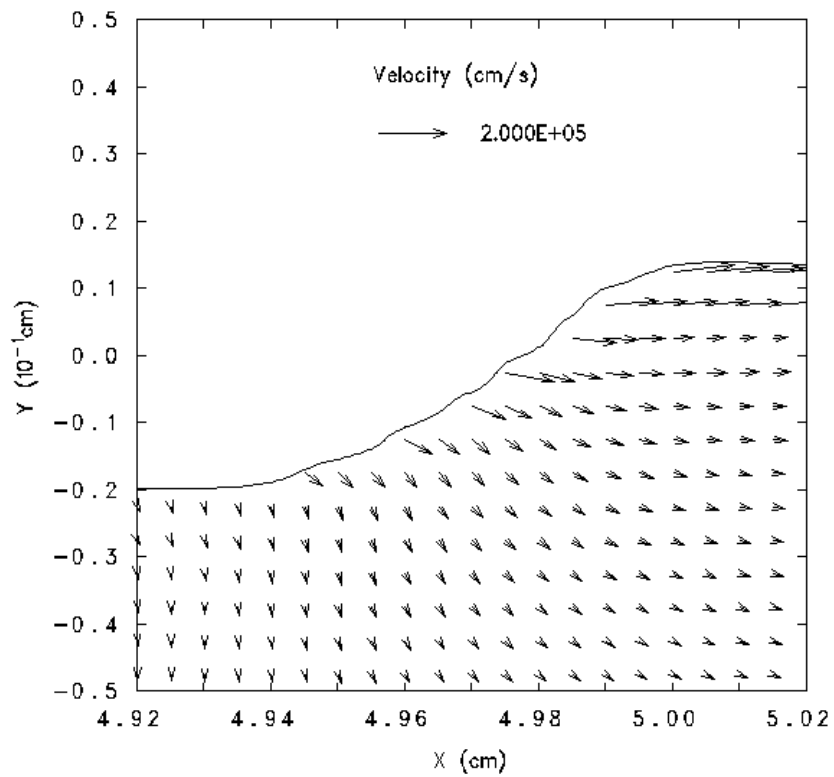


Figure 36. Velocity Vectors at $4.5 \mu\text{s}$

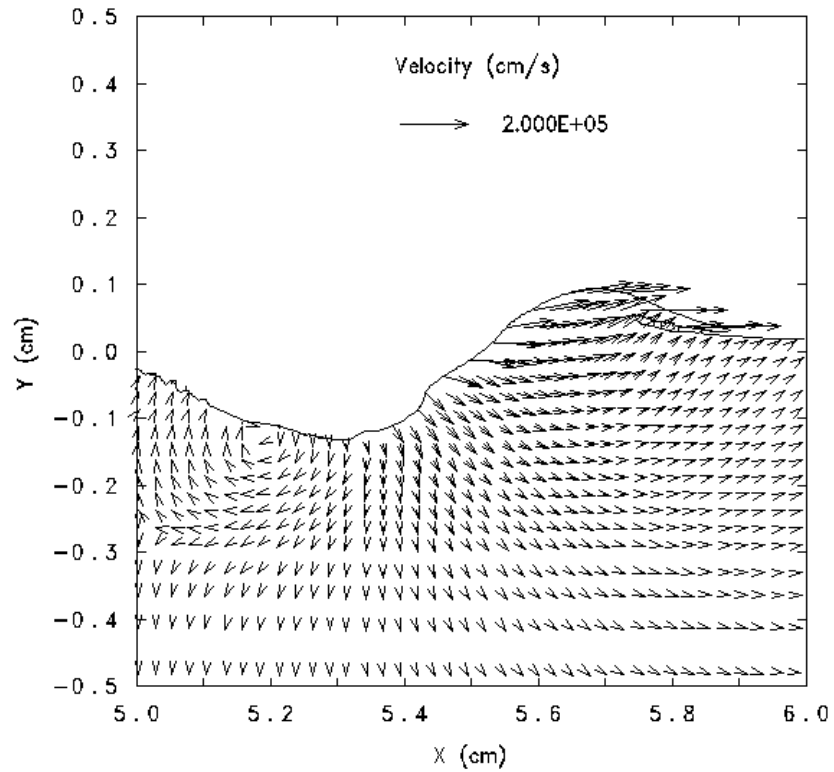


Figure 37. Velocity Vectors at $9.0 \mu\text{s}$

Stress can be broken down between pressure (spherical stress) and deviatoric components. In hypervelocity impact, the pressure component dominates the material response. The pressure is a byproduct of the equation of state and also leads to an increase in temperature. Barker, Trucano, and Munford [19], Tachau [20], and Schmitz and Schmitz [22] have all observed that the development of a high-pressure core at the location of the gouge affects the development of the gouge. Looking at pressure, Figure 38 depicts the pressure field at 3.0 μ s. The initial development of a high-pressure core can be seen centered on the interface between the slider gouge and the rail gouge. The greatest pressure in this region is about 4.9 GPa (710 ksi). Much of this pressure core greatly exceeds the yield strength of the materials involved (0.18 GPa for the rail and 1.56 GPa for the slider). This leads to and sustains a region of plastic flow.

The initial impact forces are great enough to cause plasticity at the interface. Due to the plastic deformation of the slider penetrating into the rail and the rail material pushed in front of it, an interlocking contact region where the slider is impacting horizontally into the rail is created. This impact creates the high-pressure core centered on the point where the material interface is most normal to the hypervelocity flow, labeled as point A in Figure 38. This point tends to define the center of the interaction region. The pressure is great enough to cause the material in this location and the area nearby to continue to yield, allowing additional deformation. The additional deformation increases the size of the interlocking region, which increases the size of the high-pressure and high stress region. This, in turn, increases the size of the plastic region, allowing the deformation to continue to grow. Because the physical features of a gouge cause the gouge to continue to grow in this manner, gouging can be seen as a material instability.

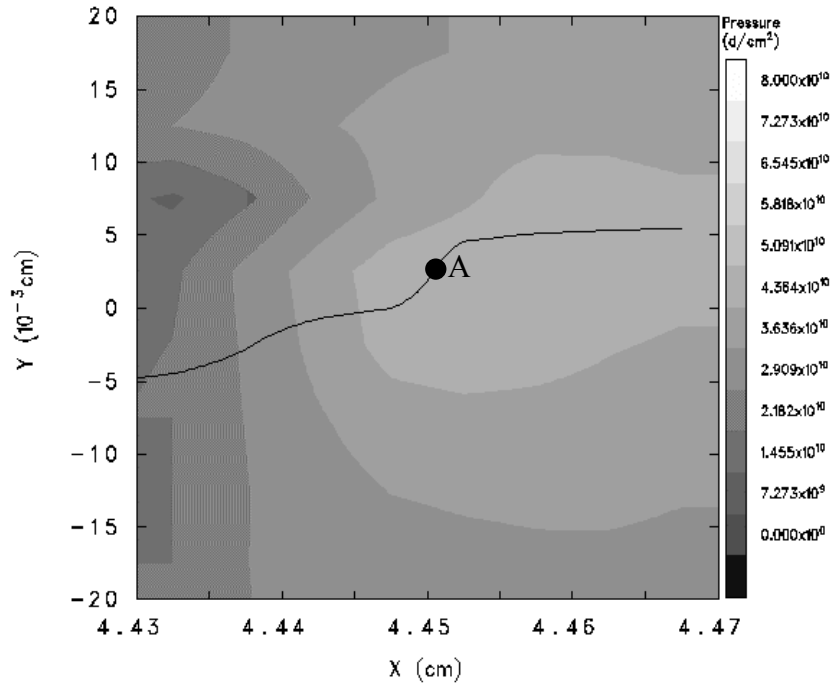


Figure 38. Development of High-Pressure Core at 3.0 μ s

By 4.5 μ s (Figure 39), the maximum pressure corresponds to roughly 7.8 GPa (710 ksi), and the area of pressure exceeding the flow stress has grown larger. Figure 40 shows the pressure field at 9.0 μ s. While the area of high pressure has continued to grow larger, the maximum pressure does not increase any further.

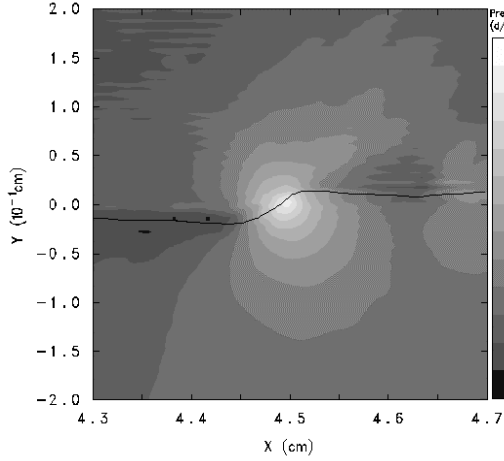


Figure 39. Growth of High-Pressure Region at $4.5 \mu\text{s}$

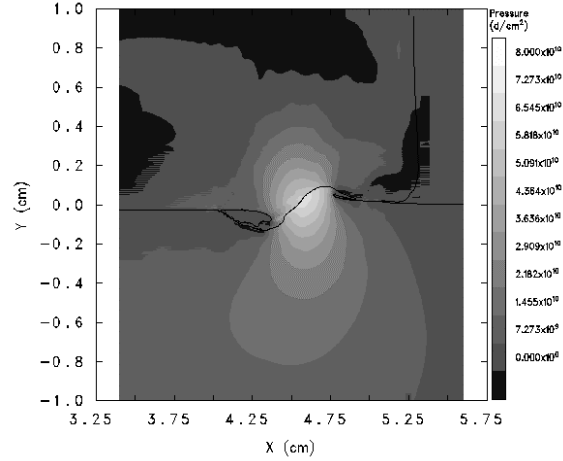


Figure 40. Growth of High-Pressure Region at $9.0 \mu\text{s}$

In high velocity impact dynamics, the creation, propagation, reflection, and interaction of shock waves can affect the material response. Figure 41 shows the location of the stress wave due to the oblique impact at $1.0 \mu\text{s}$, described here by an instantaneous change in stress. Stress waves are initiated at the impact interface, and propagate into both the slipper and the rail at the local sound speed, which is near 4.6 km/s . Material behind the wave has begun to respond to the initial impact. Material in front of the wave is still at its initial state and has not yet experienced any perturbation due to the impact.

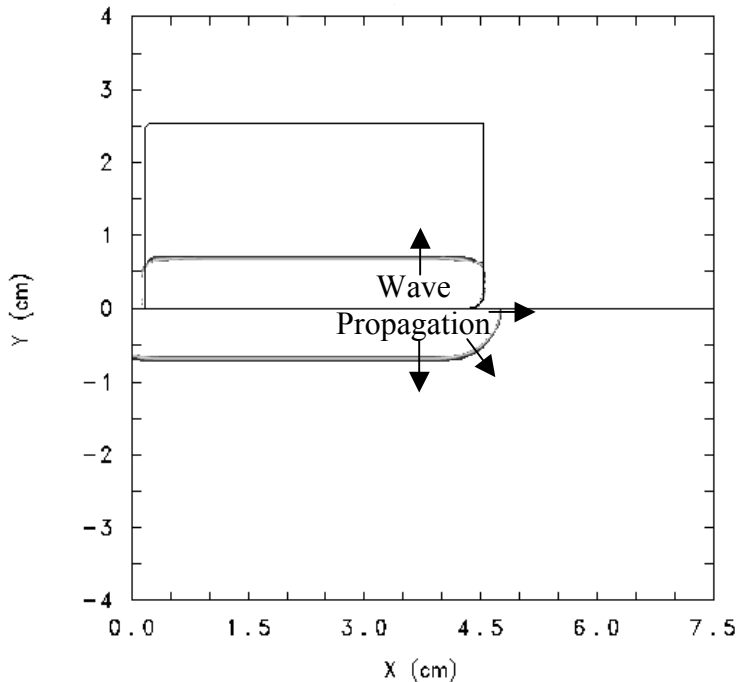


Figure 41. Stress Wave Propagation at 1.0 μ s

Since the deformation transitions from impact penetration to gouge propagation at around 4.0 or 4.5 μ s, this would be a good time to examine the stress wave to see where it may be interacting. At 4.5 μ s, it is seen in Figure 42 that the wave in the rail is still propagating away from the slipper. In the slipper, the stress wave is not obvious because it has just reached the top of the slipper and is about to reflect back. Reflection of this type relieves the stresses created by the initial wave, and arrives back at the material interface after 9.0 μ s. At this point, the wave may travel across into the rail. However, by this time the stress wave is insignificant compared to the size and magnitude of the high-pressure region generated by the gouging. Since these stress waves are not interacting near the location of gouge formation while the gouge is developed, it is unlikely that the wave propagation is influential in gouge initiation.

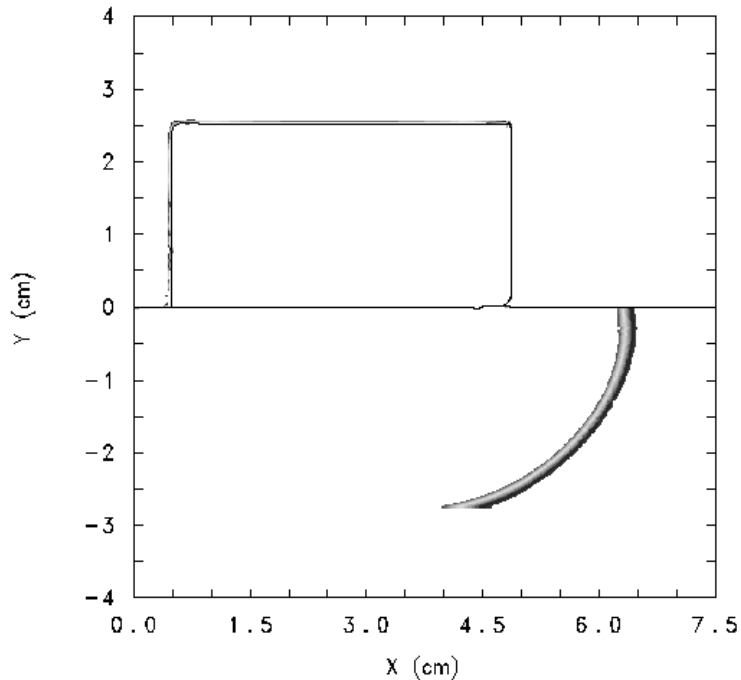


Figure 42. Stress Wave Propagation at 4.5 μ s

Because friction and aerodynamics were not considered except as to determine the initial temperature state, the only heat source in this model is due to mechanical work done on the material in the form of plasticity. The mechanical work associated with the pressure is added to the internal energy of the material. This increase of internal energy directly increases the material temperature. As expected, the temperature and temperature gradient are highest at the slipper/rail interface. Figure 43 demonstrates the temperature generated by plastic deformation at 4.5 μ s. The most plastic strain, and thus the highest temperatures, is generated at the material interface due to shear forces and results in temperatures up to 1480 K in the first microsecond. As time progresses, the peak temperature does not increase but the area of elevated temperature does increase. By 4.5 μ s, material 0.01 cm from the interface has reached 500 K.

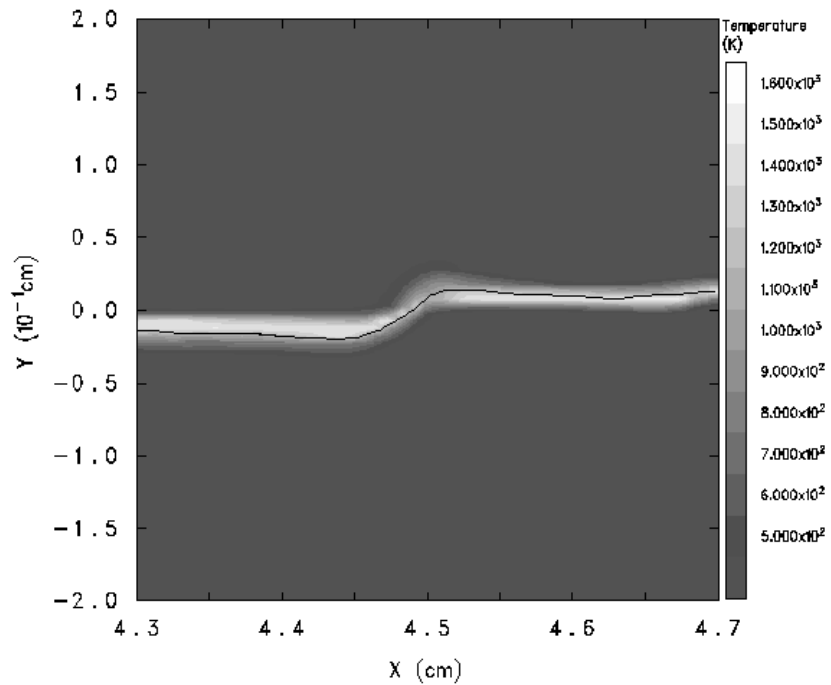


Figure 43. Temperature at 4.5 μ s

Formation of Material Jets in Slipper Impacts

In a hypervelocity normal impact of a projectile against a rigid body, material flow at the leading edge of the projectile is characterized by lateral flow that forms material jets as shown in Figure 44.

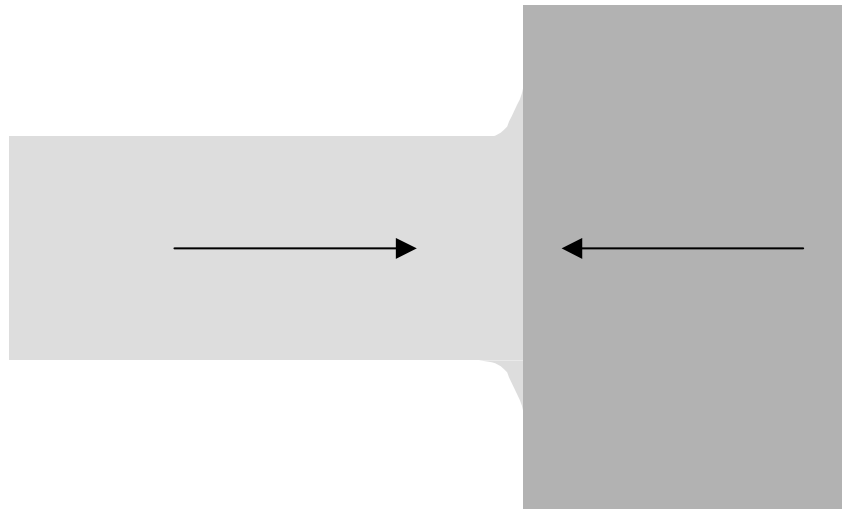


Figure 44. Fluid Jets In Typical Hypervelocity Impact

Considering the idea of an off-axis impact between two materials, one can easily imagine that similar jet formation will occur near the corners that are subject to impact, as in Figure 45.

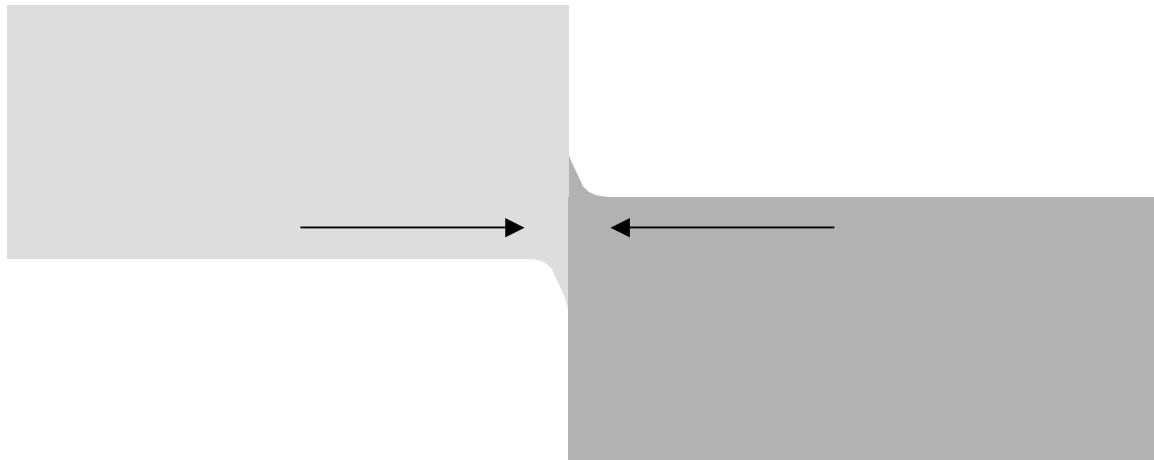


Figure 45. Fluid Jets From Near-Edge Impact of Two Bodies

Extending this idea to an idealized asperity impact as shown in Figure 46, it is easy to predict that jet formation would occur, triggering the development of a gouge.

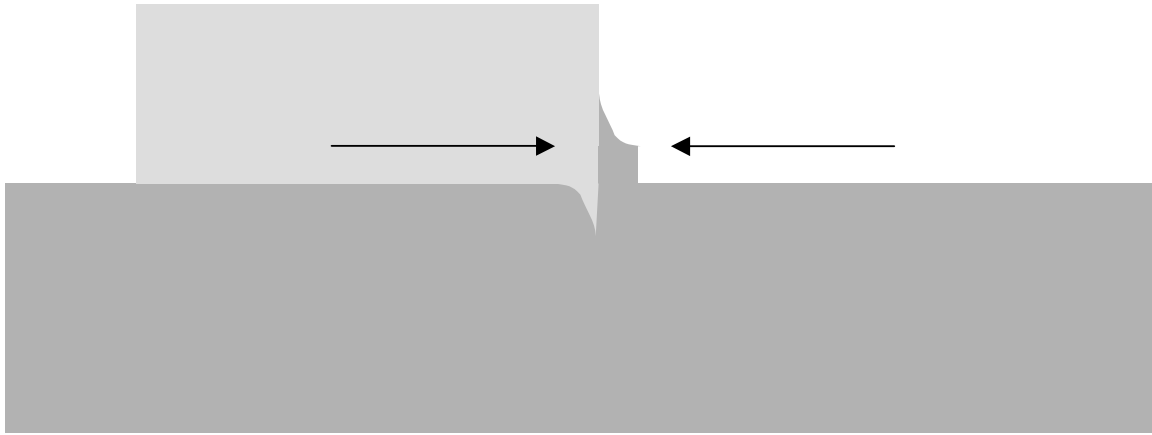


Figure 46. Fluid Jets from Slipper/Rail Asperity Impact

Similarly, in the case of an idealized oblique impact, a penetrated slipper would also produce the impact-induced jets as in Figure 47.

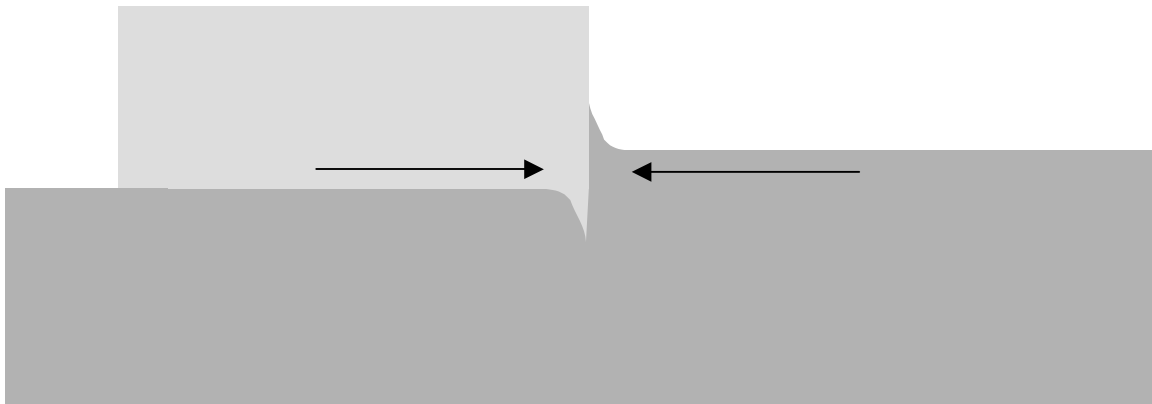


Figure 47. Fluid Jets from Slipper/Rail Penetration Induced Impact

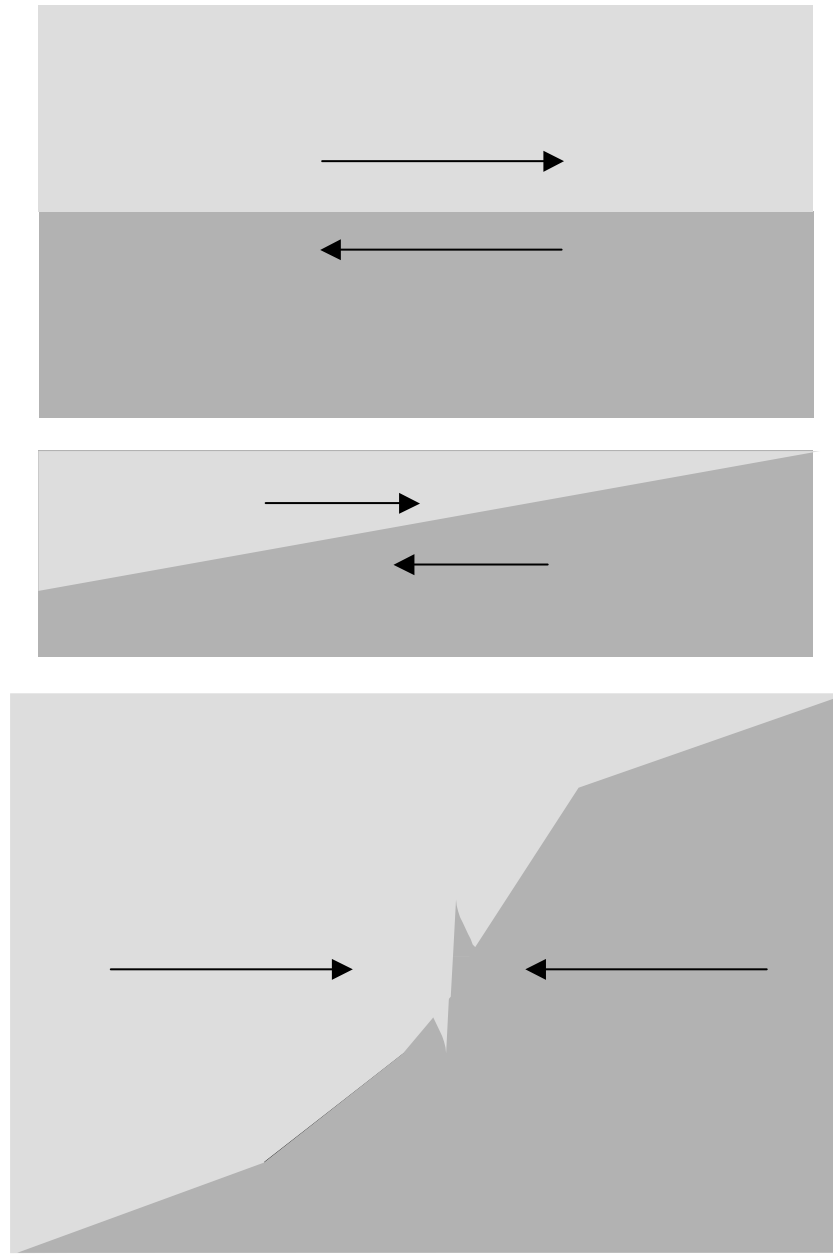


Figure 48. Formation of Fluid Jets Due to Critical Impact Angle
Top) No Angle, No Jets Center) Below Critical Angle, No Jets
Bottom) Critical Impact Angle, Jet Initiation

In these cases, the impact region consists of a normal impact. In the case of sliding, the “impact” is purely tangential and no jetting results. It is speculated, that as the impact

angle is increased, for given conditions there may exist some critical angle at which the normal component of the hypervelocity impact is sufficient to cause jet formation, and pictured in Figure 48. Exceeding this critical angle seems to be the key factor in initiation gouging in oblique impacts, while in asperity impacts this is exceeded immediately.

Temperature Effects

The initial temperature of the system is determined analytically before the numerical calculation is begun. The initial temperature profiles are highly dependent on assumptions made about the heat source. In the material presented, numerical simulations have been performed using source temperatures of 298 K, 500 K, 1000 K, 1500 K, 2000 K, and 2500 K. For the velocity of 2.0 km/s (6562 ft/s), the adiabatic stagnation temp in air, not including any hypersonic effects, is 2285 K (3653 $^{\circ}$ F). At zero pressure, the melting point of the slider is 2310 K (3698 $^{\circ}$ F). Based on the constitutive equations used, it is expected that the yield strength will be decreased, and this is likely to increase the tendency to gouge.

Considering a slider with a uniform temperature, the maximum gouge depth versus time is shown in Figure 49 for various temperatures. Compared to the baseline case at 298 K, as the temperature of the slider is increased to 500 K there is very little difference in the progression of the maximum gouge depth, except for a very small tendency toward the onset of jet formation beginning sooner and the slope of the high-rate region being slightly steeper. After an increase to 1000 K the linear growth rates are still similar, and the earlier start of the high-rate onset and the increased slope of the high-rate region

become more pronounced, and the trend continues at 1500 K. Further increases to 2000 K and 2500 K begin to reverse the trends of the high-rate region. Here, the onset of the higher rate begins to occur more slowly, although the slope remains slightly steeper than at lower temperatures. At 2500 K, the onset point of 6.0 μ s is even slower than the 4.0 μ s onset at room temperature.

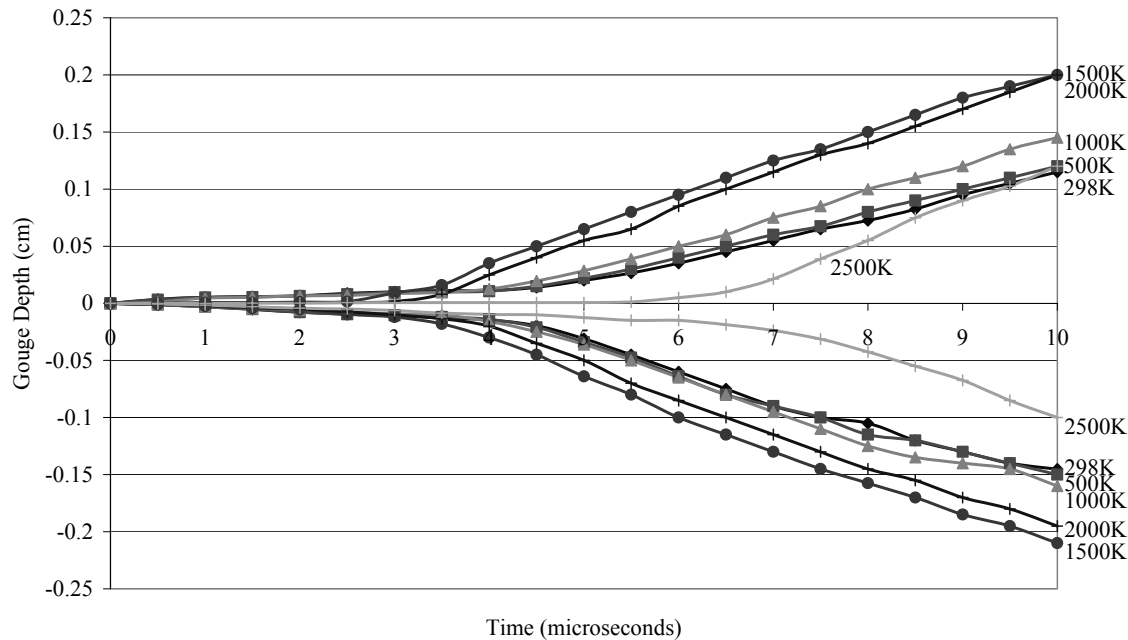


Figure 49. Maximum Gouge Depth Versus Time For Various Uniform Slipper Temperatures

At the elevated temperatures the mechanism of gouging begins to change. At room temperature, the gouge develops at a location based on the small rail hump initially at the leading edge of the slipper. At high temperatures however, multiple gouges are observed, some of which develop away from the leading edge. Figure 50 shows the material interface at 2.0 μ s. Here, a very small amount of the rail has been deformed in front of

the slipper leading edge, but no slipper material is protruding into the rail at this location. But behind the leading edge, the bulk of the slipper has penetrated to 0.004 cm into the rail. It is at the front of this deepest penetration that a gouge will first form.

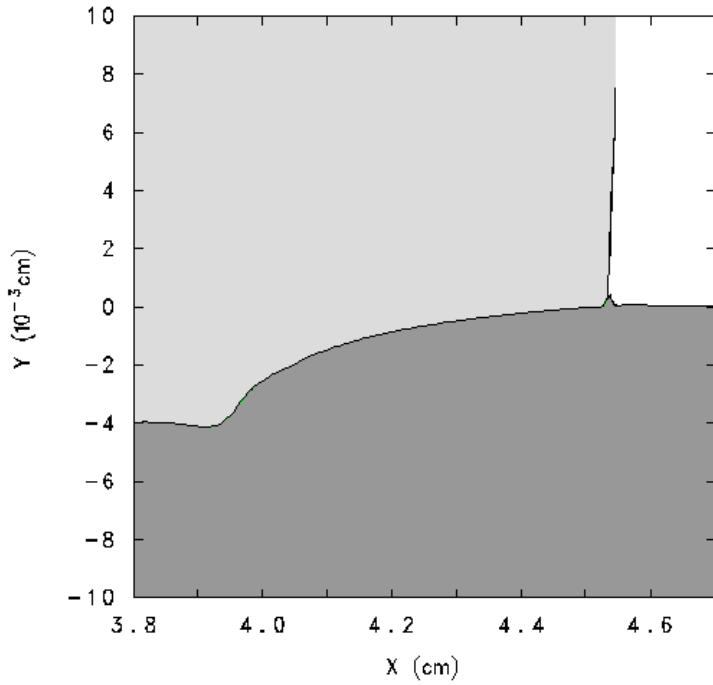


Figure 50. Gouge Initiation with 2500 K Slipper at 2.0 μ s

By 2.5 μ s, the front of the deepest penetration has taken the form of a gouge initiating instability as seen in Figure 51. This becomes the first and primary gouge in this case. The continuing interaction at the leading edge still develops into a gouge several microseconds later, resulting in multiple gouges. The numerical gouge development shown in Figure 51 is not too dissimilar to the schematic representation of gouge formation in the bottom of Figure 48.

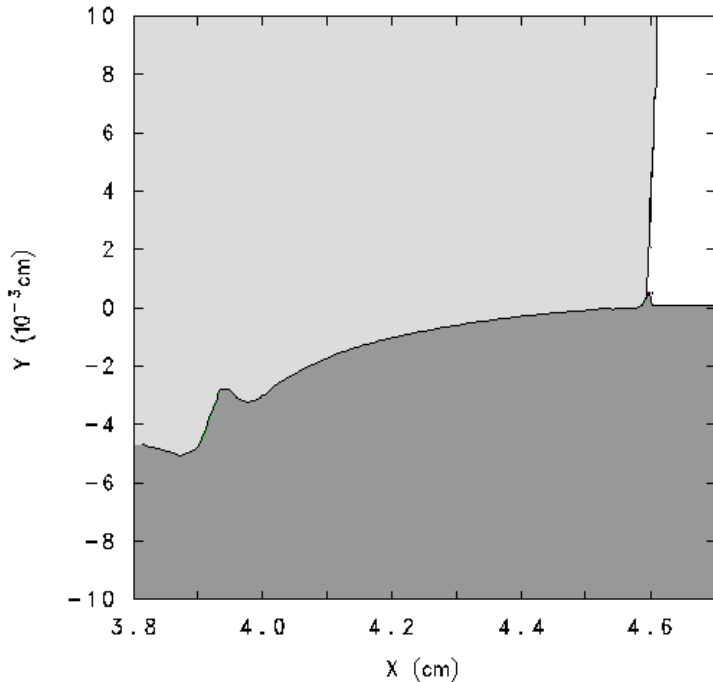


Figure 51. Gouge Initiation with 2500 K Slipper at 2.5 μ s

At temperatures between 298 K and 2500 K, both these mechanisms are present. At the start time, these phenomena are collocated. The leading edge instigated interaction always moves at the same speed independent of temperature. At lower temperatures, the penetration interaction moves at the same speed, and the two phenomena occur together. At higher temperatures, however, the penetration interaction tends to move slower. At 2500 K, the penetration-initiated instability is actually behind the x location of the initial leading edge point (Figure 51). The higher temperatures hinder the leading edge gouge, while the penetration gouge is promoted by it.

Since the size of a gouge increases with time, the size of multiple gouges with respect to each other depends on when they initiate. In the case of the 2500 K slipper, the leading edge gouge is delayed significantly such that the first gouge is always much

larger. But at 1500 K, these two gouges initiate at similar times and develop together. This double gouging is shown at 6 μ s in Figure 52. In this figure, the y direction is magnified to show gouge detail. Figure 53 shows fully developed double gouges at 2500 K, where the leeward gouge, having been the first initiated, is larger than the leading gouge.

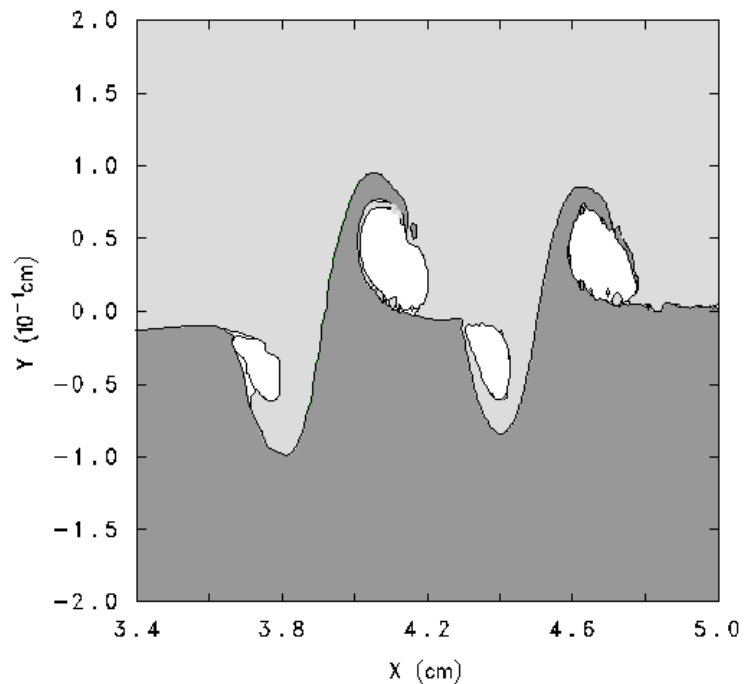


Figure 52. Double Gouge Formation in 1500 K Slipper at 6.0 μ s

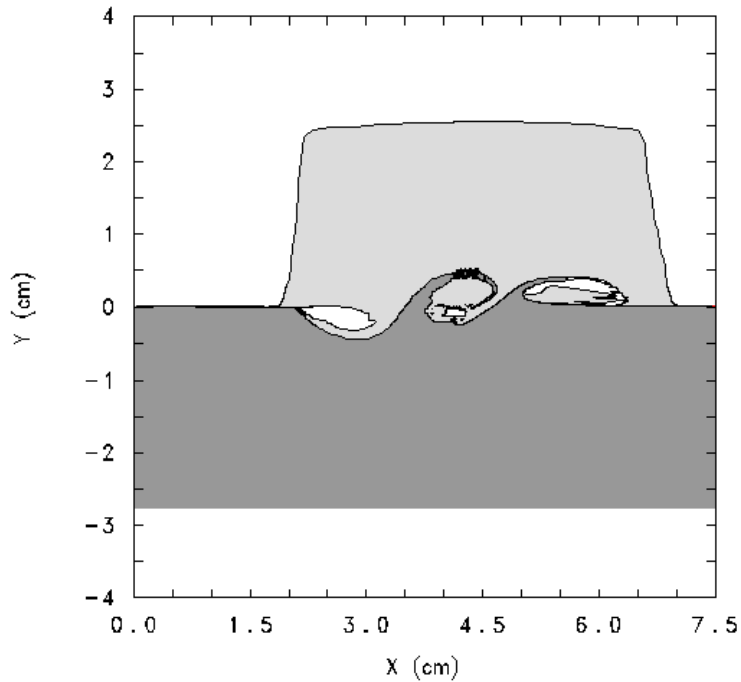


Figure 53. Double Gouges in 2500 K Slipper at 23.0 μ s

Gouging can be described as a surface layer mixing of the two materials. Although fluid like motion and fluid mixing can be seen at low temperatures, it becomes more pronounced as the temperature is increased. Figure 54 shows detail of the slipper/rail mixing at 1500 K caused by a double gouge.

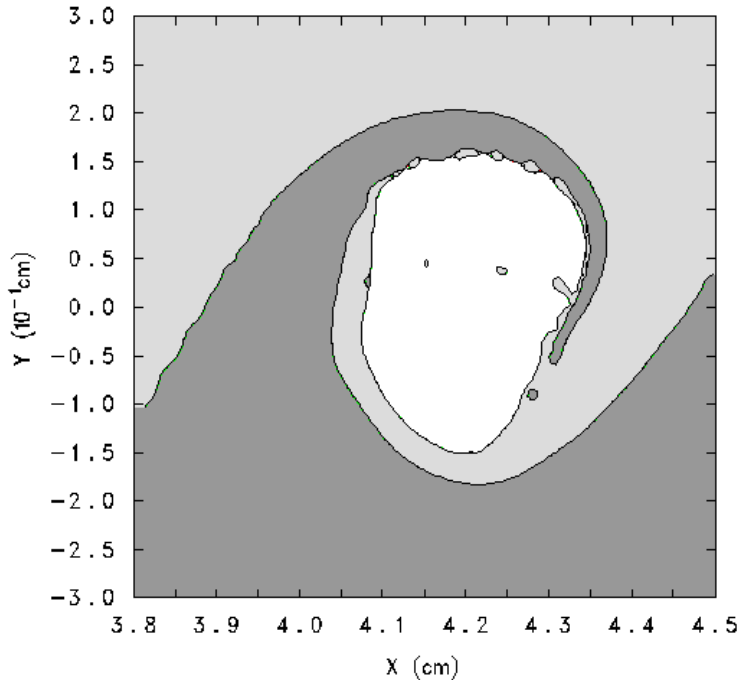


Figure 54. Material Mixing for 1500 K Slipper at 10 μ s

Figure 55 shows a comparison of pressure profiles between the 298 K case and 1000 K case at 8.0 μ s. At 298 K, the high-pressure region is smaller in size, but at about 8 GPa (1160 ksi), it is of a slightly higher magnitude than the 1000 K case. It can also be seen that the higher temperature case has a larger gouge. An interesting point is that the higher temperature has the effect of accelerating the growth of the gouge. At 5.0 μ s, the lower temperature gouge will have a similar size and shape, and will be just starting slipper jet formation as the 1000 K sample has at 4.5 μ s as in Figure 56.

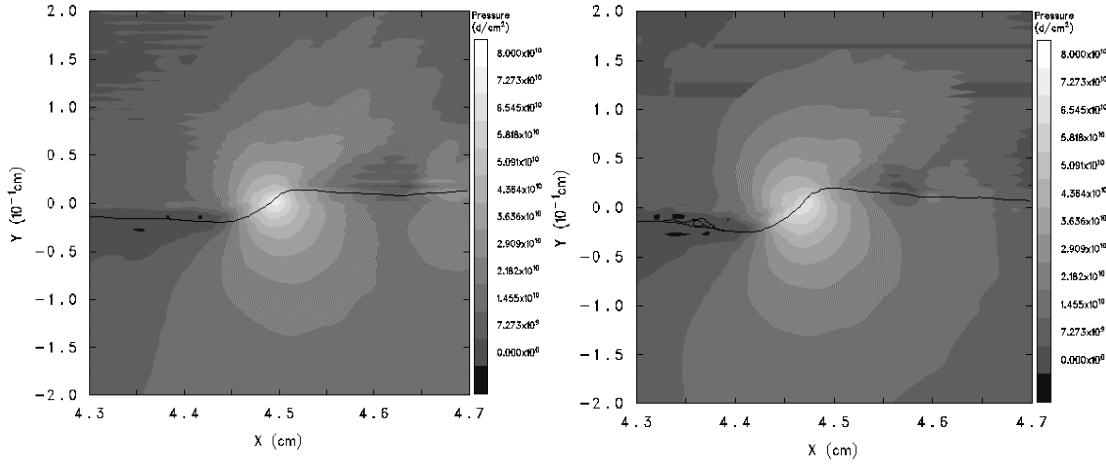


Figure 55. Pressure Profile at $4.5 \mu\text{s}$ for Slider Initially at 298 K (Left) and 1000 K (Right)

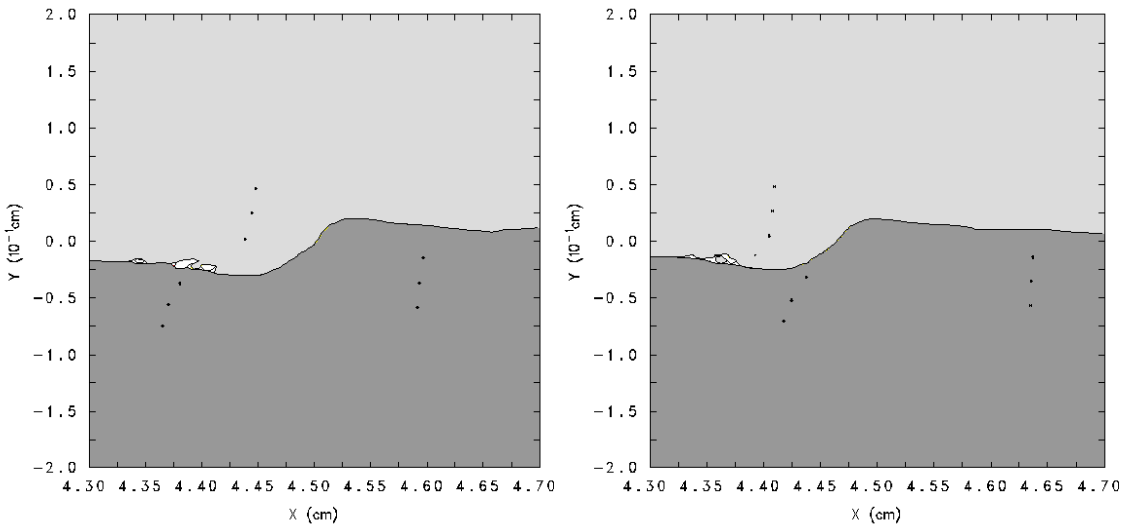


Figure 56. Material Plots for 298 K Slider at $5.0 \mu\text{s}$ (Left) and 1000 K Slider at $4.5 \mu\text{s}$ (Right)

The resulting temperature at $4.5 \mu\text{s}$ for both the 298 K and 1000 K cases is shown in Figure 57. In the 298 K case, all heating is due to shock and strain heating. In the 1000 K case, although the slider is at an elevated temperature, the maximum temperature in each case is similar, about 1500 K (2240°F). Higher temperatures lower the yield stress

of the materials, leading to less resistance to gouging. While the room temperature gouge has reached higher temperatures contributing to weakening of the material, the heated slider provides a jump-start to reaching higher temperatures, leading toward similar behavior and deformation as the unheated case, but at an earlier time.

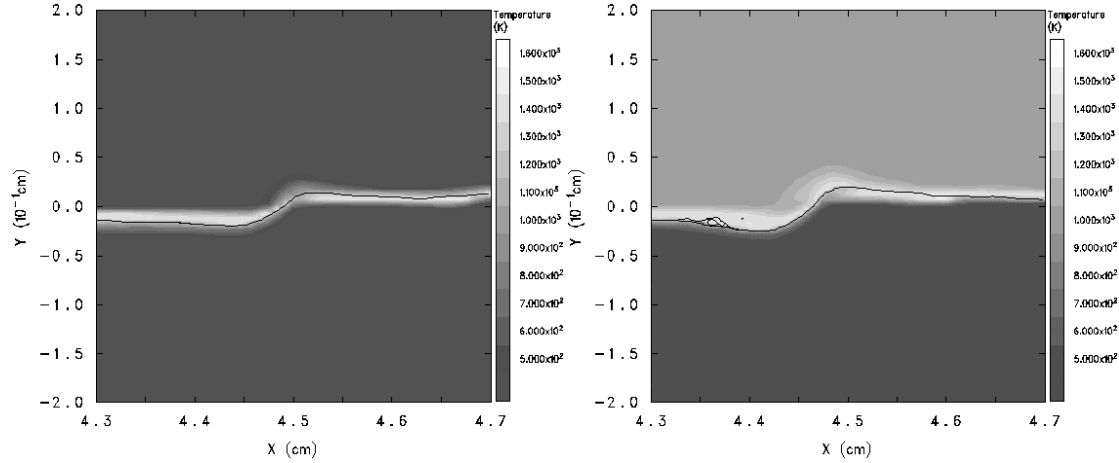


Figure 57. Temperature Profile at 4.5 μ s for Slider Initially at 298 K (Left) and 1000 K (Right)

The effect of the slider temperature on yield stress can be seen in Figure 58. Here, the yield stress of the materials at 4.5 μ s is shown at both 298 K and 1000 K. The materials generally have a higher than normal yield stress because they have been work hardened by the initial plastic stress wave and deformation in the interaction region. While very little difference is seen in the rail, the yield stress of the slider is decreased overall due to the increased temperature, as expected.

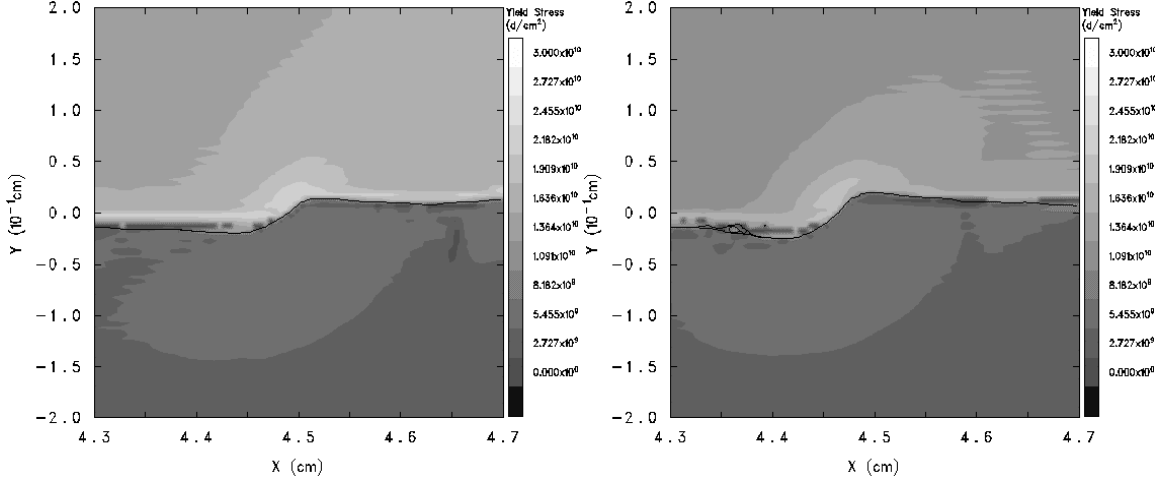


Figure 58. Yield Stress at 4.5 μ s for Slider Initially at 298 K (Left) and 1000 K (Right)

Clearly, elevated slipper temperatures affect the onset and subsequent development of gouging. Even as low as 500 K, the higher temperature aids in the initiation of gouges and accelerates their growth. Above 1500 K, growth is further accelerated, however initiation is delayed.

Slipper Temperature Profiles and Elevated Rail Temperature

To improve upon the sophistication of the temperature environment, a time dependent slipper temperature profile has been implemented as described in Chapter III. In separate simulations, temperature has also been considered in the rail with the time dependent profile in the slipper. Although a rail temperature profile has been calculated in Chapter III, the penetration depth of this profile is less than 0.005 cm. Since the smallest cell size in the model at the interface is also 0.005 cm, one layer of cells at the rail interface is given the source temperature. Expecting elevated temperatures to result in more severe gouging, this results in a worst-case scenario. Because of the high velocity of the slipper,

the rail temperature is considered as a temperature shock. In this case, the source temperature is added to the rail material, but the volume is not changed, representing the fact that the material has not had time to undergo thermal expansion. Before the start of the simulation, the rail has a uniform temperature and density of 298 K and 7.8735 g/cm^3 , respectively, and zero pressure. Introducing the source temperature at $t = 0$, the density has not yet been able to respond and is at its original value. Since T and ρ are thus defined, the equation of state dictates that pressure is now also defined and is nonzero. As a result, the rail surface begins the simulation under high pressure and expands rapidly.

At 500 K, there is very little difference between the three cases of uniform slipper, time dependent slipper profile, and slipper profile with rail temperature, as shown in Figure 59. At 1000 K, there is also no change, and at 1500 K and 2000 K, results for all three cases are still very similar. This indicates that the use of a temperature profile does not affect gouge development below 2000 K, and that only the conditions within 0.1 cm of the surface significantly affects the gouge. But these results also show that the rail temperature, confined to within 0.005 cm of the surface did not have any effect. Either the layer was too thin to influence events, or altering the rail at this point does not change anything. Gouging involves interaction and mixing between two materials. Because gouging is dependent on the plasticity of both materials, if one material has conditions or properties that prevent it from participating in gouging, gouging will not occur, even if the other material has conditions or properties that allow it to gouge. In this case, it may be that the slipper is the material most resistant to gouging, so creating conditions that make the rail more susceptible (such as heating it), makes little or no difference.

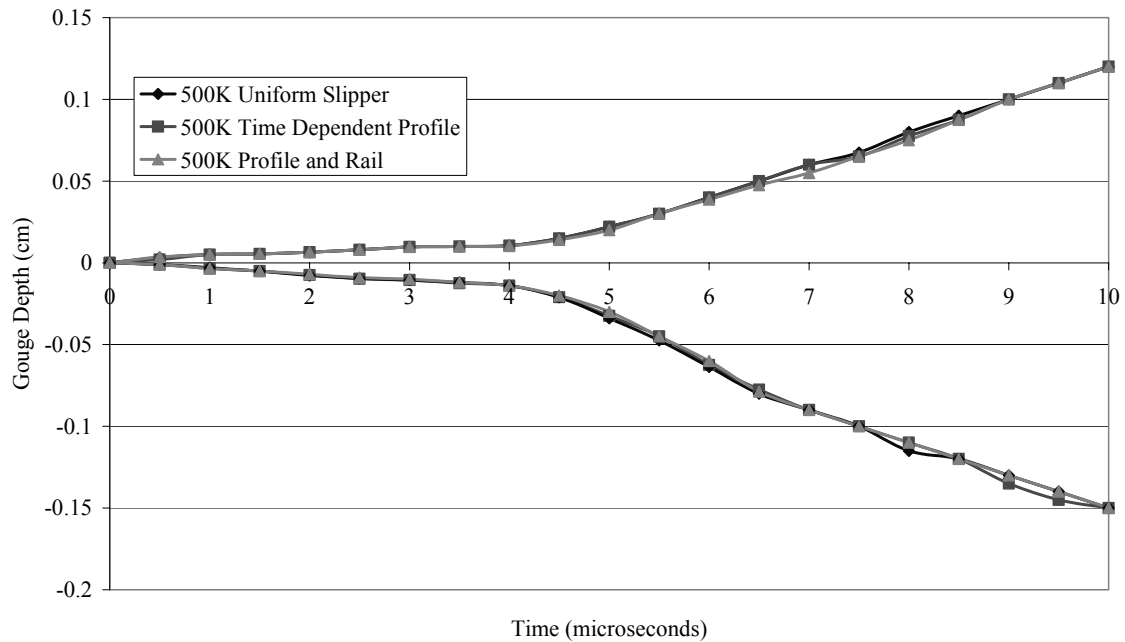


Figure 59. Maximum Gouge Depth Vs. Time for 500 K Source Temperature

At 2500 K, the situation is markedly different. All three temperature environments produced different results. Using the temperature profile in the slipper caused gouging to initiate a microsecond sooner than the uniform slipper, as shown in Figure 60. At this temperature, the slipper material has melted. In the case of the slipper profile, only the surface is melted while the interior is still solid.

Using the slipper profile in conjunction with the rail temperature resulted in immediate gouging. This is primarily due to the fact that at 2500 K, the pressure in the rail is so great that it causes the rail to rise upward so much and so rapidly that the slipper impacts this part of the rail horizontally, as in the asperity impact to be described later. In asperity impacts, gouging initiates immediately.

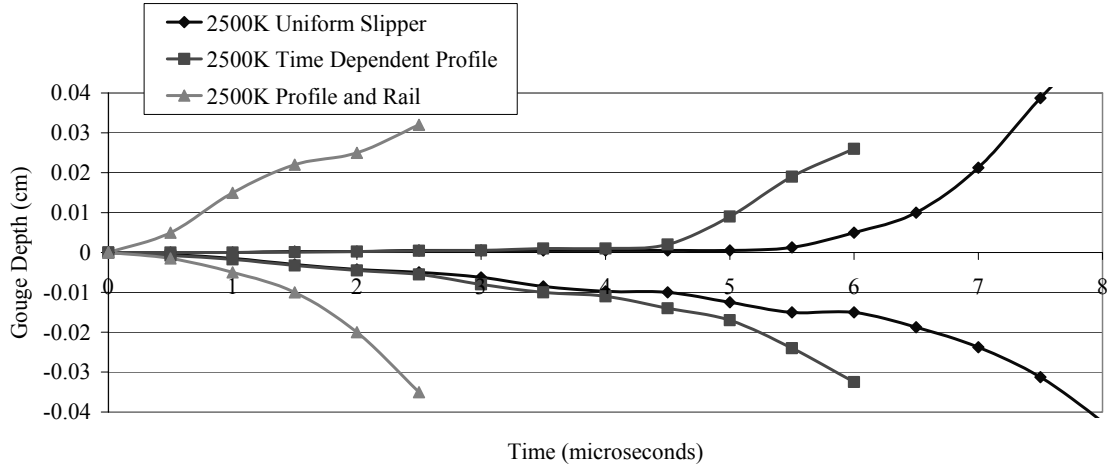


Figure 60. Maximum Gouge Depth Vs. Time for Different Thermal Environments with a 2500 K Source Strength

Asperity Impacts

The asperity model consists of a two dimensional rail, slider, and a small object called the asperity as shown in Figure 61. In this case, the slider is moving from left to right across the rail, and has no vertical velocity component. An impact event is generated when the slider collides with the asperity. The rounded edge of the slider drives the asperity downward into the rail, resulting in both horizontal and vertical impact forces. Because the asperity model has been used in previous simulations using CTH [19, 22], it was also used in these studies to compare results. The asperity model is used because it has been found that an impact event is necessary to initiate gouging; it will not occur due to sliding alone. The asperity is a simple way to initiate an impact between the slider and the rail without having to consider vertical momentum effects. In this way, the time

varying sled mass and vertical velocity need not be known nor considered. This model also has a reduced computational time versus the oblique impact case.

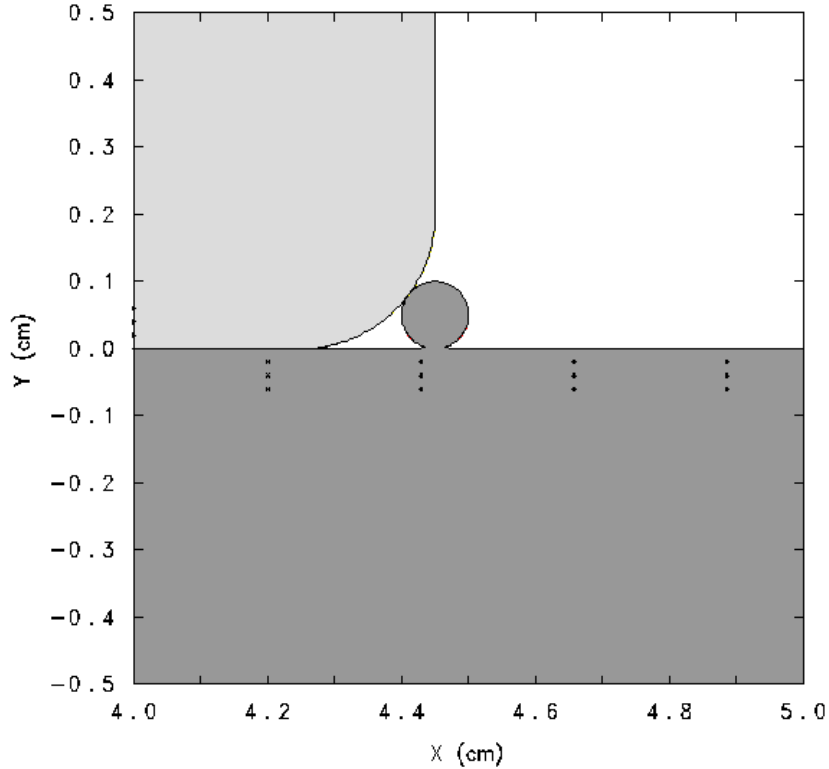


Figure 61. Asperity Impact Model

In numerical work, it is always important to maintain ties to the real work by comparing numerical results to real results. In gouging, experimental results for known initial conditions are rare and only consist of whether or not a gouge occurred at these conditions, and what the gouge looks like. No experimental information on the actual development of gouging is known. Another important reason to consider the asperity impact is to compare it to the previous work of Schmitz [82]. Schmitz tuned the angle of the slider leading edge such that velocity at which gouging initiates in CTH matches

experimental data (Figure 62), providing some correlation between simulated asperity impacts to experimental results.

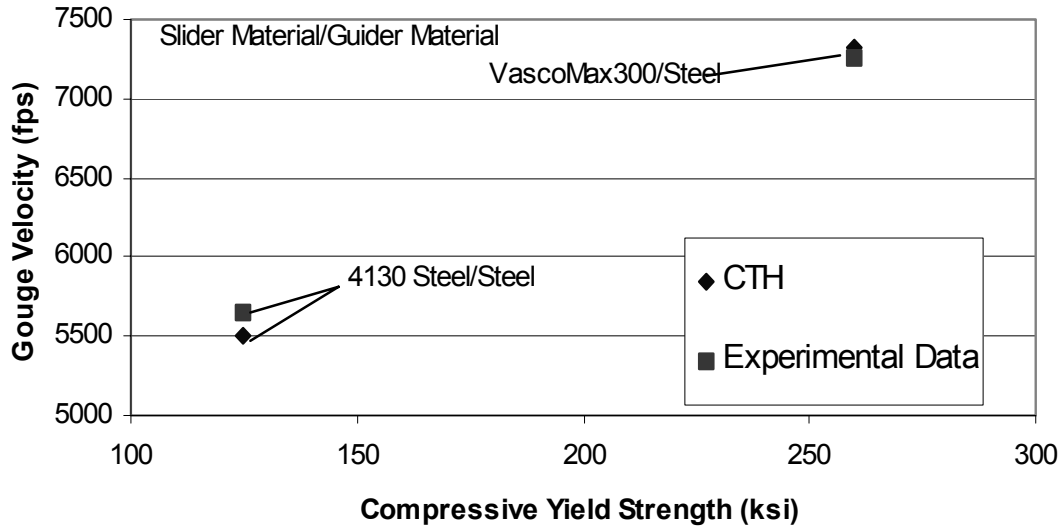


Figure 62. Correlation of CTH Results to Experimental Data [22]

Another useful purpose for asperity modeling is to understand why in three cases relatively large transverse asperities did not cause rail gouging but tended to reduce gouging in two of the cases. In 1968, Gerstle [7] purposely placed a weld bead across a railhead and the slipper contacted the bead but did not gouge. In Tarcza's study [17], a manufactured rise across the lead target again did not trigger gouging and reduced gouging downstream. Finally, web-bearing slippers that slide over raised lettering do not initiate gouges when sliding across the letters.

First using an asperity 0.1 cm in diameter, the rail again experiences gouging, and the size and shape of the gouge is very similar to that of an oblique impact. Comparing the two impact cases, it is evident that the impact event and phenomena that lead to gouging

are somewhat independent of the cause or method of impact. In the asperity impact, however, the remains of the asperity come into play, and alter the contact surface in a way not seen in the oblique impact. Furthermore, it is difficult to directly compare the damage because in an asperity based impact, the damage is associated with the angle of the slider's leading edge, whereas in the oblique impact, damage is associated with the vertical velocity and inertial forces. These differences complicate comparison between the results of the two scenarios.

The primary difference between oblique and asperity impacts is that in an asperity impact, there is a horizontal component of impact immediately; it does not need to be built up by penetration or humps. In this case then, the material jetting initiates immediately upon impact, as seen in Figure 63 at 1.0 μ s.

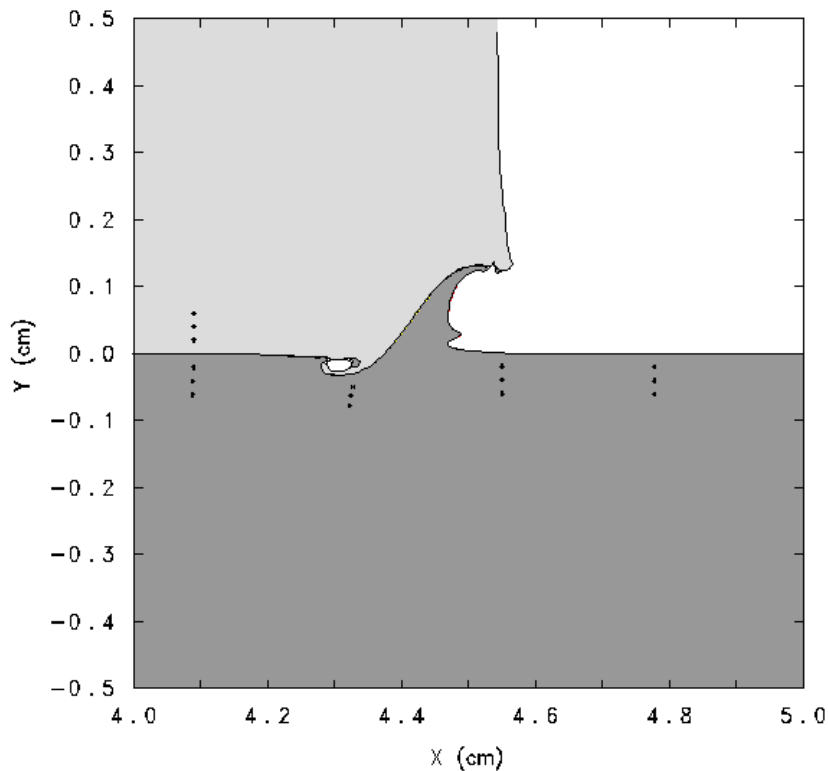


Figure 63. Material Deformation from 0.1 cm Asperity Impact at 1.0 μ s

By 5.0 μ s, there are few indications that the event is any different than the oblique impact studied previously (Figure 64).

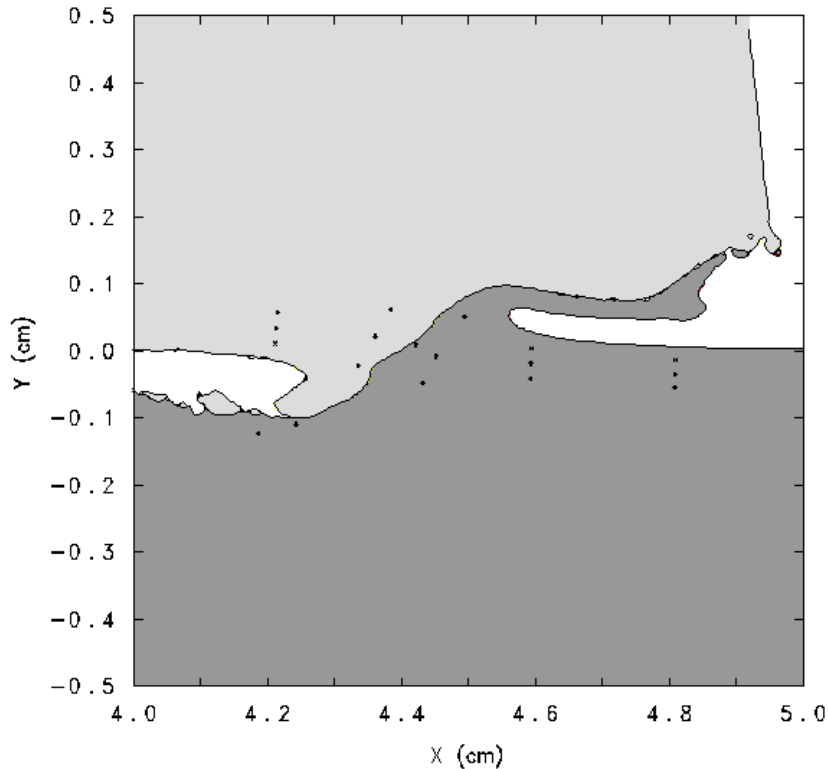


Figure 64. Material Deformation from 0.1 Asperity Impact at 5.0 μ s

Figure 65 compares the resulting gouges of the two discussed impact scenarios after 24 μ s. After this time, both gouges are not quite fully developed at the leading edge, but are clear enough to discuss. Both gouges have the characteristics of gouges seen in real life: they are slightly deeper toward the leading edge, have raised leading edges, rough bottom surfaces, and slipper material can be found embedded in the rail and vice versa. While not identical, the very different impact scenarios both produced gouges of similar size and shape, and both appeared to develop through the same interaction mechanisms.

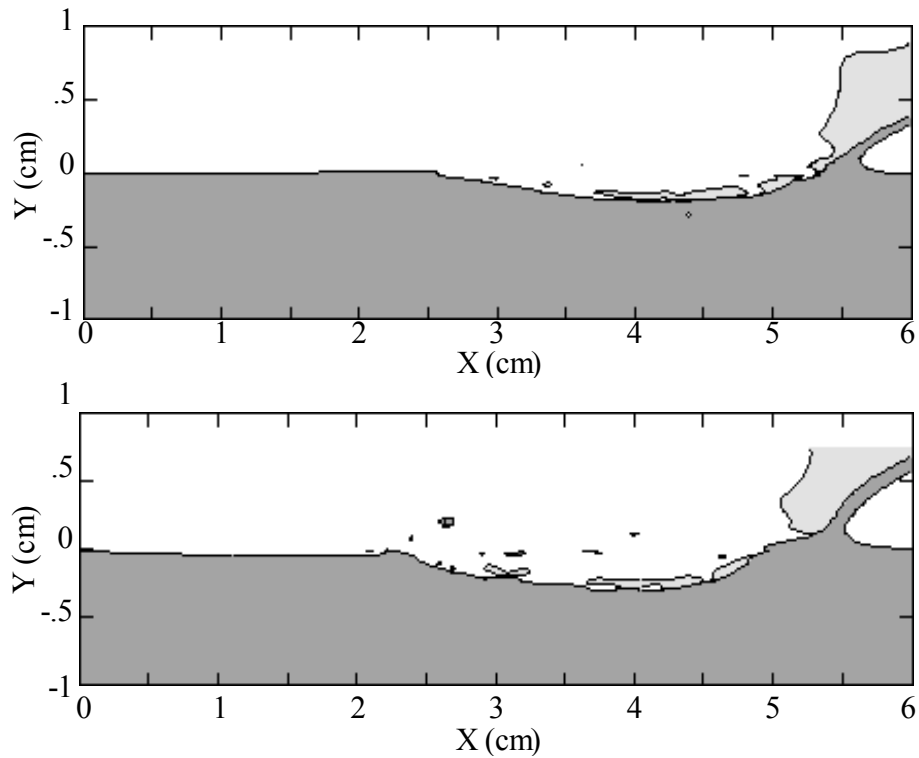


Figure 65. Resulting Gouge After Asperity Impact (Top) and Oblique Impact (Bottom)

In an asperity impact, the stress wave due to impact is centered on the asperity rather than the material interface, and moves outward from that point radially. Again, the wave front itself does not appear to play an important role in formation of the gouge. As in the oblique impact, a high-pressure core is centered on the interaction region. However, this time this area of high pressure is generated immediately and does not occur with time, although it does grow with time.

Also examining asperity sizes of 0.02 and 0.5 cm diameters, it was found that the 0.02 cm diameter asperity did not result in a gouge. The impact was not sufficient to cause jet formation. The 0.5 cm asperity resulted in a massive gouge, the initiation of which is

shown in Figure 66. This result is contrary to the observation-based belief that large asperities actually inhibit the formation of gouges.

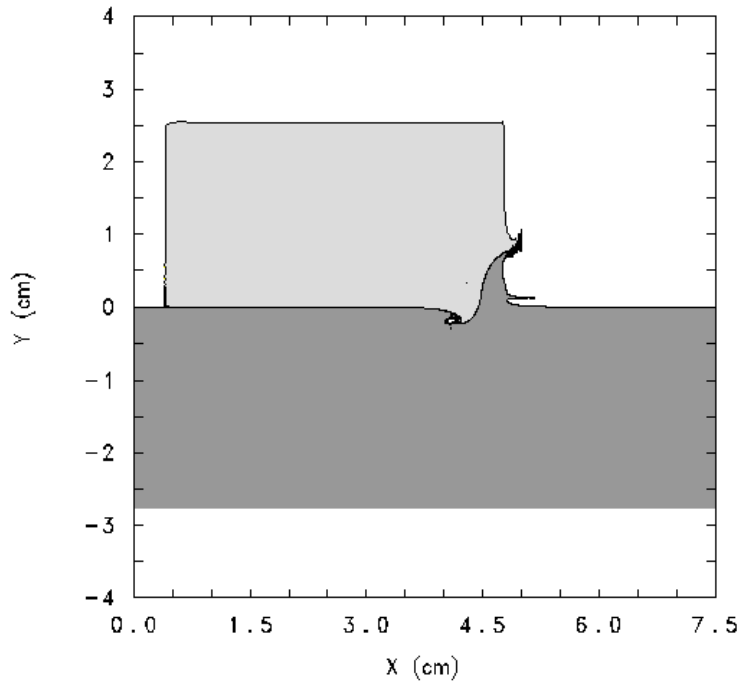


Figure 66. Gouge Initiation Due to 0.5 cm Diameter Asperity

To compare the development of the asperity gouges, maximum gouge depth versus time has been charted in Figure 67. Maximum gouge depth into the slipper has been omitted for clarity. Here it can be seen that both asperity gouges initiated immediately, and that the large asperity had a rapid initial growth rate that is slowing with time, rather than the linear rate seen in the first 10 μ s for the oblique impact.

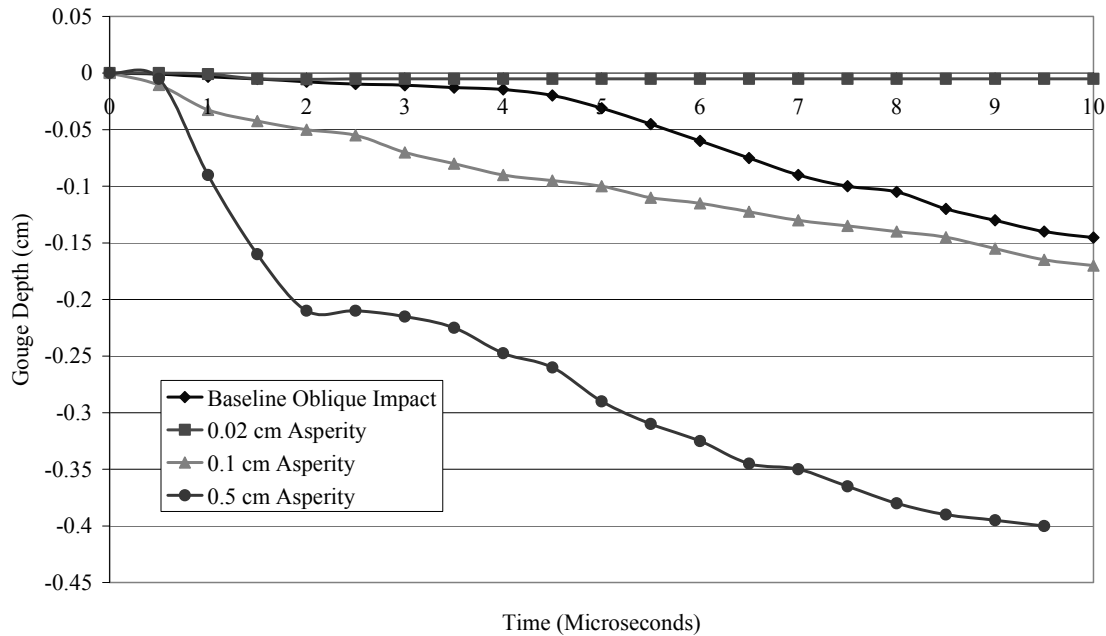


Figure 67. Maximum Gouge Depth Vs. Time for Asperity Impacts

Horizontal Velocity

Sled velocity is the most significant factor in the development of gouging. For this reason, horizontal velocities of 1, 2, and 3 km/s were examined to determine the effect of velocity on gouging. At higher velocities, impact forces will be greater, strain and strain rates will be higher, and temperature due to plastic strain is expected to be higher.

At 1 km/s, the slider did not gouge, but its penetration into the rail pushed enough rail material in front of it to produce damage similar to a gouge. In this case, a hump of rail material formed in front of the slider, but was not over run by the slider. As the penetration of the slider into the rail increases, the amount of rail displaced into the hump also increases, and a jet of rail material is formed. But by 24 μ s, no jetting has

occurred in the slipper (Figure 68). Because of the lack of the slipper jet, the interaction is not unstable, and therefore the damage is not characterized as gouging.

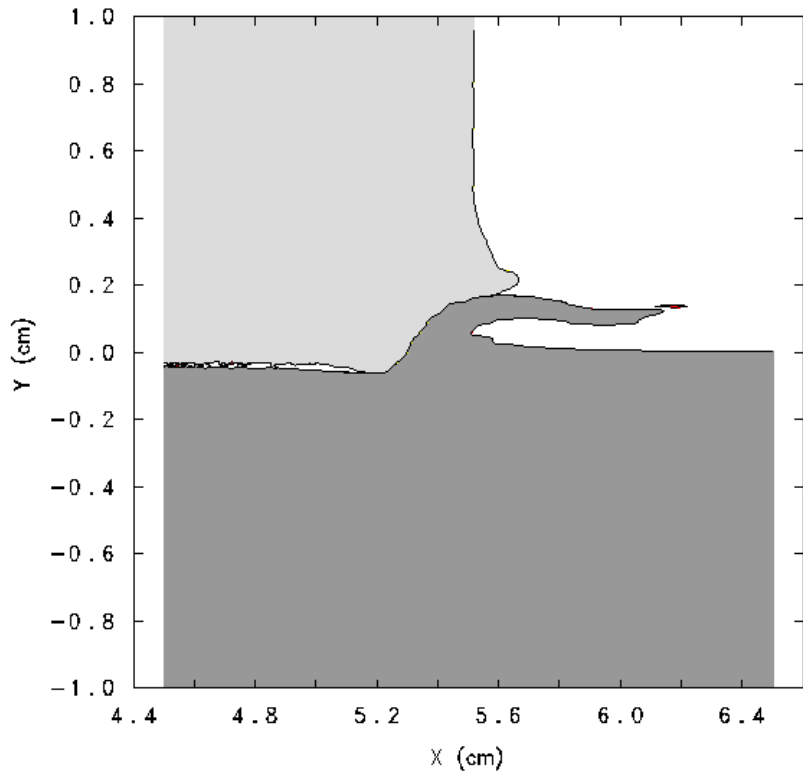


Figure 68. Rail Damage at 24 μ s Due to 1 km/s Oblique Impact

As expected, increasing the horizontal velocity to 3 km/s caused jetting to occur sooner, and resulted in a higher rate of growth. Figure 69 shows the growth of the gouges at various velocities.

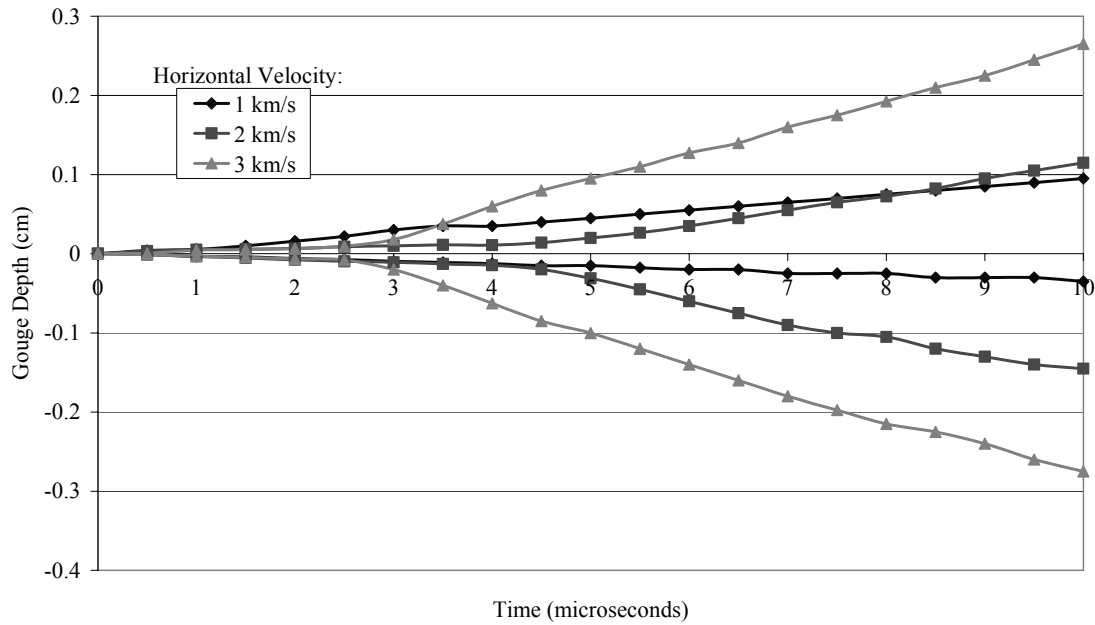


Figure 69. Maximum Gouge Depth Vs. Time for Various Horizontal Velocities

Vertical Velocity

The vertical velocity of the slipper may be an important factor in gouging.

Considering the oblique impact, the vertical velocity will dictate the strength of the initial stress wave and more importantly the depth of slipper penetration. Vertical impact velocities of 25, 50, and 100 m/s have been examined. Between 25 and 50 m/s, the higher vertical velocity caused jetting to initiate sooner and resulted in a higher growth rate of the gouge (Figure 70). Jetting occurred at about the same penetration depth for both, between 0.015 and 0.020 cm. Increasing to 100 m/s did not result in faster initiation, but gave further increases in growth rate.

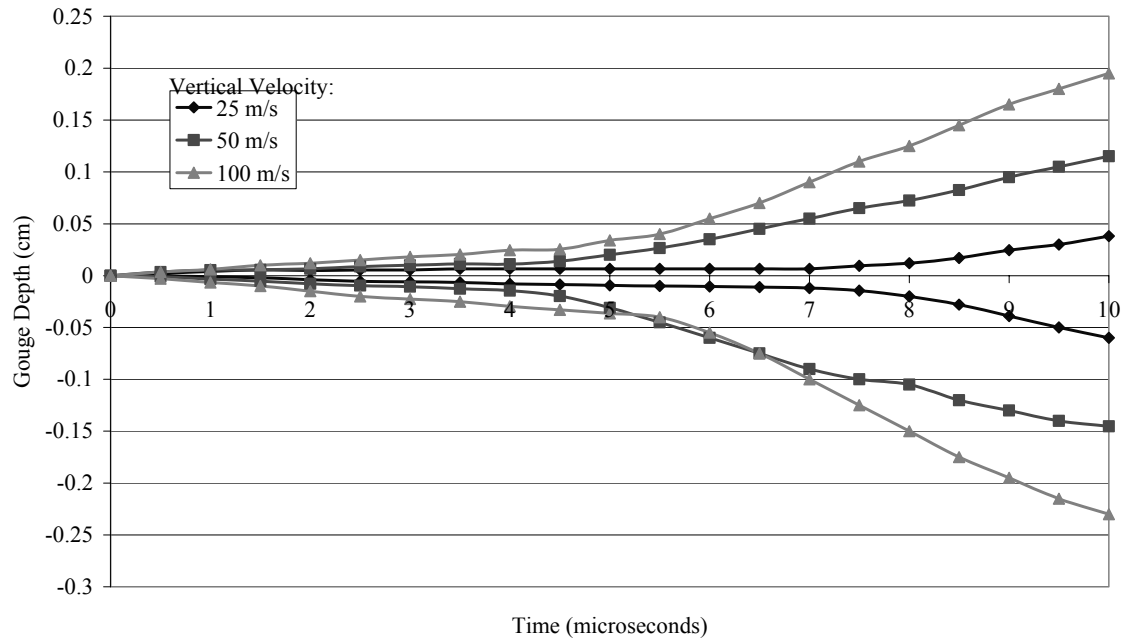


Figure 70. Maximum Gouge Depth Vs. Time For Various Vertical Impact Velocities

Geometry

Since shock wave propagation is effected by geometry, it is appropriate to vary the geometry and examine how differences in shock wave propagation effect the development of gouging. During this investigation, it was found that the angle of the slipper leading edge can play an important role. The first model studied was a small slipper with angle leading edge identical to that used by Schmitz et al [82] shown in Figure 71.

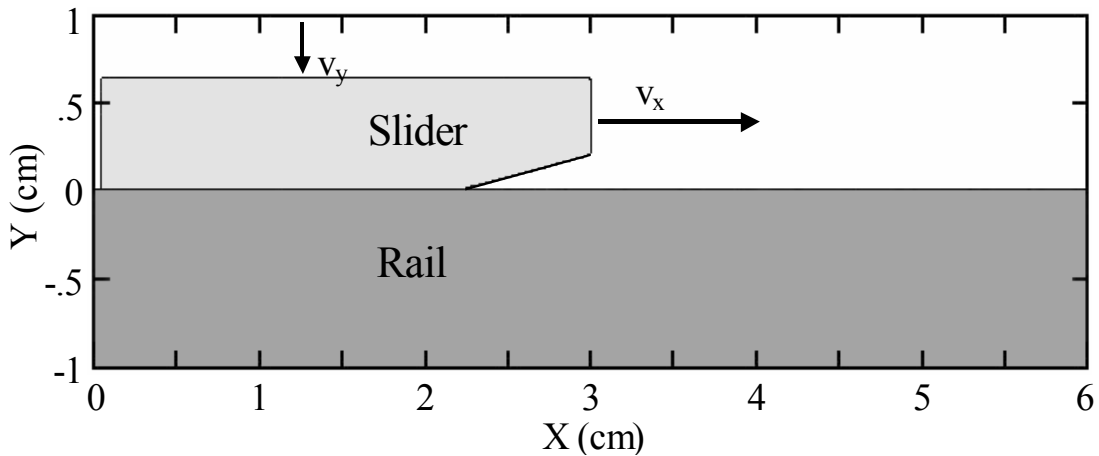


Figure 71. Small Geometry Oblique Impact Model

Using the small geometry, no gouge was created. Rail penetration vs. time for this case is compared with the baseline gouge in Figure 72. Penetration for the small geometry is nearly as deep as the baseline case before jetting occurred in the baseline. Considering stress wave propagation, the stress wave reflects off the top of the slider by 1.0 μ s. After reflection, the wave is a rarefaction wave that relieves the stress imparted by the first pass. This reflected wave arrives back at the gouge area by 2.0 μ s, well before jet formation would be expected.

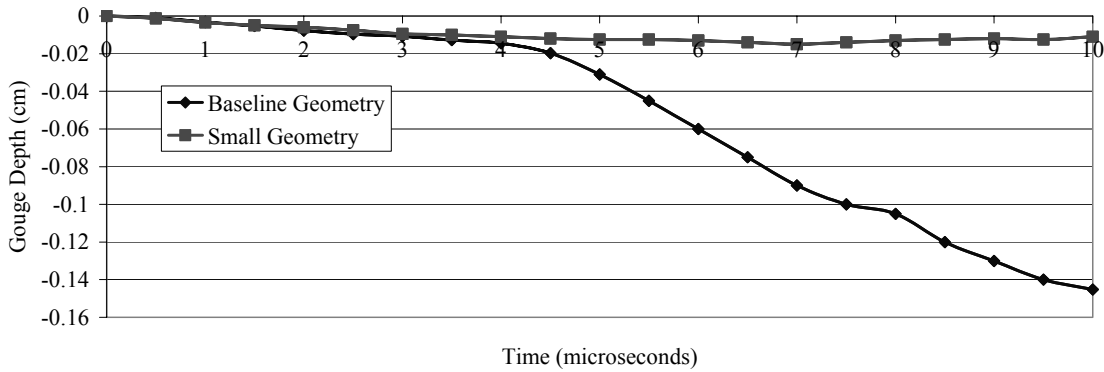


Figure 72. Maximum Gouge Depth Vs. Time for Small Geometry Slider

The fact the gouging did not occur in this case invites the following question: is the prevention of gouge formation due to the earlier stress wave reflection, the reduced mass, or the different leading edge geometry? To examine the effect of the wave propagation, a slipper model was developed with similar mass and leading edge geometry to the baseline model, but with the same thickness (0.64 cm) as the small geometry model, resulting in similar wave reflection properties. In this case, gouging still occurred. Next, a slipper model was devised with similar thickness and mass as the small geometry model, but with the rounded leading edge geometry of the baseline slipper. In this case, gouging again occurred, and the only remaining variable is the leading edge geometry.

To explore the effect of the leading edge geometry, four slipper models were created with similar size and mass as the baseline case, but with various angles of leading edge geometries. These include 14.036° (similar to the small geometry leading edge in Figure 71), 3.576° , 1.790° , and 0.787° leading edge angles, measured from the rail surface.

In these cases, the 14.036° case had little effect, but the 3.576° resulted in a delay in gouge onset until $10 \mu\text{s}$. Further reductions in leading edge angle eliminated gouging all together. These results are summarized in Table 3 below.

Table 3. Gouging Characteristics of Various Leading Edge Geometries

Leading Edge Angle	Gouge
14.036°	yes, $5 \mu\text{s}$
3.576°	yes, $10 \mu\text{s}$
1.790°	no
0.787°	no

While the maximum penetration depth for the angled leading edge simulations were similar to the baseline impact different cases, the shallow leading edge resulted in a shallow slope at the material interface, inhibiting the initiation of material jets as in the center portion of Figure 48. Thus, the slipper geometry is a factor that affects the tendency to gouge, and lowering the angle of material interface with respect to the velocity vector by changing the slipper geometry inhibits the development of gouging.

Increased Rail Yield Stress

In the results presented to this point, the rail has been modeled as iron with a yield stress of 0.175 GPa. However, the test track is constructed of 1080 steel, which has a yield stress close to 0.7 GPa. By using this yield stress in the numerical model, perhaps a more realistic test track scenario can be created. All other factors held the same as in the baseline case; use of this yield stress did not result in gouging. It is interesting to notice, however, that the increased yield stress did not inhibit the penetration of the slipper into the rail. Figure 73 compares the penetration depth of this case to that with no horizontal velocity using the original rail yield stress. It is seen that the amount of penetration is identical.

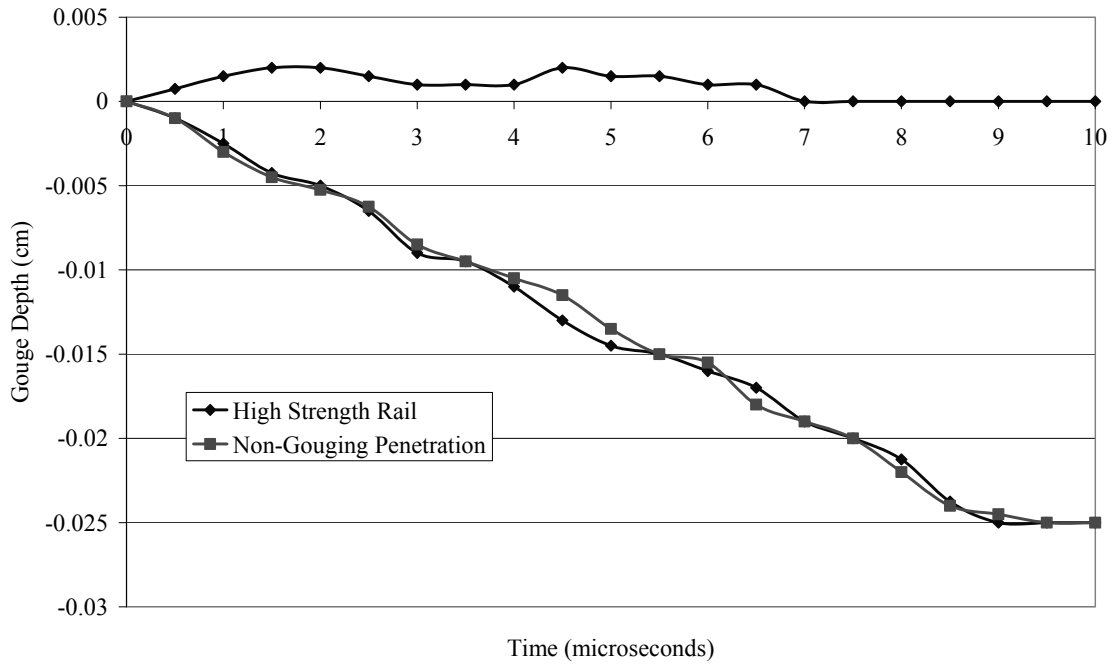


Figure 73. Maximum Gouge Depth Vs. Time for High Yield Stress Slipper

Rate Dependent Slipper

In Chapter III, the importance of a strain-rate dependent constitutive model was discussed. However, in these simulations, a rate independent model was invoked for the slipper because of the lack of Steinberg-Guinan-Lund model rate dependent material constants for the VascoMax steel. This is considered to be acceptable because while yield stress increases with strain rate, this behavior is not without limit. At stresses approaching 10 GPa, and strain rates greater than 10^5 s^{-1} , additional strain-rate effects become insignificant [47]. The gouging phenomenon is near this regime, if not a little low. To test the validity of rate independence, the rate dependent constants known for 4340 RC 38 Steel where inserted into the VascoMax model:

$$C_1 = 3.1 \times 10^6 \text{ 1/s}$$

$$C_2 = 2.4 \times 10^4 \frac{\text{g}}{\text{cm} \cdot \text{s}}$$

$$U_K = 0.31 \text{ eV}$$

$$Y_P = 7.0 \times 10^9 \frac{\text{g}}{\text{cm} \cdot \text{s}^2}$$

$$Y_A = 1.0 \times 10^{10} \frac{\text{g}}{\text{cm} \cdot \text{s}^2}$$

$$Y_{max} = 2.5 \times 10^{10} \frac{\text{g}}{\text{cm} \cdot \text{s}^2}$$

Figure 74 displays the maximum gouge depth versus time for both the rate dependent and rate independent slipper models. The time and depth that jetting develops is identical, as are the growth rates. In all, the use of the rate dependent model makes very little difference in this case.

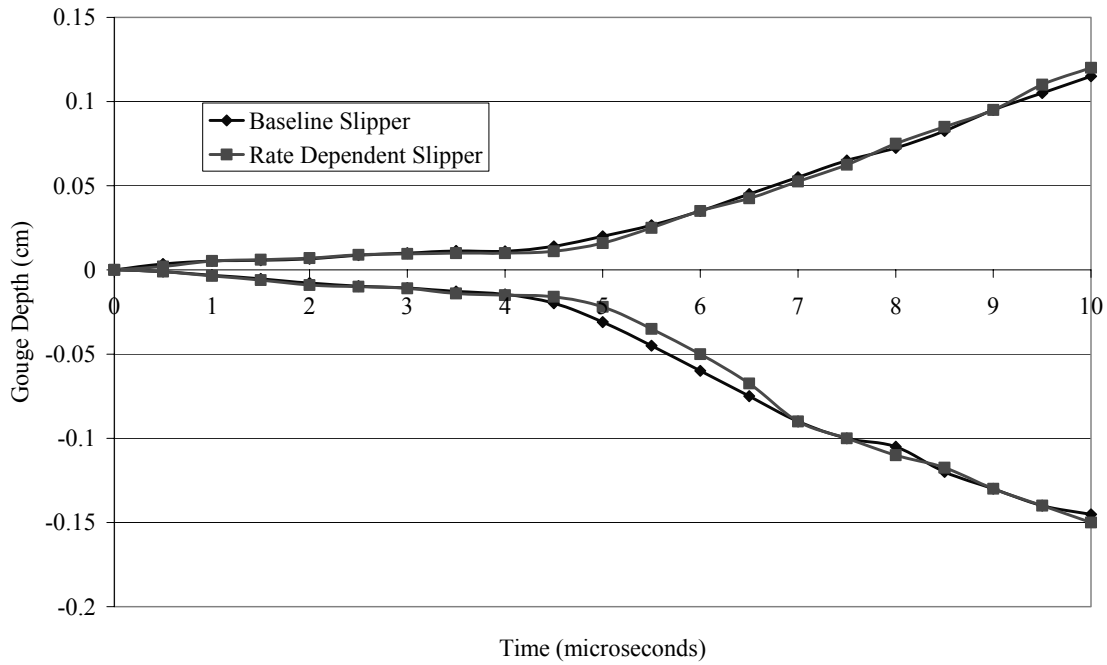


Figure 74. Maximum Gouge Depth Vs. Time for Rate Dependent Slipper Model

Parallel Plate Models

In the results thus far, it appears that the most important factor leading to gouging is the introduction of a horizontal component of impact that will lead to the formation of material jets. A parallel plate impact model was developed. Two parallel plates moving in opposite directions with a pre-described deformation as shown in Figure 75. The pre-described deformation acts like an asperity, with an initial source of horizontal impact. As expected, this scenario immediately results in material jetting and unstable growth of a gouge (Figure 76).

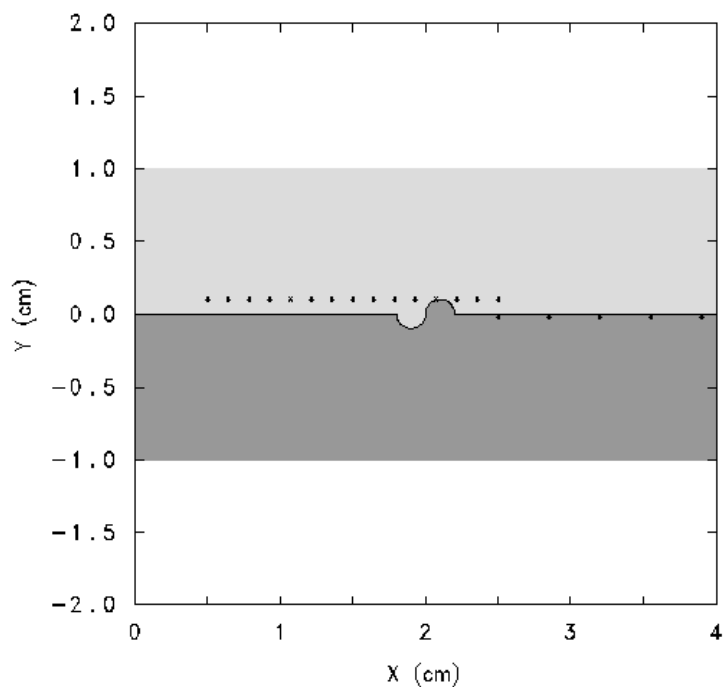


Figure 75. Parallel Plate Model with Pre-Described Deformation

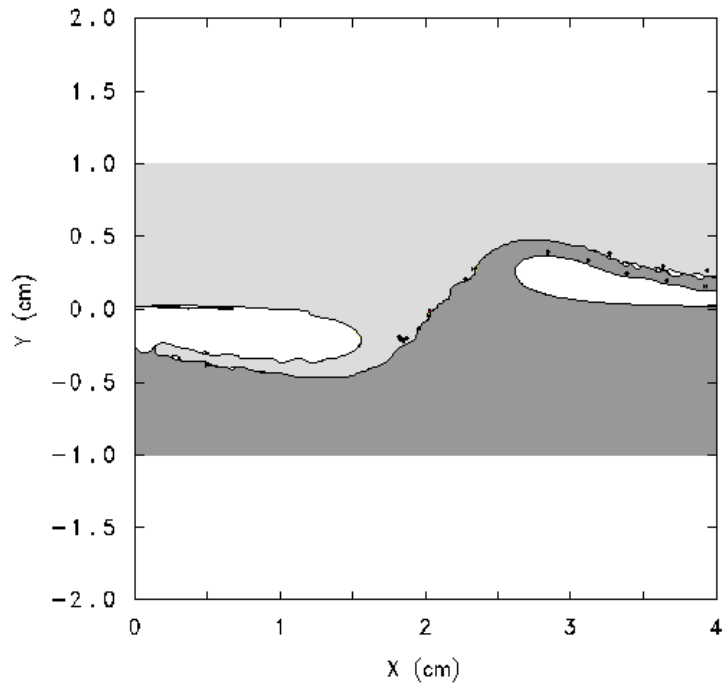


Figure 76. Resultant Gouge Due to Pre-Described Deformation

As a variation of the oblique impact, a case was developed where the two plates do not have a pre-described deformation, but do have vertical impact components in addition to the horizontal velocity. In this case, gouging could not be initiated, even at impact velocities resulting in pressures up to 20 GPa. This indicates that hypervelocity sliding accompanied by vertical forces cannot result in gouging by itself. A “front” of one material is needed to provide a leading edge of penetration, or a location of horizontal impact. The parallel plate model with no deformation cannot result in a horizontal impact component, at least computationally where the surfaces are perfectly smooth.

Three Dimensional Model

All of the simulations presented to this point have been two-dimensional plane strain problems. But it would be encouraging to know if plane strain provides an accurate representation of what really occurs. To be sure, a study has also been carried out on a three dimensional model.

In development of the model, one should consider the physical realities of rail and slipper contact. The plane strain model behaves as would the impact of the two bodies with infinite dimensions in the z -direction. In transitioning to a three dimensional model, one might first think of the problem of a brick impacting a rail, each with a four inch z -dimension, thus simulating perfect parallel contact between the top surface of the rail and the largest inner surface of the slipper. However, it should be remembered that the sides and the bottoms of the rail and slipper interface also form flat, parallel surfaces, but of much smaller area, thus having different loading characteristics. Furthermore, because of the gap present between the rail and slipper, the slipper may undergo roll, pitch, and yaw

that detract from parallel surface impact. Any perturbation of one axis of the slider from being parallel to the rail will result in an edge impact on a rail surface, and perturbation of two or more axes will result in a point impact at one of the railhead corners as drawn in Figure 77. Because of slider movement, this corner impact scenario is the most likely case, and this idea is reinforced by the fact that many more gouges occur at the corners than on the flat surfaces [11].

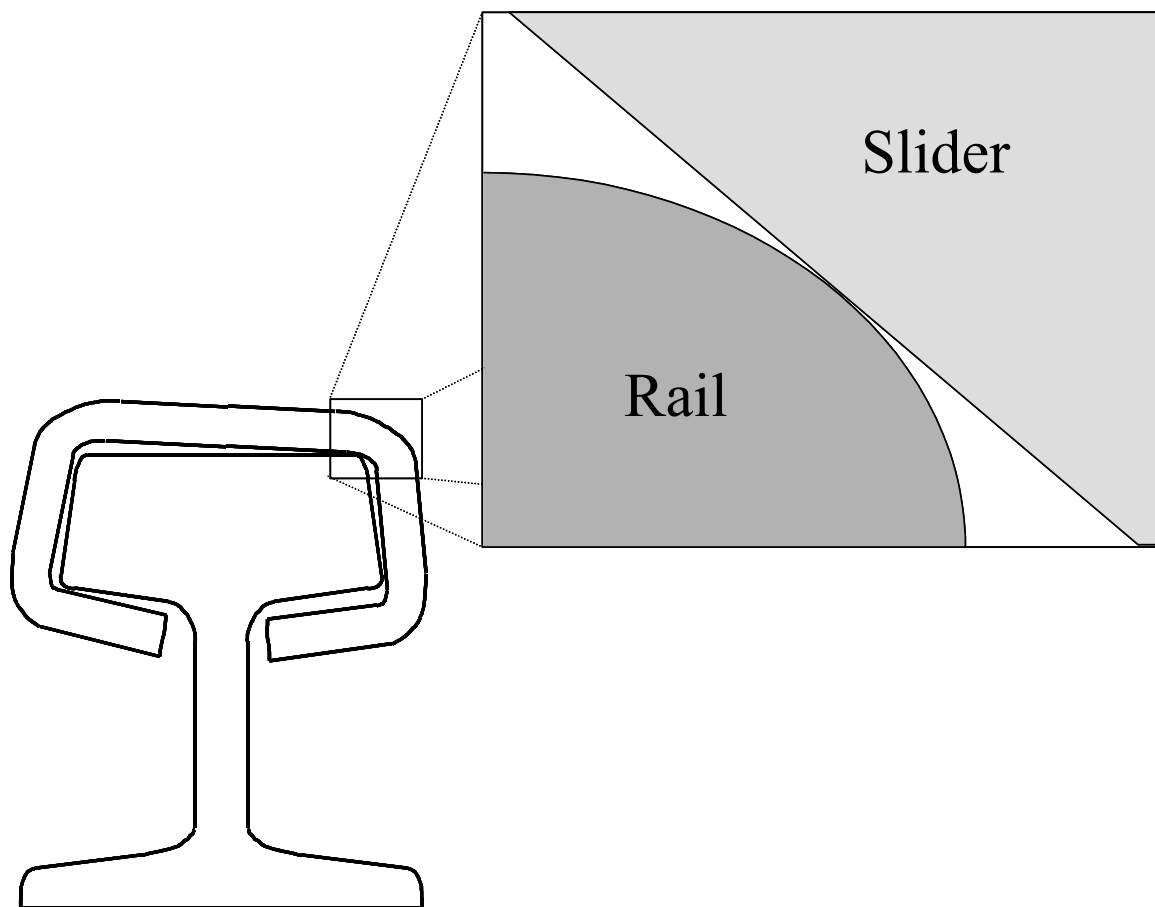


Figure 77. Slider Corner Contact

Due to this localized impact, one would expect higher stresses to occur in the impact area. This difference in the stress distribution and the curved nature of the rail corners may present a challenge to the validity of the plane-strain model. The three-dimensional model uses the same x - y geometry and other conditions as the baseline oblique impact. The model is axisymmetric about $z = 0$ (the rail center) and the z -axis extends 2 cm from the rail center. The grid size in the z -direction is also similar to the x - y grid. A close up view of the y - z profile is shown in Figure 78, and is based on actual rail geometry. This geometry results in a line contact between the slipper and rail in the x -direction.

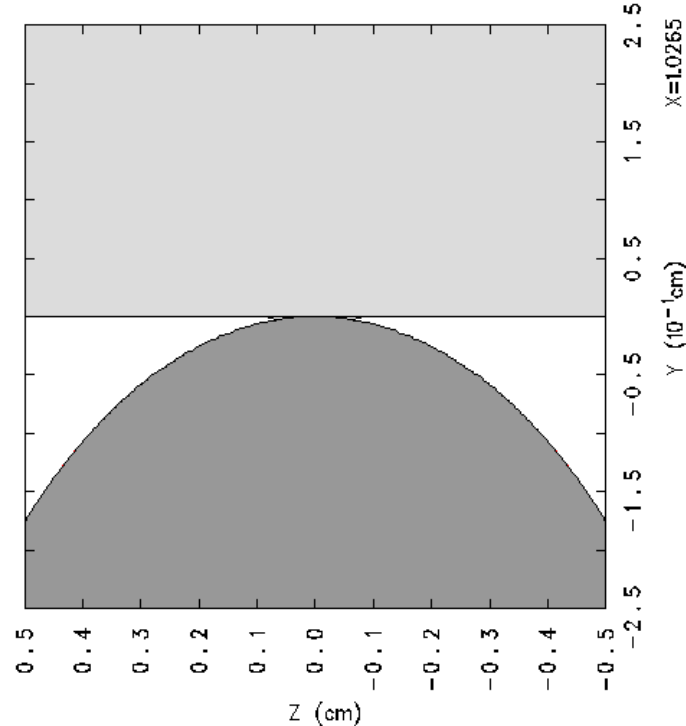


Figure 78. Three-Dimensional Oblique Impact Model

Rather than the higher stresses and faster initiation that was expected, it was found that although the developing physical characteristics were similar, three-dimensional gouging actually delayed the development of gouging with respect to time. Figure 79 shows the three-dimensional gouge after 11.0 μ s, where it is comparable to the baseline gouge at 6.5 μ s. This is most likely the result of the fact that there is a gap between the two materials to the sides of the centerline, making the interaction region smaller, and providing a space for displaced rail material to flow or jet without impinging on the opposite surface.

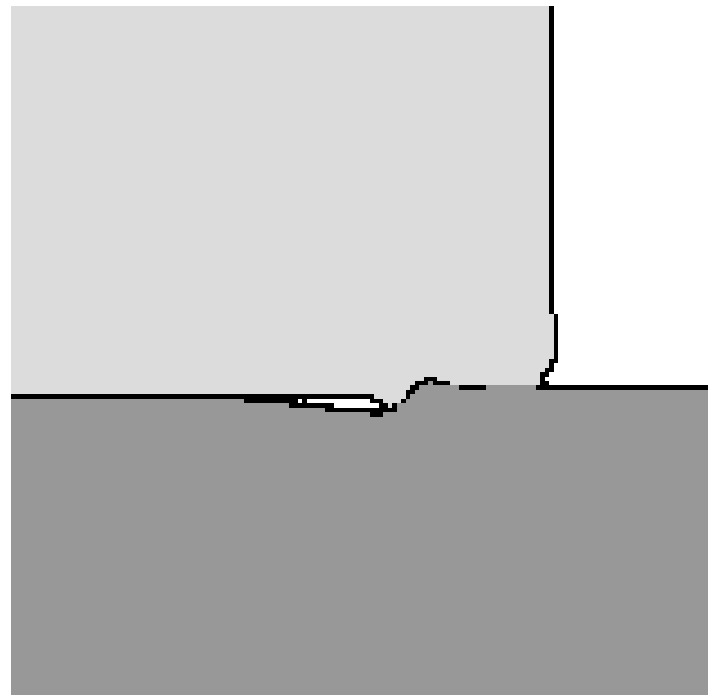


Figure 79. Development of Three-Dimensional Gouge at 11 μ s

The three-dimensional results validate that the two-dimensional plane strain model is adequate in terms of modeling material flow and gouging characteristics, but that the timing of these events may be a few microseconds off.

Mixed Eulerian Cell Treatment

As mentioned previously, CTH has several different options to handle multi-material cells. In the method used for the previous calculations, the model defines the yield stress in a mixed material cell as the sum of the volume fraction weighted yield stresses of the individual materials. Single material cells with voids have a decreased yield stress because the volume fraction of the material is less than one. This results in the materials being one piece, and they cannot move independently.

Another model is similar except that the yield stress of all cells is divided by the sum of the volume fractions of the materials that can support shear. Now single material cells with voids have the yield stress of the material.

The last model sets the cell yield stress to zero in mixed cells except for the case of a cell containing one material plus void. In this case a volume-weighted average is used, as in the first model. This allows the materials to move as separate, unattached entities, but also results in the impact being frictionless. This model is generally the preferred option when modeling frictionless interfaces when the boundary layer algorithm is not used.

Figure 80 shows the maximum gouge depth versus time for these three models. The first two, referred to here as mix 1 and mix 3, produce nearly identical results. The last model, called mix 5, results in jet formation that occurs about 0.5 μ s sooner, but a slightly

lower growth rate. Although these factors have changed slightly, all three cases provide similar gouging results.

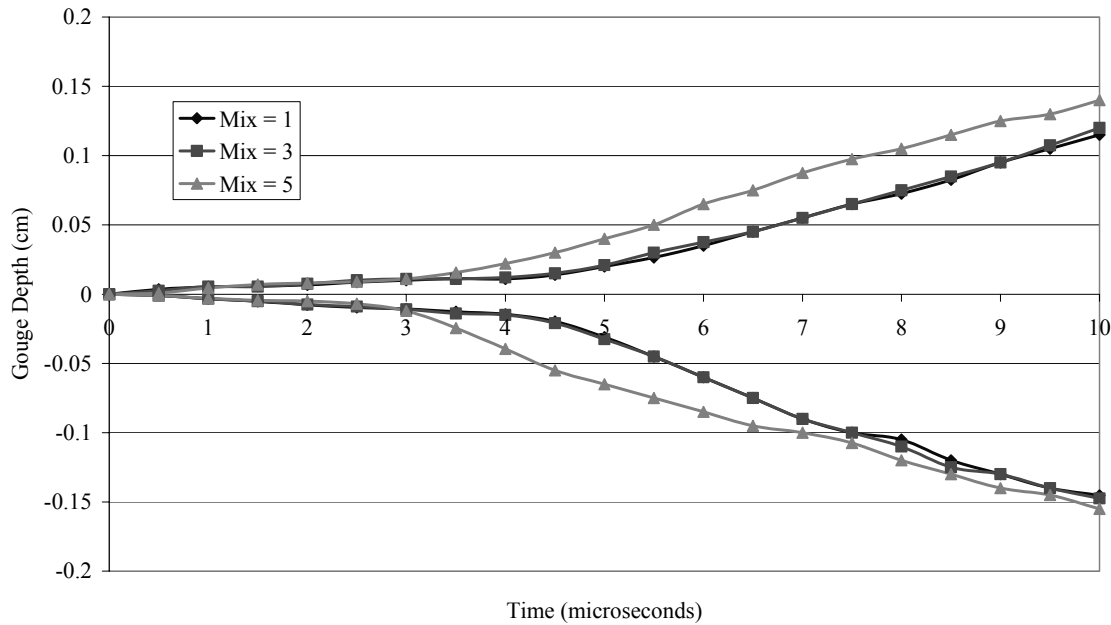


Figure 80. Maximum Gouge Depth Vs. Time for Three Different Mixed Cell Treatments

Material Interface Models

Because material interfaces are characterized by mixed cells, the previously discussed mixed cell treatments are one method of modeling the material interface. In addition, two specially developed interface models in CTH are the Slide Line and Boundary Layer Interface models. These special models allow for the simulation of sliding interfaces by allowing the materials at an interface to retain their strength properties, yet move independently. The slide line routine, for example, allows material along designated interfaces to keep their strength in compression and tension, but sets its shear strength to

zero to allow the materials to slide. Behavior can be computed at material interfaces using a Lagrangian calculation by providing spatial slidelines, which are used when large transverse deflections of the material interface are expected [40]. The Boundary Layer Interface model couples the deformation of materials where they share an interface. One surface is deformed using the forces on both materials, and the adjoining surface is transversely constrained to move with it, although the materials may maintain distinct tangential velocities. The effects of friction may be included, which is a desirable attribute in simulating gouging effects.

Results of these models are shown in Figure 81 and compared to the baseline case. It turns out that the run using the slide line algorithm experienced numerical problems causing the time step to drop below 10^{-12} s, at which point the calculation was ended. CTH often experiences such problems, which are usually resolved by changing the grid or other properties. But until the calculation was terminated, results were similar to the baseline case.

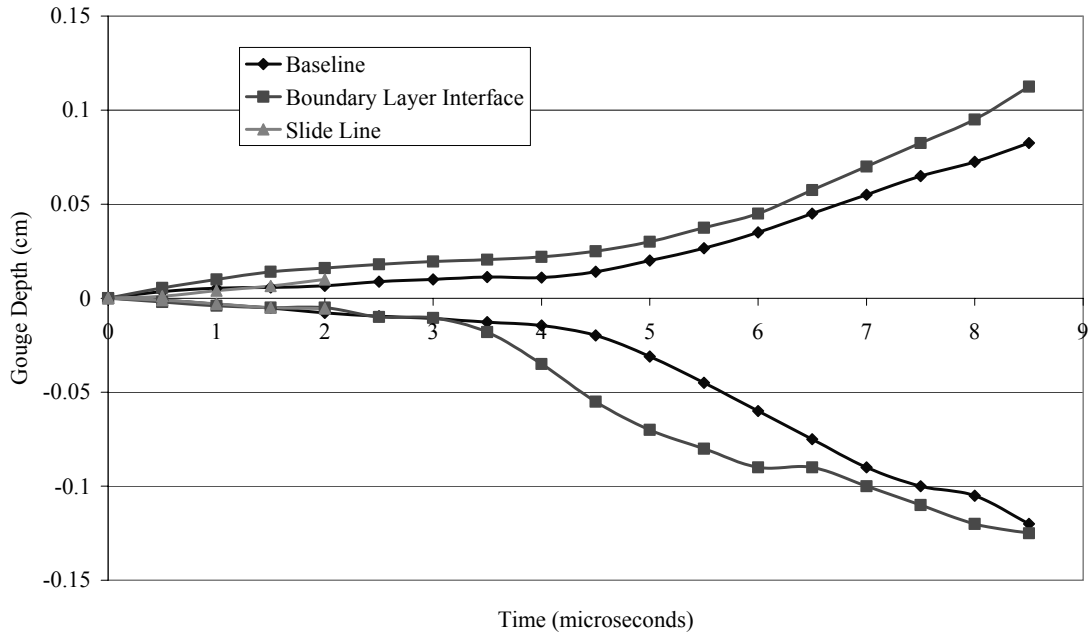


Figure 81. Maximum Gouge Depth Versus Time for Material Interface Models

In the case of the Boundary Layer Interface algorithm, penetration of the rail into the slipper occurs more rapidly than the baseline case for the first $1.5 \mu\text{s}$, and then the rates become equivalent. Jet development occurs at the same time, and the growth rate is also similar after jet formation. As for the slipper penetration into the rail, results are similar in both cases until $3.5 \mu\text{s}$, when the Boundary Layer Interface model begins to form a slipper jet $1 \mu\text{s}$ sooner than the baseline model. After this point, growth rates are about the same. Overall, it appears that the interface model does not make a significant difference in the development of gouging.

Friction

Another useful reason for examining the Boundary Layer Interface algorithm is that it also allows for the implementation of a coefficient of friction. Using this option, the

effect of friction is reviewed by the use of simulations conducted with coefficients of friction from 0.0, 0.1, 0.2, and 0.3. This range was considered because test track engineers find that using a coefficient of friction of 0.2 provides a suitable estimation in velocity vs. position calculations. Gouge initiation and development vs. time for frictional calculations has been plotted in Figure 82. In this case, the effect of friction on gouging appears to be negligible during the development of the gouge itself. It should be recognized, however, that friction is still a considerable source of heat that would affect the slipper temperature, which, as discussed previously, does affect the gouging.

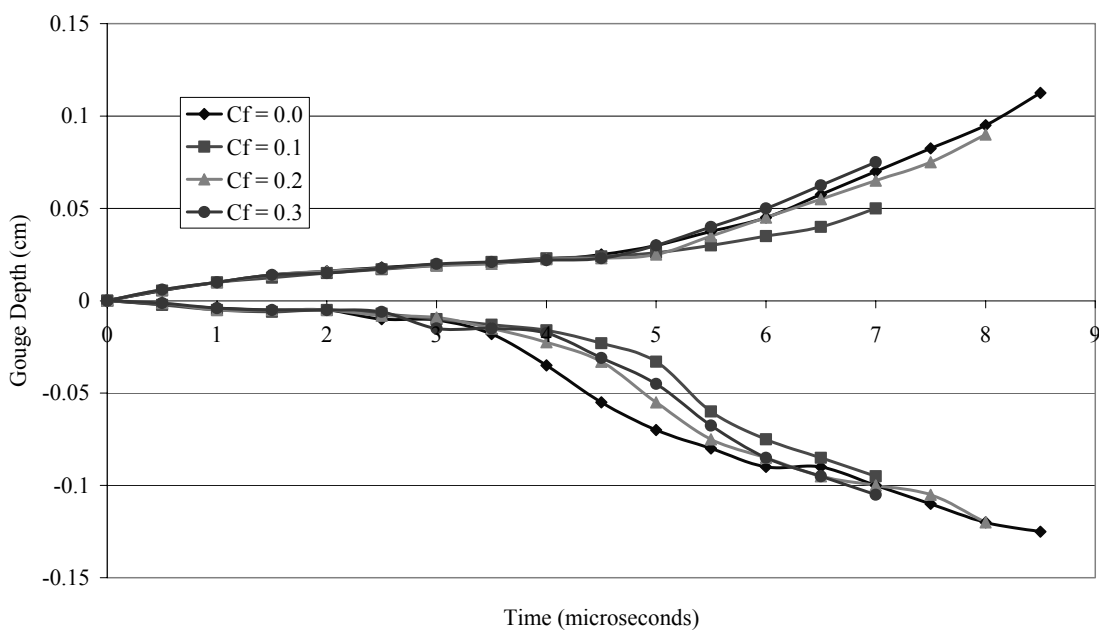


Figure 82. Maximum Gouge Depth Vs. Time for Various Frictional Coefficients

Fluid Behavior and Instability

Investigation of gouging has produced some additional observations. In hypervelocity impact, it has been observed in the past that metals can behave as fluids due to the effects of momentum. In gouge development, this behavior is seen in the formation of the material jets, and the interaction of the materials in the region of the gouge is not unlike fluid mixing, and the unstable nature of the development appears to be very similar to a fluid instability known as a Kelvin-Helmholtz instability where an interlocking wave like vortex pattern develops. Kelvin-Helmholtz flow is the flow of two materials in parallel contact at different velocities. The impact pressure allows the localized plasticity to develop and behave like a fluid interface, creating the Kelvin-Helmholtz instability. Once the instability begins to develop, the interacting regions continue to experience hypervelocity impact, allowing the sustainment of a plastic region and enabling the instability to grow. Figure 83 and Figure 84 compare the gouge instability to a Kelvin-Helmholtz instability in fluid flow. Since there is previous work in the field [83-85], any additional research into the gouging phenomena should be accompanied by a review of the Kelvin-Helmholtz instability.

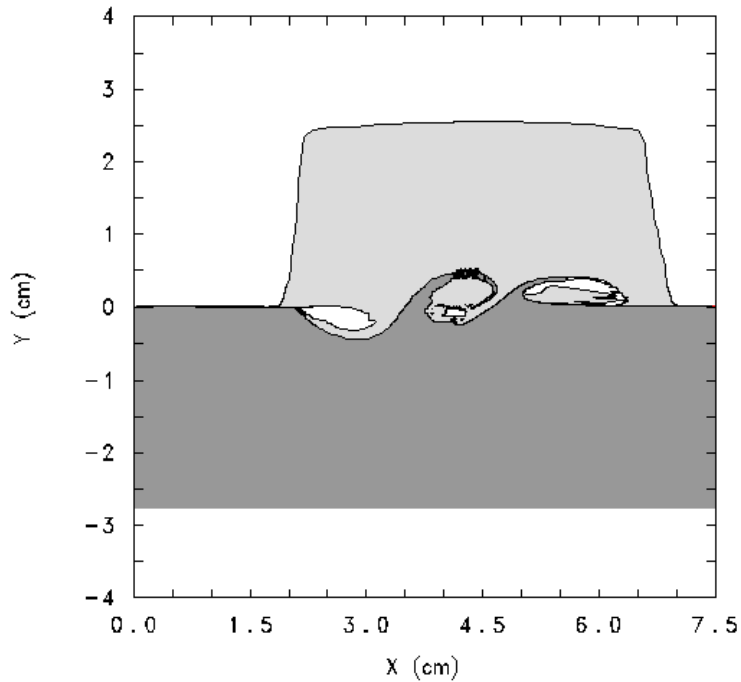


Figure 83. Fluid-Like Mixing of Rail and Slipper

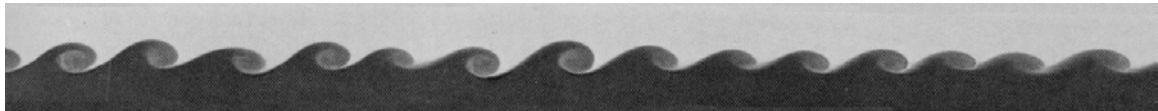


Figure 84. Kelvin-Helmholtz Instability in Fluid Flow [85]

Explosive Welding

Overall, the development of the gouge also appears similar to the explosive welding process, in which metals are exploded toward each other such that an interlocking wave pattern appears at the interface, and then hardens in that position to “weld” the materials together, as in Figure 85. It is likely that the same mechanisms are involved, and a great deal of research has been performed on the conditions under which this process will

occur [86,42]. Further investigation into gouging should include a thorough understanding of the physics of explosive welding.

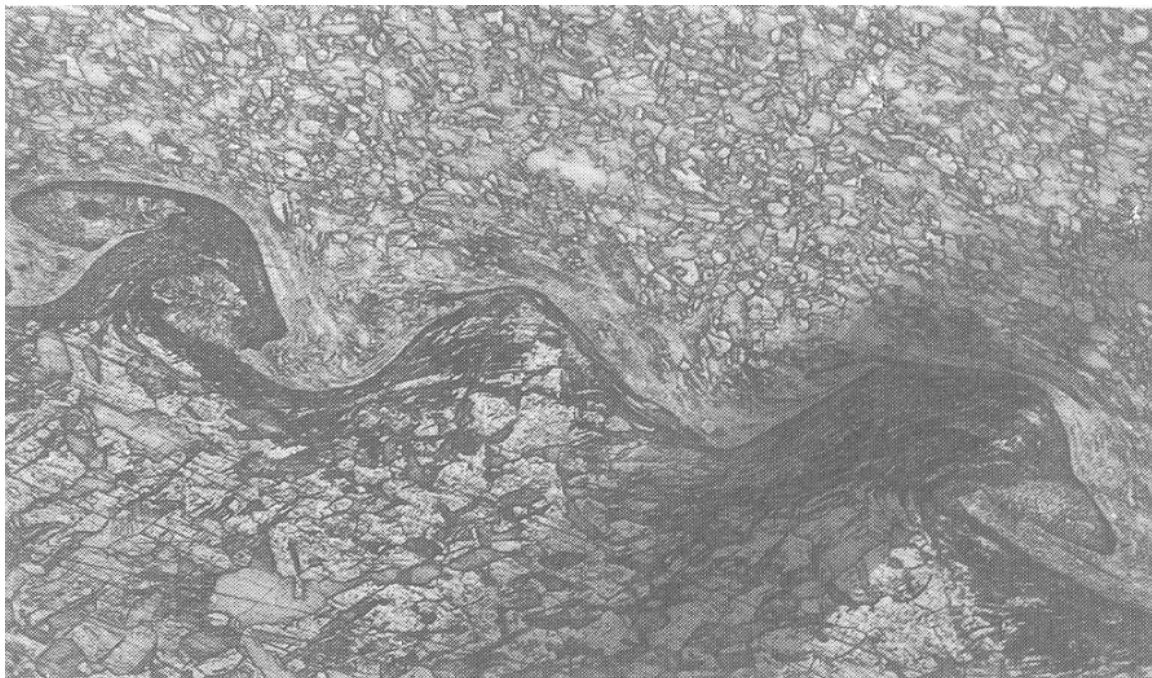


Figure 85. Interface of Two Explosively Welded Metals [42]

V. Summary and Conclusions

Conclusions can now be made about how the hypervelocity impact leads to gouging, the effects of wave propagation, high temperatures, slipper geometry, and yield stress.

Hypervelocity Impact

The initial impact forces of an oblique impact are great enough to cause plasticity at the interface. Due to the plastic deformation of the slipper penetrating into the rail and the rail material pushed in front of it, an interlocking contact region where the slipper is impacting horizontally into the slipper is created. Getting the material to impact in the hypervelocity direction is the key to gouge initiation. This normal component of hypervelocity impact is provided by a present asperity, slipper penetration, or displacement of rail material to create an asperity. This impact creates a high-pressure core centered on the point of greatest impact energy, or where the interface slope is most normal to the velocity. Under sufficient pressure, material jets will form that penetrate into the material surfaces. The pressure in this region is great enough to cause the surrounding material to continue to yield, allowing additional deformation. The additional deformation increases the size of the interlocking region, which increases the size of the high-pressure and high stress region. In turn, this increases the size of the plastic region, allowing the deformation to continue to grow. Because the physical features of a gouge cause the gouge to continue to grow in this manner, gouging can be seen as a material instability.

Plastic deformation, vertical force, or low material strength are contributing factors of gouge initiation, but each of these alone are not sufficient to produce gouging. The key

feature of gouging is the initiation of the material jets. This jet formation and the way in which it behaves characterize gouging as interaction and mixing between two materials. In order for a jet to form between two materials in intimate contact, the jet must penetrate the material opposite. This scenario requires the deformation of both materials involved. Because the jet formation requires plasticity of both materials, if one material has conditions or properties that prevent it from participating in gouging, gouging will not occur, even if the other material has conditions or properties that allow it to gouge.

Shock Wave Propagation

In high velocity impact dynamics, the creation, propagation, reflection, and interaction of shock waves can affect the material response. Stress waves are initiated at the impact interface, and propagate into both the slipper and the rail at the local sound speed, which is near 4.6 km/s. At the time that jet formation and the onset of gouging begin to occur, the stress wave in the rail is still propagating away from the slipper and the stress wave in the slipper is just reaching the top of the slipper. Since these stress waves are not interacting near the location of gouge formation while the gouge is developed, it is unlikely that the wave propagation is influential in gouge initiation.

Effect of High Temperatures

The initial temperature of the system is determined analytically before the numerical calculation is begun. The initial temperature profiles are highly dependent on assumptions made about the heat source. Based on the constitutive equations used, it is expected that the yield stress will be decreased, and this is likely to increase the tendency to gouge.

As the temperature of the slider increases toward 1500 K, the amount of time that passes between impact and gouge onset tends to decrease, and the growth rate of the gouge increases. Further temperature increases toward the material melting temperature delay the onset of the jet formation, but continue to increase the growth rate of the gouge.

At the elevated temperatures the mechanism of gouging begins to change. At room temperature, the gouge develops at a location based on the small rail hump initially at the leading edge of the slider. At high temperatures however, multiple gouges are observed, some of which develop away from the leading edge at a point where slider penetration due to the vertical component of impact is the greatest.

At the temperatures studied between 298 K and 2500 K, both these mechanisms are present. At the start time, these phenomena are collocated near the leading edge. The leading edge instigated interaction always moves at the same speed independent of temperature. At lower temperatures, the penetration interaction moves at the same speed, and the two phenomena occur together. At higher temperatures, however, the penetration interaction tends to move slower. At 2500 K, the penetration-initiated instability is actually behind the location of the initial leading edge point. The higher temperatures hinder the leading edge gouge, while the penetration gouge is promoted by it.

Higher temperatures lower the yield stress of the materials, leading to less resistance to gouging. While the room temperature gouge has reached higher temperatures contributing to weakening of the material, the heated slider provides a jump-start to reaching higher temperatures, leading toward similar behavior and deformation as the unheated case, but at an earlier time.

Clearly, elevated slipper temperatures affect the onset and subsequent development of gouging. Even as low as 500 K, the higher temperature aids in the initiation of gouges and accelerates their growth. Above 1500 K, growth is further accelerated, however initiation is delayed.

Below 2000 K, there is very little difference between the three cases of uniform slipper, time dependent slipper profile, and slipper profile with rail temperature. This indicates that the use of a temperature profile does not effect gouge development below 2000 K, and that only the conditions within 0.1 cm of the surface significantly affect the gouge. But these results also show that the rail temperature, confined to within 0.005 cm of the surface did not have any effect.

At 2500 K, the situation is markedly different. At this temperature, the slipper material is above its melting point of 2310 K, and the yield stress is reduced to zero. In this environment, each of the three temperature environments produced different results. Using the temperature profile in the slipper caused gouging to initiate a microsecond sooner than the uniform slipper. In the case of the slipper profile, only the surface is melted while the interior is still solid. Using the slipper profile in conjunction with the rail temperature results in gouging immediately because of the high pressure in the rail resulting from the equation of state. This pressure causes the rail to rise upward so much and so rapidly that the slipper impacts this part of the rail horizontally.

Successful modeling of gouging should include modeling the temperature environment, as the slipper temperature has proven to have a significant affect on the material yield stress and its resistance to gouging. As the slipper temperature increases above ambient temperature, the tendency is that gouging initiates sooner and grows faster

during an oblique impact, until the temperatures approach the melting temperature, where the onset of gouging begins to get delayed. Detail of the temperature environment has proven to be not as important. Inclusion of a thermal profile or rail temperature did not significantly influence events until the source temperature was above the melting temperature.

Slipper Geometry

When studying slippers of different geometries, it was found that slippers with shallow leading edge angles of less than 1.790° with respect to the rail did not gouge under the same velocity conditions that caused a similarly sized slipper with a rounded leading edge to gouge. While the maximum penetration depth was similar in the different cases, the shallow leading edge resulted in a shallow slope at the material interface, inhibiting the initiation of material jets

Effect of Material Yield Stress

Experience at the test track has shown that using slipper materials with high yield stress tends to increase the resistance to gouging, but changing materials also alters all other properties as well. By making no changes other than to increasing the yield stress of the rail from 0.175 GPa to 0.7 GPa, gouging was prevented. This reinforces the idea that yield stress is a key property that affects resistance to gouging and therefore is an important consideration when conducting or modeling gouging. This also shows that increasing the rail yield stress inhibits gouging. Furthermore, this result shows that changing a property of only one material effects the development of gouges that occur in

both materials simultaneously. It is also interesting to notice that the increased rail yield stress did not inhibit the penetration of the slipper into the rail.

Preventing Gouging

Current gouge reduction methodology involves altering the rail and slipper materials. Since the rail is a large infrastructure, material changes are made through the use of rail coatings. Gouging is an interaction, so one material may be a factor in creating or preventing gouging conditions in the other. Gouging requires plastic flow of both materials and the formation of material jets. The initial slipper penetration into the rail, and the rail hump deformation, lead to sufficient horizontal impact to cause the creation of the material jets in an oblique impact. If the materials are dissimilar, it is not expected that both material exhibit plasticity, flow, and jet formation at the same time. Probably one material would fail before the other. Gouging will not form until both materials fail. Under certain conditions, it is possible that the behavior of the first failed material may aid in preventing the failure of the other material. If the first failed material responds in such a way that penetration does not occur to such an extent, the hump deformation does not occur, prevents the horizontal component of impact, or prevents the build up of pressure at the interaction region, then gouging may not occur.

Current rail coatings may be around 6 mils thick, which is about 0.015 cm. It is interesting to notice that the penetration depth of the slipper in most of these simulations before jet formation occurred was between 0.012 and 0.02 cm. If the coating material is such that it can displace or even jets away without resulting in forces great enough for the slipper to jet, no gouging should occur.

The new hypersonic sled being developed at the HHSTT for the 10,000 fps tests is a dual rail design, which will provide more structural flexibility than the previous monorail designs. This flexibility may prove beneficial in reducing vertical loads and slipper penetration.

Subjects for Future Studies

Much work still needs to be done to solve the problem of gouging at the Holloman High Speed Test Track and in hypervelocity gun barrels. Since hydrocode modeling is a viable method of examining the gouging process, using hydrocode models to perform design work of slipper/rail systems is a logical next step. The development of designs that are resistant to gouging and/or have the ability to arrest gouge propagation once gouging is initiated would be the most desirable. Such designs could exploit special geometries, control of loads, different slipper materials, and rail coatings. In addition, to gain confidence in the quantitative results of hydrocode based designs, further work can be done in determining and resolving any quantitative discrepancies between hydrocode and experimental gouge data.

Ultimately, some damage criteria that predict the onset of gouging would be useful. These criteria could relate all or many of the factors that affect gouging by directly indicating a relationship between material properties, velocity, impact angle, etc. to gouge characteristics.

Appendix: Sample Input Deck

```
*eor* cgenin
*
*  cthgen grid generation input for Gouge simulation
*
*
*          |      ----->  |
*          |      |      |
*          |      v      /
*  -----
*
*
*  vx=2.0 km/s, vy=50 m/s  V300 Steel Slider, 1080 Steel Rail, No Atm.
*  No Slide line. mix=1 frac=1 Rounded corner.
*
*E1

control
  mmp
  ep
  vpsave
endcontrol

mesh          *Define the Eulerian mesh
  block 1  geom=2dr  type=e
    x0=0.0          *Create grid in x direction
    x1 n=40  w=3.5 dxf=0.08
    x2 w=0.5 dxf=0.08 dxl=0.005
    x3 n=200 w=1.0 dxf=0.005
    x4 w=0.5 dxf=0.005 dxl=0.08
    x5 n=25  w=2.0 dxf=0.08
  endx
  y0=-2.76      *Create grid in y direction
  y1 n=28  w=2.24 dyf=0.08
  y2 w=.26 dyf=0.08 dyl=0.005
  y3 n=104 w=0.52 dyf=0.005
  y4 w=.26 dyf=0.005 dyl=0.08
  y5 n=28  w=2.24 dyf=0.08
  endy
  endblock
endmesh

insertion of material  *Input location of the materials
  block 1
    package guider      *Draw the guider
      material 1
      numsub 100
      xvel 0.0
      yvel 0.0
      insert box
        p1 0.0,-2.76
        p2 7.5,0.0
      endinsert
    endpackage
```

```

package slider      *Draw the slider
  material 2
  numsub 100
  temperature = 2.53575e-2 * eV = 70F
  xvel 2.0e+5
  yvel -50.0e+2
  insert box
    p1 0.08, 0.0
    p2 4.45, 2.54
  endinsert
  delete circle
    center 4.25, 0.2
    radius 0.2
  enddelete
  delete box
    p1 4.25, 0.2
    p2 4.45, 0.0
  enddelete
endpackage

package sliderround *Draw the rounded corner of the slider
  material 2
  numsub 100
  temperature = 2.53575e-2 * eV = 70F
  xvel 2.0e+5
  yvel -50.0e+2
  insert circle
    center 4.25, 0.2
    radius 0.2
  endinsert
endpackage
endblock
endinsertion

edit
  block 1
  expanded
endblock
endedit

tracer
  *Target guider      *Define locations of Lagrangian tracers
  add 4.2, -0.02 to 7.4, -0.02 n=15
  add 4.2, -0.04 to 7.4, -0.04 n=15
  add 4.2, -0.06 to 7.4, -0.06 n=15
  *Target slider
  add 0.8, 0.02 to 4.0, .02 n=15
  add 0.8, 0.04 to 4.0, .04 n=15
  add 0.8, 0.06 to 4.0, .06 n=15
endt

eos          *Set material equation of state options
  MAT1 SES IRON
  MAT2 SES STEEL_V300
ende

```

```

epdata
  vpsave
  mix=1
  matep=1 * IRON Guider/initiator *Activate Johnson-Cook model for rail
    johnson-cook IRON
    poisson 0.28
  matep=2
    st=19 * STEEL V300 Slider * Activate SGL model for slipper
    poisson 0.27
ende

*****
*eor* cthin
E1
* cth solver input
control
  mmp          *Use multiple temperatures and pressures in mixed cells
  frac=1
  tstop = 24.0E-6 *Solution stop time
  nscycle=55000   *Solution stop cycle
  rdumpf=991800.
  cpshift=600.
  ntbad=999999
endc

Convct      *Set interface tracker
  convection=1
  interface=high_resolution
endc

edit        *Select time increment to store history and plot data
  shortt
    time = 0.0 ,dt=10.0e-6
  ends
  longt
    time = 0.0e0 , dt = 1.0
  endl
  plott
    time 0.5e-6 dtfrequency 0.5e-6
  endp
  histt
    time 0.5e-6 dtfrequency 0.5e-6
    htracer all
  endhistt
ende

boundary    *Define boundary conditions
  bhydro
    block 1
      bxbot = 1 , bxtop = 1
      bybot = 1 , bytop = 2
    endb
  endh
endb

```

```
vadd          *Add velocity to whole system to maintain gouge location
  block=1
  tadd=0.0
  xvel=-1.08333e+5
endvadd

mindt          *Define minimum time step
  time=0. dt=1.e-12
endn
maxdt          *Define maximum time step
  time=0. dt=.01
endx
```

References

1. Meyers J, 'Slipper Wear/Gouging Phenomena', unpublished request for proposals for gouging research (1999).
2. Krupovage DJ, 'Rail Friction and Slipper Wear on the Holloman High Speed Test Track', 38th Meeting of the Aeroballistic Range Association, 6585th Test Group, Test Track Division, Holloman AFB, NM (1987).
3. Krupovage DJ, Mixon LC, and Bush JD, 'Design Manual for Dual Rail, Narrow Gage, and Monorail Rocket Sleds', Holloman High Speed Test Track (1991).
4. Schmitz CP, Photos of High Speed Test Sled (2000).
5. Hooser M, Personal Correspondence (1999).
6. Preston DL, 'Mach 6 Sled Development From 1963 to September 1964', Sandia Corp., Report W80098 (1964).
7. Gerstle FP, 'The Sandia Rocket Sled Rail and Slipper Study', Sandia National Laboratories (1968).
8. Gerstle FP, 'Deformation of Steel During High Velocity Unlubricated Sliding Contact', Ph.D. Dissertation, Duke University, (1972).
9. Krupovage DJ and Rassmussen HJ, 'Hypersonic Rocket Sled Development', Test Track Division, Holloman Air Force Base, Report No. AD-TR-82-41 (1982).
10. Krupovage DJ, 'Rail Gouging on the Holloman High Speed Test Track', 35th Meeting of the Aeroballistic Range Association, 6585th Test Group, Test Track Division, Holloman AFB, NM (1984).
11. Mixon LC, 'Assessment of Rocket Sled Slipper Wear/Gouging Phenomena', Chapter 4 of *Slipper Wear and Gouging Phenomena* ARA SBIR Report for 846 TS/TGTAD by T Caipen and C Needham (1997).
12. Barber JP and Bauer DP, 'Contact Phenomena at Hypervelocities', *Wear*, Vol. 78, pp. 163-169 (1982).
13. Trott BD, 'Evaluation of Rocket Sled Shoe Materials', Battelle Memorial Institute, Columbus Laboratories Report BMI-X-476 (1967).

14. Graff KF, Dettloff BB, and Bobulski HA, 'Study of High Velocity Rail Damage', Dept. of Engineering Mechanics, Ohio State University Research Foundation, Air Force Special Weapons Center, USAF Contract No. F29600-67-c-0043 (1968).
15. Graff KF, and Dettloff BB, 'The Gouging Phenomenon Between Metal Surfaces at Very High Speeds', *Wear*, Vol. 14, pp. 87-97 (1969).
16. Graff KF and Dettloff BB, 'Study of High Velocity Rail Damage', Dept. of Engineering Mechanics, Ohio State University Research Foundation, Air Force Special Weapons Center (1970).
17. Tarcza, KR, 'The Gouging Phenomenon at Low Relative Sliding Velocities', Thesis, University of Texas at Austin (1995).
18. Boehman LI, Barker JP, and Swift HF, 'Simulation of Friction, Wear, Anti Gouging for Hypersonic Guider-rail System', Arnold Engineering Development Center (PMP), Report No. UDR-TR-77-68, November 1977.
19. Barker LM, Trucano TG, and Munford JW, 'Surface Gouging by Hypersonic Sliding Contact Between Metallic Materials', Sandia National Laboratories Report, SAND87-1328-UC-34 (1987).
20. Tachau RDM, 'An Investigation of Gouge Initiation in High-Velocity Sliding Contact', Sandia National Laboratories Report SAND91-1732-UC-706 (1991).
21. Tachau RDM, Yew CH, and Trucano TG, 'Gouge Initiation in High-Velocity Rocket Sled Testing', Hypervelocity Impact Symposium (1994).
22. Schmitz CP and Schmitz RP, 'Slipper Wear/Gouging Analytical Tool', Phase I SBIR Final Report Contract No. F08365-97-c-0046, AZ Technology Report No. 97-4-351-001 (1998).
23. Barker LM, Trucano T, and Susoeff AR, 'Railgun Rail Gouging by Hypervelocity Sliding Contact', *IEEE Transactions on Magnetics*, Vol. 25, No. 1, pp. 83-87 (1988).
24. Susoeff, AR and Hawke, RS, 'Mechanical Bore Damage in Round Bore Composite Structure Railguns', Lawrence Livermore National Laboratory Report UCID-21520 (1988).
25. Marshall RA, 'The Mechanism of Current Transfer in High Current Sliding Contacts', *Wear*, Vol. 37, pp. 233-240 (1976).

26. Rabinowicz E, 'The Temperature Rise at Sliding Electrical Contacts,' *Wear*, Vol. 78, pp. 29-37 (1982).
27. Persad C and Peterson DR, 'High Energy Modification of Surface Layers of Conductors', *IEEE Transactions on Magnetics*, Vol. MAG-22, no. 6, pp. 1658-1661 (1986).
28. Weldon WF, 'Development of Hypervelocity Electromagnetic Launchers', *International Journal of Impact Engineering*, Vol. 5, pp. 671-679 (1987).
29. Korkegi RH and Briggs RA, 'Aerodynamics of Hypersonic Slipper Bearing', Aerospace Research Laboratory Report ARL 68-0028 (1968).
30. Korkegi RH and Briggs RA, 'The Hypersonic Slipper Bearing- A Test Track Problem', *Journal of Spacecraft and Rockets*, Vol. 6, No. 2, pp.210-212 (1969).
31. Abrahamson GR and Goodier JN, 'The Hump Deformation Preceding a Moving Load on a Layer of Soft Material', *Journal of Applied Mechanics*, Paper No. 61-APMW-5 (1961).
32. Cole J and Huth J, 'Stresses Produced in a Half Plane by Moving Loads', *Journal of Applied Mechanics*, Paper No. 58-APM-8 (1958).
33. Gerstle FP and Pearsall GW, 'The Stress Response of an Elastic Surface to a High-Velocity, Unlubricated Punch', *Journal of Applied Mechanics*, Paper No. 75-APMW-1, pp. 1036-1040, (1974).
34. Chao CC, 'Dynamical Response of an Elastic Half-Space to Tangential Surface Loadings', *Journal of Applied Mechanics*, Paper No. 60-APM-29, pp. 559-567, (1960).
35. Adler AA and Reismann H, 'Moving Loads on an Elastic Plane Strip', *Journal of Applied Mechanics*, pp. 713-718 (1974).
36. Criner HE and McCann GD, 'Rails on Elastic Foundation Under the Influence of High-Speed Traveling Loads', *Journal of Applied Mechanics*, Vol. 75, pp.13-22 (1953).
37. Kenney JT, 'Steady-State Vibrations of Beams on Elastic Foundations for Moving Loads', *Journal of Applied Mechanics*, Paper No. 54-APM-8, pp. 359-364 (1954).
38. Florence AL, 'Traveling Force on a Timoshenko Beam', *Journal of Applied Mechanics*, Paper No. 64-WA/WPM-26, pp. 351-358 (1965).

39. Choros J and Adams GG, 'A Steadily Moving Load on an Elastic Beam Resting on a Tensionless Winkler Foundation', *Journal of Applied Mechanics*, Paper No. 79-APM-11, pp. 175-180 (1979).
40. Anderson CE Jr, 'An Overview of the Theory of Hydrocodes', *International Journal of Impact Engineering*, Vol. 5, pp. 33-59 (1987).
41. Benson DJ, 'Computational Methods in Lagrangian and Eulerian Hydrocodes', *Computer Methods in Applied Mechanics and Engineering* Vol. 99, pp. 235-394 (1992).
42. Meyers MM, *Dynamic Behavior of Materials*, John Wiley and Sons, Inc., New York (1994).
43. Karpp RR, 'Warhead Simulation Techniques: Hydrocodes', *Tactical Missile Warheads* Chapter 5 Vol. 155 Progress in Astronautics and Aeronautics, pp. 223-313 (1993).
44. Chan KS, Bodner SR, and Lindholm US, 'Phenomenological Modeling of Hardening and Thermal Recovery in Metals', *Journal Engineering Materials and Technology* Vol. 110, pp. 1-8 (1988).
45. Johnson GR and Cook WH, 'A Constitutive Model and Data for Metals Subjected to Large Strains, High Strain Rates, and High Temperatures,' in *Seventh International Symposium on Ballistics*, The Hague, Netherlands (1983).
46. Zerilli FJ and Armstrong RW, 'Dislocation-Mechanics-Based Constitutive Relations for Material Dynamics Calculations', *Journal of Applied Physics* Vol. 61, pp. 1816-1825 (1987).
47. Steinberg DJ, Cochran SG, and Guinan MW, 'A Constitutive Model for Metals Applicable at High-Strain Rate,' *Journal of Applied Physics* Vol. 51, pp. 1498-1504 (1980).
48. Steinberg DJ and Lund CM, 'A Constitutive Model for Strain Rates from 10-4 to 106 S-1,' *Journal of Applied Physics* Vol. 65, pp. 1528-1533 (1989).
49. Steinberg DJ, 'Equation of State and Strength Properties of Selected Materials', Lawrence Livermore National Laboratory Report UCRL-MA-106439 Change 1 (1996).
50. Zukas JA, *High Velocity Impact Dynamics*, John Wiley and Sons, Inc., New York (1990).

51. Wagoner R. and Chenot J-L, *Fundamentals of Metal Forming*, John Wiley and Sons, Inc., New York (1997).
52. Wagoner RH and Chenot J-L, *Metal Forming Analysis*, Cambridge University Press, Cambridge (2001).
53. Hertel ES Jr, Bell RL, Elrick MG, Farnsworth AV, Kerley GI, McGlaun JM, Petney SV, Silling SA, Taylor PA, and Yarrington L, 'CTH: A Software Family for Multi-Dimensional Shock Physics Analysis', Proceedings of the 19th International Symposium on Shock Waves, pp 377-382 (1993).
54. Bell RL, Baer RM, Brannon RM, Elrick MG, Hertel ES Jr, Silling SA, and Taylor PA, 'CTH User's Manual and Input Instructions Version 4.00', Sandia National Laboratories (1999).
55. Hertel ES Jr and Kerley GI 'CTH Reference Manual: The Equation of State Package', Sandia National Laboratories Report SAN98-0974 · UC-705 (1998).
56. McGlaun JM, 'Shock Wave Codes at Sandia National Laboratories', Proceedings of the 18th International Symposium on Shockwaves, pp. 459-462 (1991).
57. Morgan MJ and Shapiro HN, *Fundamentals of Engineering Thermodynamics* John Wiley and Sons, Inc., New York (1992).
58. Kerley GI, 'CTH Reference Manual: The Equation of State Package,' Sandia National Laboratories Report SAND91-0344 (1991)
59. Kerley, G. I., 'Multiphase Equation of State for Iron', Sandia National Laboratories Report SAN93-0027 · UC-410 (1993).
60. Computational Physics Research and Development Department, 'ALEGRA: User Input and Physics Descriptions', Sandia National Laboratories (1999).
61. Asay JR and Kerley GI, 'The Response of Materials to Dynamic Loading,' *International Journal of Impact Engineering* Vol. 5 (1986).
62. Holmquist TJ and Johnson GR, 'Determination of Constants and Comparison of Results for Various Constitutive Models', *Journal de Physique IV*, Colloque C3, suppl. au *Journal de Physique III*, Vol. 1, pp. C3:853-C3:860 (1991).
63. Silling SA, 'CTH Reference Manual: Viscoplastic Models', Sandia National Laboratories Report SAND91-0291 (1991).

64. Taylor PA, 'CTH Reference Manual: The Steinberg-Guinan-Lund Viscoplastic Model', Sandia National Laboratories Report SAND92-0716 (1992).
65. Versteeg HK and Malalasekera W, *An Introduction to Computational Fluid Dynamics: The Finite Volume Method*, Longman Scientific and Technical, Essex (1995).
66. Couch R, McCallen R, Otero I, and Sharp R, '3D Metal Forming Applications of ALE Techniques', *Simulation of Materials Processing: Theory, Methods, and Applications* pp. 401-406 (1995).
67. Couch R, Sharp R, Otero I, Tipton R, and McCallen R, 'Application of ALE Techniques to Metal Forming Simulations,' *Advanced Methods in Material Modeling* ASME Winter Annual Meeting (1993).
68. Swegle JW, Attaway SW, Hienstein MW, Mello FJ, and Hicks DL, 'An Analysis of Smoothed Particle Hydrodynamics', Sandia National Laboratory Report SAND93-2513 (1994).
69. Von Neumann J, and Richtmyer RD, 'A Method for the Numerical Calculation of Hydrodynamic Shocks', *Journal of Applied Physics* Vol. 21, No. 3, pp 232-237 (1950).
70. Courant R, Friedrichs KO, and Lewy H, 'Uber die partiellen Differenzengleichungen der mathematischen Physik', *Mathematische Annalen* Vol. 100, pp 32-74 (1928).
71. Hoffman KA and Chiang ST, *Computational Fluid Dynamics For Engineers – Volume II*, Engineering Education System, Wichita (1993).
72. Homan ML, 'Wind Tunnel Investigation of Monorail Sled at Transonic Speeds', AEDC-TR 65-73 (1965).
73. Jenke LM and Lucas EJ, 'Supersonic Wind Tunnel Tests of Dual Rail and Monorail Rocket Sleds', AEDC-TR 65-70 (1965).
74. Rhudy RW and Corce JD, 'Static Stability and Axial Force Tests of the Holloman Monorail Rocket Sled at Mach Numbers 8 and 10', AEDC-TR 75-122 (1975).
75. Mixon LC, 'Sled Design Techniques', 6585th Test Group, Holloman AFB, Report AFSWC-TR 71-3 (1971).

76. Schoenfeld WP, 'Requirements for Upgrading the Holloman High Speed Test Track Computational Fluid Dynamics Analytical Capability', 21st AIAA Advanced Measurement Technology and Ground Testing Conference (2000).
77. Dynamic Design and Analysis System simulations, unpublished data from Holloman AFB (2001).
78. Boyce WE and DiPrima RC, *Elementary Differential Equations and Boundary Value Problems*, John Wiley & Sons, Inc., New York (1992).
79. Baker WP, Palazotto AN, and Laird DJ, 'Thermal Diffusion From A High Speed Source Moving Along a Rail', accepted for publication in ASCE *Journal of Aerospace Engineering*, (2002).
80. Hooser M, 'Simulation of a 10,000 Foot per Second Ground Vehicle', Proceedings of the 21st AIAA Advanced Measurement Technology and Ground Testing Conference, AIAA 2000-2290, Denver CO, 19-22 June (2000).
81. Hall AM and Slunder CJ, *The Metallurgy, Behavior, and Application of the 18-Percent Nickel Maraging Steels*, NASA SP-5051 (1968).
82. Schmitz CP, Palazotto AN, and Hooser M, 'A Numerical Investigation of the Gouging Phenomena Within A Hypersonic Rail/Sled Assembly', presented at the AIAA Structures, Structural Dynamics, and Materials Conference, AIAA 2001-1191, Seattle WA, April 17-20 (2001)
83. Acheson DJ, *Elementary Fluid Dynamics*, Clarendon Press, Oxford (1990).
84. Craik ADD, *Wave Interactions and Fluid Flows*, Cambridge University Press, Cambridge (1985).
85. Thorp SA, 'Experiments on the Instability of Stratified Shear Flows: Miscible Fluids', *Journal of Fluid Mechanics* Vol. 46, pp. 299-319 (1971).
86. Rinehart JS and Pearson J, *Explosive Working of Metals*, Pergamon Press, New York (1963).

Vita

Captain David J. Laird graduated from Downers Grove South High School in Downers Grove, Illinois in June 1991. He entered undergraduate studies at the University of Illinois in Champaign-Urbana, Illinois where he graduated with a Bachelor of Science degree in Aeronautical and Astronautical Engineering in May 1995. He then continued studies at Iowa State University as both a teaching assistant and a research assistant, receiving a Master of Science Degree in Aerospace Engineering in August 1997.

He was commissioned through AFROTC in December 1996, and his first assignment was at Los Angeles AFB, where he served as the payload design engineer for the MILSATCOM Advanced Systems Directorate. In January of 1999, he entered the Graduate School of Engineering at the Air Force Institute of Technology. Upon graduation, he will be assigned to the Air Vehicles Directorate of AFRL.

REPORT DOCUMENTATION PAGE

Form Approved
OMB No. 0704-0188

The public reporting burden for this collection of information is estimated to average 1 hour per response, including the time for reviewing instructions, searching existing data sources, gathering and maintaining the data needed, and completing and reviewing the collection of information. Send comments regarding this burden estimate or any other aspect of this collection of information, including suggestions for reducing the burden, to Department of Defense, Washington Headquarters Services, Directorate for Information Operations and Reports (0704-0188), 1215 Jefferson Davis Highway, Suite 1204, Arlington, VA 22202-4302. Respondents should be aware that notwithstanding any other provision of law, no person shall be subject to any penalty for failing to comply with a collection of information if it does not display a currently valid OMB control number.

PLEASE DO NOT RETURN YOUR FORM TO THE ABOVE ADDRESS.

1. REPORT DATE (DD-MM-YYYY) 03-2002	2. REPORT TYPE Doctoral Dissertation	3. DATES COVERED (From - To) Jul 2000-Dec 2002		
4. TITLE AND SUBTITLE THE INVESTIGATION OF HYPERVELOCITY GOUGING		5a. CONTRACT NUMBER		
		5b. GRANT NUMBER		
		5c. PROGRAM ELEMENT NUMBER		
6. AUTHOR(S) Laird, David, J., Captain, USAF		5d. PROJECT NUMBER ENR# 1999-115		
		5e. TASK NUMBER		
		5f. WORK UNIT NUMBER		
7. PERFORMING ORGANIZATION NAME(S) AND ADDRESS(ES) Air Force Institute of Technology Graduated School of Engineering and Management (AFIT/EN) 2950 P. Street, Building 640 WPAFB, OH 45433-7765		8. PERFORMING ORGANIZATION REPORT NUMBER AFIT/DS/ENY/02-01		
9. SPONSORING/MONITORING AGENCY NAME(S) AND ADDRESS(ES) AFOSR/NM Attn: Dr. Len Sakell 801 N. Randolph Street, Room 732 Arlington, VA 22203-1977		10. SPONSOR/MONITOR'S ACRONYM(S)		
		DSN:426-6566	11. SPONSOR/MONITOR'S REPORT NUMBER(S)	
12. DISTRIBUTION/AVAILABILITY STATEMENT APPROVED FOR PUBLIC RELEASE; DISTRIBUTION UNLIMITED.				
13. SUPPLEMENTARY NOTES				
14. ABSTRACT <p>The slipper/rail interface of a hypervelocity rocket sled is subject to immense forces due to dynamic loads and impact of the slipper with the rail, and tremendous heating due to aerodynamic and frictional effects is produced at the interface. Under these severe loading conditions, the material in the rail will sometimes experience large non-linear deformations known as gouging. Hydrocodes are computational solvers designed to handle such non-linear, large deformation, high shock, hydrodynamic applications. The ability of the hydrocode CTH to handle gouge modeling is considered, as well as the manner in which temperature environments affect deformation and plastic strain. The solution techniques and material modeling are described. Using this numerical analysis tool, a study of how gouging occurs and tracing of its development at various impact velocities was undertaken, with emphasis on the effect of shock wave distribution. Modeling the intense aerodynamic and frictional heating near the contact region, the effects of temperature on gouge initiation were evaluated through the application of several thermal environment scenarios that have been developed. The effects of friction, slipper geometry, slipper velocity, and impact method have been considered. Finally, the differences between three-dimensional and two-dimensional analysis considering gouging have been evaluated.</p>				
15. SUBJECT TERMS Rocket Sleds, Hypervelocity Impact, CTH, Gouging				
16. SECURITY CLASSIFICATION OF: a. REPORT U		17. LIMITATION OF ABSTRACT UU	18. NUMBER OF PAGES 197	19a. NAME OF RESPONSIBLE PERSON Dr. Anthony N. Palazotto
				19b. TELEPHONE NUMBER (Include area code) (937) 255-3636 ext 4599